Doctoral Dissertation

Study on the Acoustic Energy Harvester Based on Piezoelectric Polymer for a Fundamental Frequency of Human Voice

(音声基本周波数に対する圧電性高分子を用いた
音響発電素子に関する研究)

Jonghyeon Jeong

鄭　鍾炫

January 2013

Division of Electrical, Electronic and Information Engineering,
Graduate School of Engineering,
Osaka University

Doctoral Dissertation

Study on the Acoustic Energy Harvester Based on Piezoelectric Polymer for a Fundamental Frequency of Human Voice

（音声基本周波数に対する圧電性高分子を用いた
音響発電素子に関する研究）

Jonghyeon Jeong

鄭　　鍾　炫

January 2013

Division of Electrical, Electronic and Information Engineering,
Graduate School of Engineering,
Osaka University

Contents

Abstract

This dissertation is the study on the development of an acoustic energy harvester based on a piezoelectric polymer for a fundamental frequency of human voice. It is organized the following five chapters, three appendices, and acknowledgements. The summaries of each chapter are as follows;

Chapter 1 Introduction

In this chapter, the energy harvesting technology is introduced as the technical background, and piezoelectric effect of poly vinylidene fluoride is described with the constitutive relationships and its applications. The outline of this study is also described.

Chapter 2 Formation of Poly(vinylidene fluoride-tetrafluoroethylene) Thin Films with Sol-Gel Method

In this chapter, I investigated the characteristics of the P(VDF-TeFE) thin film formed with a spin-coating process on a silicon substrate using various solvents. For the conditions to form a thin film on the surface, I carried out the measurement of the film thickness and investigated the surface morphology of the film. The casting solvents, which are mixed two different organic solvents, were employed to effectively form the thin film of P(VDF-TeFE). The roughness of film surfaces was also controlled by the post annealing temperature. With the XPS and FTIR measurements, I observed the limitation of the sol-gel process for P(VDF-TeFE) film forming process.

Chapter 3 Improvement on Properties of Poly(vinylidene fluoride-tetrafluoro ethylene) Thin Films

In this chapter, the improved annealing process was proposed to solve the problems raised in Chapter 2. Piezoelectric properties of P(VDF-TeFE) thin films were preserved from the post annealing temperature higher than its melting point. Furthermore, to assist the rearrangement of

monomers in the P(VDF-TeFE) film, an electric field was applied during the annealing process. With various measurements, I investigated the restoration of the polarization properties of the film and additional advantages of the improved annealing process.

Chapter 4 Design, Fabrication, and Characterization of the Acoustic Energy Harvester for the Fundamental Frequency of Human Voice

In this chapter, I designed the acoustic energy harvester which electric power can be generated from the acoustic wave by a piezoelectric diaphragm and fabricated with micromachining techniques. The diaphragm structure was changed to compensate defects of P(VDF-TeFE) thin films and a proof mass was installed on the diaphragm to lower the resonant frequency of the diaphragm. With the remodeled equivalent circuit and vibration modes, the fabricated devices are measured and characterized for a sound source.

Chapter 5 Conclusions

The achievements obtained in this study are summarized and the consequences are discussed.

Chapter 1
Introduction

1.1 Background

With the advances of portable electronic devices and wireless interface, new energy technology is on the rise for the extension of an actuation time and the miniaturization of the device. The conventional energy-storage technology which is based on chemicals involves some issues; the effective actuation time is limited by a raw material of a battery, and the battery size gets larger by an increase of storage capacity. Nowadays, all of the portable electronic devices are powered only by batteries. As the scale of electronic devices decreases so does the energy consumption. In this context, batteries should be also produced in smaller size by providing more energy storage availability. However, due to technological issues, the batteries have not been following by the same evolution trend, limiting the effective actuation time and performances of the portable electronic devices as they need to be replaced or recharged periodically, and adding also unexpected weight and volume [1]. Ambient power sources, as a replacement for batteries, come into consideration to minimize the maintenance and the cost of operation. Power scavenging may enable wireless and portable electronic devices to be completely self-sustaining, so that battery maintenance can be eventually removed. Hence, self-powered source and energy harvesting technology stand out as the solution of those demerits [2-5].

The energy harvesting technology, also known as energy scavenging or power harvesting, is the process by which energy is derived from environmental energy sources captured and stored into usable electrical energy. Commonly, the term "energy harvesting" is applied when speaking about wireless autonomous devices, like those used in portable electronic devices or wireless sensor networks. A variety of sources are available for energy scavenging, including solar power, ocean waves, piezoelectricity, thermoelectricity, and physical motions such as active or passive human power.

In 1988, *Seiko Epson* in Japan developed a wristwatch powered by human movement. It dispensed the conventional batteries, being the human arm movement used instead. In the wristwatch, the motion of human arm drives a rotating weight, and through a gear train, an electromagnetic generator rotates to generate a power. Since then, several wristwatches has a

generator were developed, but the potential of this system to power larger devices is limited by the slowness how human movement consequently reduced arm movement.

The energy harvesters cannot currently produce sufficient energy to perform mechanical work, but instead provide very small amount of power applicable for low-power consumed devices. Hence, the energy harvesting can be an alternate energy source for small portable electronic devices. In wide perspective, the energy harvesting technology is based on several ambient sources as follows [6],

- Human body: Mechanical and thermal energy,
- Natural energy: Wind, water flow, ocean waves, and solar energy,
- Mechanical energy: Vibrations, mechanical stress, and strain,
- Thermal energy: Waste heat energy variations,
- Light energy: Indoor room light and outdoor sunlight energy, and
- Electromagnetic energy: Inductors, coils, and transformers.

Additionally, chemical and biological sources and radiation can be considered ambient energy sources. From the ambient energy sources, general energy harvesting systems can be classified as follows,

- Electromagnetic energy harvesting,
- Piezoelectric energy harvesting,
- Electrostatic energy harvesting,
- Thermoelectric energy harvesting, and
- Solar energy harvesting.

In this dissertation, by applying a piezoelectric energy harvesting method, I have studied an acoustic energy harvester which is based on human voice as an ambient energy source.

1.2 Resonance for Human Voice

An acoustic energy harvesting was demonstrated using a mesoscale Helmholtz resonator machined from aluminum, delivering a power of 25 mW to a resistive load at 152 dB sound pressure level (SPL) [7]. This acoustic energy may be used to locally power a wireless active liner for suppression of engine noise in turbofan engine nacelles, where noise levels typically reach upwards of 150 dB [8]. There is a substantial amount of data on the fundamental frequency of

human voices (F_0) in the speech of speakers of different ages and genders. Such data have been published in several languages and for various fields. The data reported nearly always include an average measure of F_0, usually expressed in Hz, but in some cases the average duration of a period has been reported instead. Typical values obtained for F_0 are 120 Hz for men and 210 Hz for women [9]. Since the acoustic pressure of a human voice is under 90 dB SPL (0.632 Pa at a reference pressure of 20 μPa) from a distance of 5 cm, the human voice has very low energy as an ambient source.

Since acoustic pressure of a human voice is very low, it is difficult to be delivered on a diaphragm for application in a Helmholtz resonator. Fig. 1.1 shows a lumped element model using only a diaphragm without a bottleneck in a Helmholtz resonator. With the exposure of the diaphragm, the area that can be reached by acoustic waves is increased, and the sensitivity for frequency is improved.

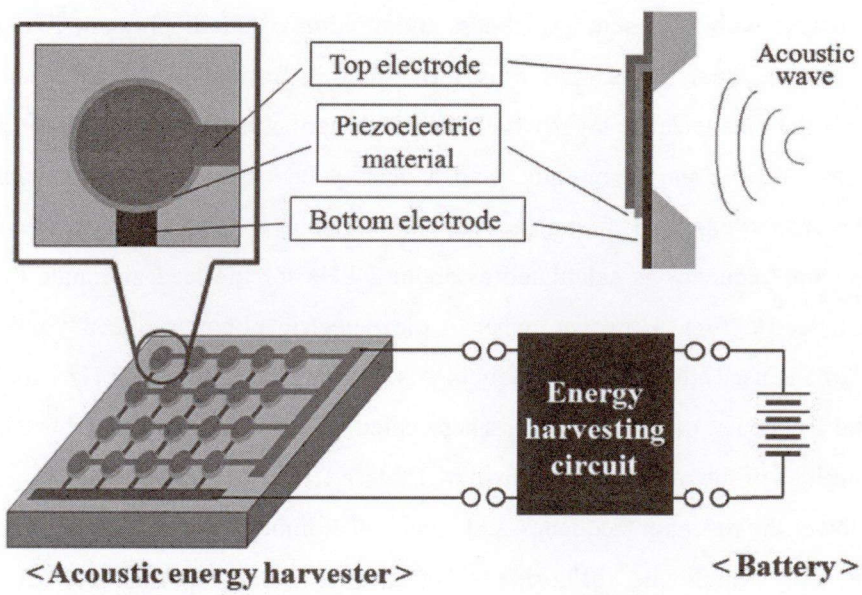

Fig. 1.1 A schematic diagram of an acoustic energy harvesting system

In order to estimate a resonant frequency, f_r, of the diaphragm, the author employed the resonant frequency formula from the study on the capacitive micromachined ultrasonic transducers [10]. The first natural resonant frequency can be written in terms of the effective mass, m_e, and the stiffness, κ, of the diaphragm as;

$$f_r = \frac{1}{2\pi}\sqrt{\frac{\kappa}{m_e}} \simeq \frac{2\,t_d}{\pi a^2}\sqrt{\frac{Y_0 + T}{1.8\,\rho\left(1-\sigma^2\right)}}\,, \tag{1.1}$$

Table 1.1 Comparison of PVDF copolymer with PZT for physical quantities

Parameter		Unit	PZT	PVDF	P(VDF-TeFE)
Density	ρ	kg/m^3	7,500	1,800	1,900
Young's modulus	Y_0	GN/m^2	110	3.0	1.2
Piezoelectric constant	d_{31}	pC/N	123	15 ~ 20	12 ~ 20
	d_{33}	pC/N	-	20 ~ 25	15 ~ 20
	g_{31}	Vm/N	0.011	0.20 ~ 0.25	0.15 ~ 0.22
	g_{33}	Vm/N	-	0.21 ~ 0.26	0.15 ~ 0.26
Dielectric constant	$\varepsilon/\varepsilon_0$		635 ~ 1,300	12	11
Operating temperature limit		°C	300 ~ 328	80 ~ 100	120

where t_d and a respectively represent a thickness and a radius of the diaphragm, Y_0 is the Young's modulus, T is the residual stress, and σ is the Poisson's ration of the diaphragm material. Considering only the piezoelectric layer which the diaphragm consists of mostly, the piezoelectric material that has a low Young's modulus and a density has the obvious advantage for a low resonant frequency. For example, fixing the diaphragm size as 500 nm in thickness and 1 mm in radius, the resonant frequency is calculated as about 3 kHz for the lead zirconate titanate (PZT) used as a piezoelectric film. However, when a piezoelectric polymer like the poly vinylidene difluoride (PVDF) is used, the resonant frequency is calculated is about 200 Hz which is close to the fundamental frequency of human voice. These calculation results are caused by the difference in physical quantities of the materials as shown in Table 1.1.

In order to lower the resonant frequency and mechanical impedance, as referred in Chapter 4, of the diaphragm, poly vinylidene difluoride – tetrafluoroethylene (P(VDF-TeFE)) as a PVDF copolymer is used in this dissertation. Even though a density of a P(VDF-TeFE) is almost same as that of a PVDF, the Young's modulus, as a cause of the increase in mechanical impedance, of a P(VDF-TeFE) is smaller than half of that of a PVDF. Hence, the diaphragm which is sensitive to acoustic wave can be fabricated by reducing mechanical impedance of the diaphragm.

1.3 Piezoelectric Polymer

In biological tissue and other organic materials, very weak piezoelectric effects have been reported since the 1950's [11], but until 1969 it was not that available levels of piezoelectric

properties were discovered in non-biological polymers. While conducting an investigation on the electrets properties of various synthetic polymers in that year, Kawai [12] discovered that drawn and electrically poled PVDF showed exceptional piezoelectricity. A number of subsequent researches have been studied on the piezoelectric [13, 14], ferroelectric [15], dielectric [16], pyroelectric [17], electrocaloric [18], photovoltaic [19], photoelastic [20], and optical properties of PVDF [21].

1.3.1 Poly vinylidene fluoride (PVDF)

PVDF has a chemical composition of $(CH_2–CF_2)_n$ and is more formally known as 1, 1 difluoro-ethylene. It is a semi-crystalline polymer with a crystal volume fraction of about 50% after melt extrusion. The crystal structure after melt processing has a classically spherulitic, non-polar α phase with a helical (**TGTG'**, where **G** refers *gauche* and **T** refers *trans*, and a prime in **G'** refers

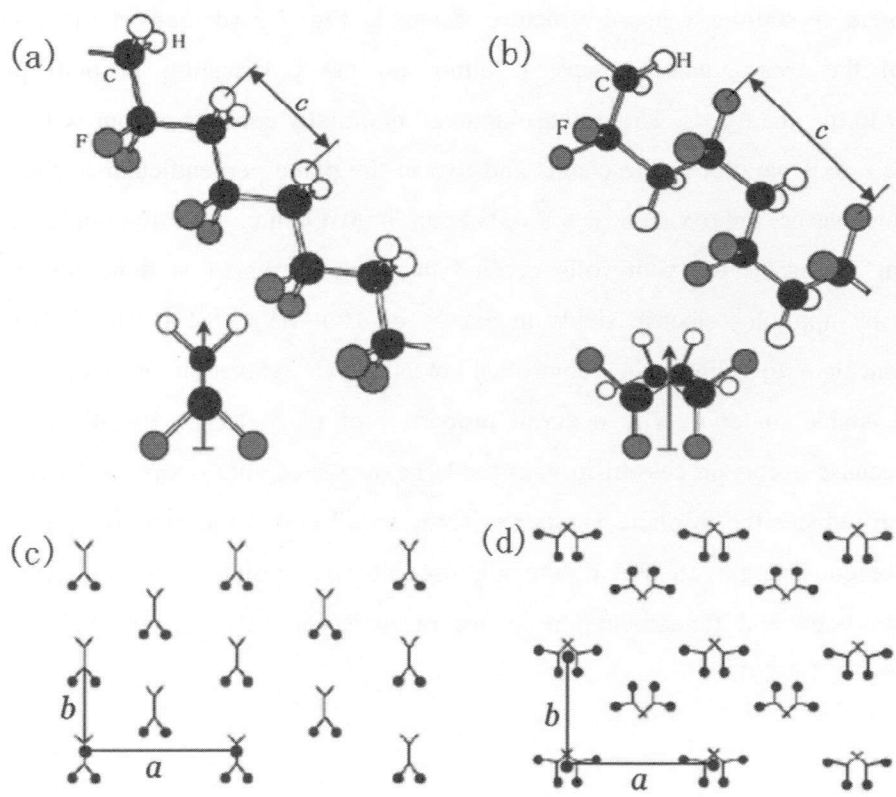

Fig. 1.2 Diagrams of crystalline forms of PVDF (a) in the all-*trans* conformation (inset, end view of a chain); (b) in the alternating *trans-gauche* conformation (inset, end view of a chain); (c) end-on view of the crystal structure of the ferroelectric β phase, composed of close-packed all-*trans* chains; (d) end-on view of the crystal structure of the paraelectric α phase, composed of close-packed *trans-gauche* chains (from [22, 26])

the dihedral angle being opposite to the **G** conformation with respect to the reference plane **T**) configuration as shown in Fig. 1.2 (b). After the melt extrusion, strong mechanical orientation of the polymer is required to introduce the solid state phase transition from the α phase to a highly polar β phase with a planar zig zag, all-*trans* (**TTTT**) chain configuration as shown in Fig. 1.2 (a).

In the β phase, the chain configuration crystallizes in an orthorhombic *mm*2 structure with chains along the crystal *c*-axis and the dipoles aligned approximately along the crystal *b*-axis as shown in Fig. 1.2 (c) [22-26]. The β phase is polar and uniaxial ferroelectric, as the polarization can be repeatedly switched between opposite but energetically equivalent directions along the 2-fold *b*-axis. The β phase unit cell nominally consists of two (CH_2–CF_2) formula units, one along the *c*-axis parallel to the chains as shown in Fig. 1.2 (a). The unit cell dimension is approximately: c = 0.256 nm along the chain axis, b = 0.491 nm along the polarization direction which is the 2-fold axis and a = 0.858 nm perpendicular to the chain axis and to the polarization [25]. It is possible that the unit cell is twice as big, containing two monomers along the chain, because a $\pm 7^0$ dihedral tilt-ordering would make the *c*-axis period two monomers long or $c \approx 0.512$ nm [24].

The complete crystalline α phase structure shown in Fig. 1.2 (d) consist of opposing polar sublattices of the *trans-gauche* chains, resulting no net polarization in both parallel and perpendicular to the chain axis. The α phase unit cell nominally consists of four (CH_2–CF_2) units, two along the *c*-axis parallel to the chains and two in the plane perpendicular to the *c*-axis. The unit cell dimensions are approximately: a = 0.964 nm, b = 0.496 nm, c = 0.462 nm [27].

Subsequent poling of the film rolls applied the melt extrusion is done under controlled temperatures by applying electric fields in excess of 100 MV/m [28]. The PVDF films are thermally annealed to allow the controlled mechanical relaxation necessary to provide commercially stable material. The material properties of piezoelectric PVDF are made more anisotropic because of this process history, as the large degree of microscopic order resulting from the orientation reduces the in plane 1-axis randomness and makes the macroscopic piezoelectric behavior more consistent with that of the microscopic *mm*2 point group symmetry [29]. The detailed morphology and fundamental basis for piezoelectric behavior of PVDF is discussed extensively in [12, 15, 29].

1.3.2 Piezoelectric Constitutive Relationships

The constitutive equations describing the piezoelectric property are based on the assumption that the total strain in the transducer is the sum of mechanical strain induced by both the mechanical stress and the controllable actuation strain caused by the applied electric voltage. There

axes may be identified by numerals rather than letters. In Fig. 1.3, **1** refers to the x axis, **2** corresponds to the y axis, and **3** corresponds to the z axis. The shear planes are indicated by the subscripts **4**, **5**, **6** and are perpendicular to the directions **1**, **2**, and **3** respectively [30]. Axis **3** is assigned to the direction of the initial polarization of the piezo-material, and axes **1** and **2** lie in the plane perpendicular to axis **3**.

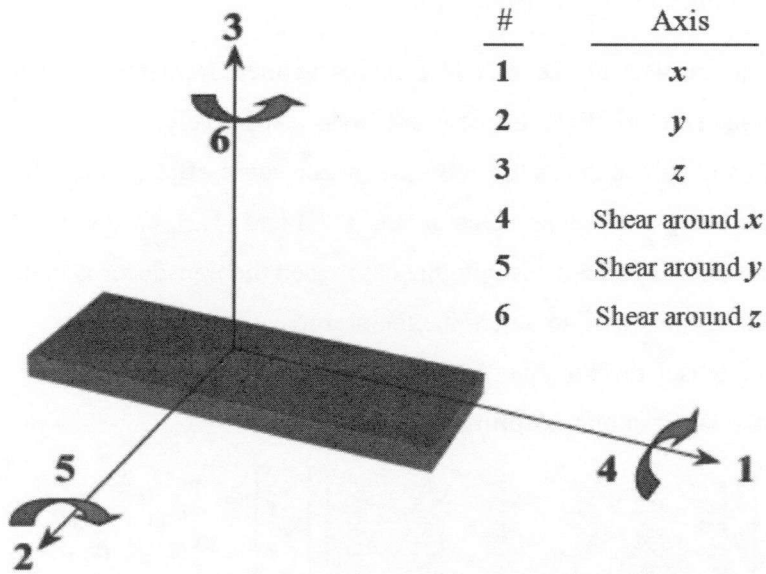

Fig. 1.3 Tensor directions for defining the constitutive relations

The describing electromechanical equations for a linear piezoelectric material can be written as;

$$S_i = \sum_j s_{ij}^E \xi_j + \sum_m d_{im} E_m \ , \tag{1.2}$$

$$D_m = \sum_i d_{mi} \xi_i + \sum_k \varepsilon_{mk}^{\xi} E_k \ , \tag{1.3}$$

where the indexes $i, j = 1, 2, \ldots, 6$ and $m, k = 1, 2, 3$ refer to different directions within the material coordinate system as shown in Fig. 1.3. The above equations can be written in the following form, which is often used for applications that involve sensing;

$$S_i = \sum_j s_{ij}^D \xi_j + \sum_m g_{im} D_m \ , \tag{1.4}$$

$$E_i = \sum_i g_{mi} \xi_i + \sum_k \beta_{mk}^{\xi} D_k \ , \tag{1.5}$$

where

$\boldsymbol{S}$: strain vector (N/m^2),
s : matrix of compliance coefficients (m^2/N),
$\boldsymbol{\xi}$: stress vector (N/m^2),
d : matrix of piezoelectric strain constants (m/V),
$\boldsymbol{D}$: vector of electric displacement (C/m^2),
ε : permittivity (F/m),
$\boldsymbol{E}$: vector of applied electric field (V/m),
g : matrix of piezoelectric constants (m^2/C),
β : impermitivity component (m/F).

Furthermore, the superscripts $\boldsymbol{D}$, $\boldsymbol{E}$, and $\boldsymbol{\xi}$ represent measurements taken at constant electric displacement, constant electric field and constant stress respectively.

Equations (1.2) and (1.4) express the converse piezoelectric effect, which describe the situation when the device is being used as an actuator. Eq. (1.3) and (1.5), on the other hand, express the direct piezoelectric effect, which deals with the case when the transducer is being used as a sensor. The converse effect is often used to determine the piezoelectric coefficients.

By reducing the tensor elements and using standard notations, the resulting equations of (1.2) and (1.3) can be displayed in matrix form as follows [30];

$$\begin{bmatrix} S_1 \\ S_2 \\ S_3 \\ S_4 \\ S_5 \\ S_6 \end{bmatrix} = \begin{bmatrix} s_{11}^E & s_{12}^E & s_{13}^E & s_{14}^E & s_{15}^E & s_{16}^E \\ s_{21}^E & s_{22}^E & s_{23}^E & s_{24}^E & s_{25}^E & s_{26}^E \\ s_{31}^E & s_{32}^E & s_{33}^E & s_{34}^E & s_{35}^E & s_{36}^E \\ s_{41}^E & s_{42}^E & s_{43}^E & s_{44}^E & s_{45}^E & s_{46}^E \\ s_{51}^E & s_{52}^E & s_{53}^E & s_{54}^E & s_{55}^E & s_{56}^E \\ s_{61}^E & s_{62}^E & s_{63}^E & s_{64}^E & s_{65}^E & s_{66}^E \end{bmatrix} \begin{bmatrix} \xi_1 \\ \xi_2 \\ \xi_3 \\ \xi_4 \\ \xi_5 \\ \xi_6 \end{bmatrix} + \begin{bmatrix} d_{11} & d_{12} & d_{13} \\ d_{21} & d_{22} & d_{23} \\ d_{31} & d_{32} & d_{33} \\ d_{41} & d_{42} & d_{43} \\ d_{51} & d_{52} & d_{53} \\ d_{61} & d_{62} & d_{63} \end{bmatrix} \begin{bmatrix} E_1 \\ E_2 \\ E_3 \end{bmatrix}, \quad (1.6)$$

$$\begin{bmatrix} D_1 \\ D_2 \\ D_3 \end{bmatrix} = \begin{bmatrix} d_{11} & d_{12} & d_{13} & d_{14} & d_{15} & d_{16} \\ d_{21} & d_{22} & d_{23} & d_{24} & d_{25} & d_{26} \\ d_{31} & d_{32} & d_{33} & d_{34} & d_{35} & d_{36} \end{bmatrix} \begin{bmatrix} \xi_1 \\ \xi_2 \\ \xi_3 \\ \xi_4 \\ \xi_5 \\ \xi_6 \end{bmatrix} + \begin{bmatrix} \varepsilon_{11}^{\xi} & \varepsilon_{12}^{\xi} & \varepsilon_{13}^{\xi} \\ \varepsilon_{21}^{\xi} & \varepsilon_{22}^{\xi} & \varepsilon_{23}^{\xi} \\ \varepsilon_{31}^{\xi} & \varepsilon_{32}^{\xi} & \varepsilon_{33}^{\xi} \end{bmatrix} \begin{bmatrix} E_1 \\ E_2 \\ E_3 \end{bmatrix}. \quad (1.7)$$

The particular crystal symmetry of a piezoelectric material determines which components of the permittivity, piezoelectric, and stiffness tensors are non-zero and unique. Piezoelectric coefficients are defined by the relationships between the elastic ($\boldsymbol{\xi}$, $\boldsymbol{S}$) and dielectric ($\boldsymbol{E}$, $\boldsymbol{D}$) properties of piezoelectric materials. Assuming that the piezoelectric film is poled along the axis **3**, and viewing the piezoelectric material as a transversely isotropic material, which is true for piezoelectric ceramics, many of the parameters in the above matrices will be either zero, or can be expressed in

terms of other parameters [30]. In particular, the non-zero compliance coefficients are

$$s_{11}^E = s_{22}^E ,$$
$$s_{13}^E = s_{31}^E = s_{23}^E = s_{32}^E ,$$
$$s_{12}^E = s_{21}^E ,$$
$$s_{44}^E = s_{55}^E ,$$
$$s_{66}^E = 2(s_{11}^E - s_{12}^E) .$$

The non-zero piezoelectric strain constants are

$$d_{31} = d_{32} \quad \text{and}$$
$$d_{15} = d_{24} .$$

Finally, the non-zero dielectric coefficients are $\varepsilon_{11}^{\xi} = \varepsilon_{22}^{\xi}$ and ε_{33}^{ξ}. Subsequently, Eq. (1.6) and (1.7) are simplified to;

$$\begin{bmatrix} S_1 \\ S_2 \\ S_3 \\ S_4 \\ S_5 \\ S_6 \end{bmatrix} = \begin{bmatrix} s_{11}^E & s_{12}^E & s_{13}^E & 0 & 0 & 0 \\ s_{12}^E & s_{11}^E & s_{13}^E & 0 & 0 & 0 \\ s_{13}^E & s_{13}^E & s_{33}^E & 0 & 0 & 0 \\ 0 & 0 & 0 & s_{44}^E & 0 & 0 \\ 0 & 0 & 0 & 0 & s_{44}^E & 0 \\ 0 & 0 & 0 & 0 & 0 & 2(s_{11}^E - s_{12}^E) \end{bmatrix} \begin{bmatrix} \xi_1 \\ \xi_2 \\ \xi_3 \\ \xi_4 \\ \xi_5 \\ \xi_6 \end{bmatrix} + \begin{bmatrix} 0 & 0 & d_{31} \\ 0 & 0 & d_{31} \\ 0 & 0 & d_{33} \\ 0 & d_{15} & 0 \\ d_{15} & 0 & 0 \\ 0 & 0 & 0 \end{bmatrix} \begin{bmatrix} E_1 \\ E_2 \\ E_3 \end{bmatrix} , \quad (1.8)$$

$$\begin{bmatrix} D_1 \\ D_2 \\ D_3 \end{bmatrix} = \begin{bmatrix} 0 & 0 & 0 & 0 & d_{15} & 0 \\ 0 & 0 & 0 & d_{15} & 0 & 0 \\ d_{31} & d_{31} & d_{33} & 0 & 0 & 0 \end{bmatrix} \begin{bmatrix} \xi_1 \\ \xi_2 \\ \xi_3 \\ \xi_4 \\ \xi_5 \\ \xi_6 \end{bmatrix} + \begin{bmatrix} \varepsilon_{11}^{\xi} & 0 & 0 \\ 0 & \varepsilon_{11}^{\xi} & 0 \\ 0 & 0 & \varepsilon_{33}^{\xi} \end{bmatrix} \begin{bmatrix} E_1 \\ E_2 \\ E_3 \end{bmatrix} . \quad (1.9)$$

The piezoelectric strain constant, d, is defined as the ratio of developed free strain to the applied electric field. The subscript of d_{mi} implies that the electric field is applied or charge is collected in the m direction for a displacement of force in the i direction.

The transduction matrix in Eq. (1.9) applies to PZT materials. For transducers made of PVDF materials, this matrix should be modified to [30]

$$\begin{bmatrix} 0 & 0 & 0 & 0 & d_{15} & 0 \\ 0 & 0 & 0 & d_{24} & 0 & 0 \\ d_{31} & d_{32} & d_{33} & 0 & 0 & 0 \end{bmatrix} . \quad (1.10)$$

This reflects the fact that in PVDF films the induced strain is non-isotropic on the surface of the film. Hence, an electric field applied in the direction of the polarization vector will result indifferent strains in **1** and **2** directions.

1.3.3 Piezoelectric Coefficients

The physical meaning of various piezoelectric coefficients (d_{ij}, g_{ij}, s_{ij}, and ε_{ij}) introduced in the previous section will be reviewed in this section. These coefficients play an important role in the performance of the piezoelectric material [31].

1.3.3.1 Piezoelectric Constant, d_{ij}

The piezoelectric coefficient d_{ij} is the ratio of the strain in the j-axis to the electric field applied along the i-axis, when all the external stresses are held constant. In Fig. 1.4, a voltage of V is applied to a piezoelectric transducer which is polarized in direction **3**. This voltage generates the electric field

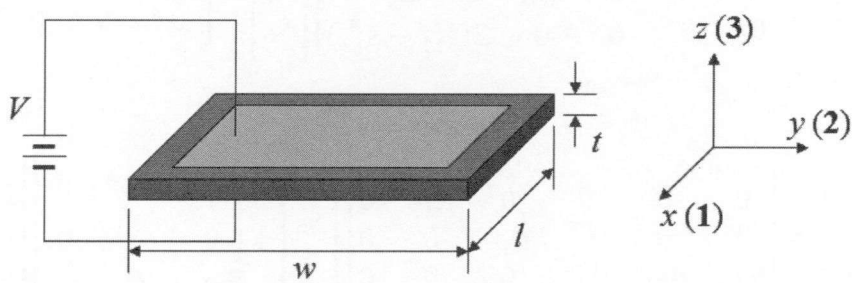

Fig. 1.4 A piezoelectric transducer arrangement used for d_{31} measurement

$$E_3 = \frac{V}{t} \tag{1.11}$$

which strains the transducer. t represents a thickness of the transducer. In particular

$$S_1 = \frac{\Delta l}{l} \tag{1.12}$$

where l is length of the transducer for direction **1**, and Δl represents a length deformation in which

$$\Delta l = \frac{d_{31} V l}{t} \quad . \tag{1.13}$$

The piezoelectric constant d_{31} is usually a negative number. This is due to the fact that application of a positive electric field will generate a positive strain in direction **3**.

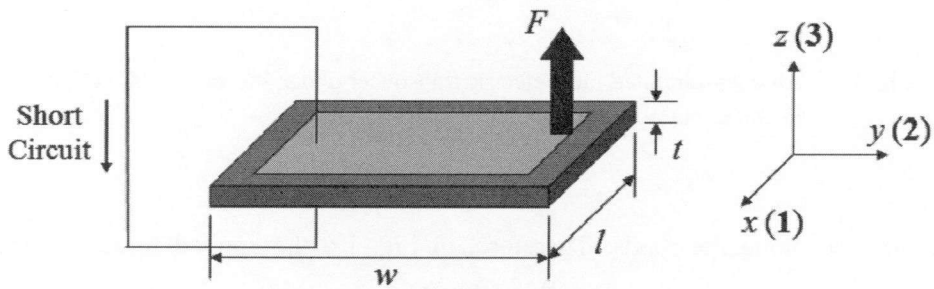

Fig. 1.5 Charge deposition on a piezoelectric transducer – an equal, but opposite force, ***F***, is not shown.

Another interpretation of d_{ij} is the ratio of short circuit charge per unit area flowing between connected electrodes perpendicular to the j direction to the stress applied in the i direction. As shown in Fig. 1.5, once a force ***F*** is applied to the transducer, in the **3** direction, it generates the stress ξ;

$$\xi_3 = \frac{F}{lw} \quad , \tag{1.13}$$

where w is a width of the transducer which results in the electric charge

$$q = d_{33} F \tag{1.14}$$

flowing through the short circuit. If a stress is applied equally in **1**, **2**, and **3** directions, and the electrodes are perpendicular to axis **3**, the resulting short-circuit charge per unit area divided by the applied stressed is denoted by d_p.

1.3.3.2 Piezoelectric Constant, g_{ij}

The piezoelectric constant g_{ij} signifies the electric field developed along the i-axis when the

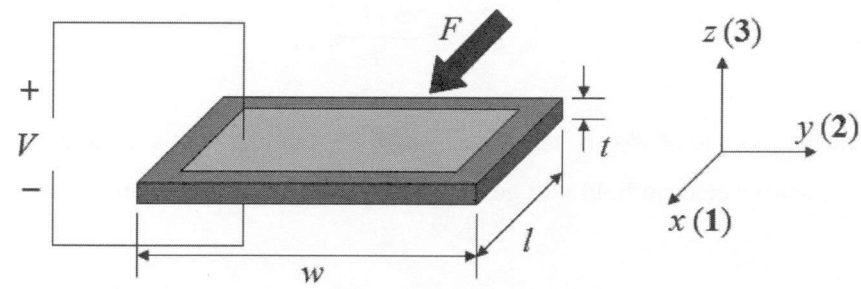

Fig. 1.6 An open-circuited piezoelectric transducer under a force $\boldsymbol{F}$ in direction **1** – an equal, but opposite force, $\boldsymbol{F}$, is not shown.

material is stressed along the j-axis. Therefore, in Fig. 1.6 the applied force $\boldsymbol{F}$, results in the voltage

$$V = \frac{g_{31} F}{w} \,. \tag{1.15}$$

Another interpretation of g_{ij} is the ratio of strain developed along the j-axis to the charge per unit area deposited on electrodes perpendicular to the i-axis. Therefore, in Fig. 1.7, if an electric charge q is deposited on the surface electrodes, the thickness of the piezoelectric element changes by

$$\Delta l = \frac{g_{31} q}{w} \,. \tag{1.16}$$

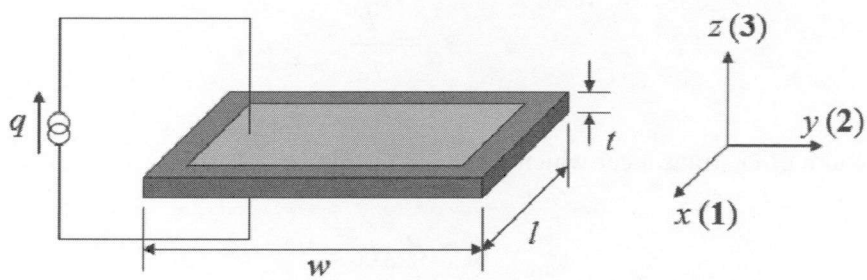

Fig. 1.7 A piezoelectric transducer subject to applied charge

1.3.3.3 Elastic Compliance, s_{ij}

The elastic compliance constant s_{ij} is the ratio of the strain in the i-direction to the stress in the j-direction, given that there is no change of stress along the other two directions. Direct strains and stresses are denoted by indices **1** to **3**. Shear strains and stresses are denoted by indices **4** to **6**.

Subsequently, s_{12} signifies the direct strain in the **1**-axis when the device stressed along the **2**-axis, and stresses along directions **1** and **3** are unchanged. Similarly, s_{44} refers to the shear strain around the **2**-axis due to the shear stress around the same axis.

A superscript, ***E***, is used to state that the elastic compliance s_{ij}^{E} is measured with the electrodes short-circuited. Similarly, the superscript, ***D***, in s_{ij}^{D} denotes that the measurements were taken when the electrodes were left open-circuited. A mechanical stress results in an electrical response that can increase the resultant strain. Therefore, it is natural to expect s_{ij}^{E} to be smaller than s_{ij}^{D}. That is, a short-circuited piezo has a smaller Young's modulus of elasticity than that obtained when it is open-circuited.

1.3.3.4 Dielectric Coefficient, e_{ij}

The dielectric coefficient e_{ij} determines the charge per unit area perpendicular to the *i*-axis due to an electric field applied along the *j*-axis. In most piezoelectric materials, an electric field applied along the *j*-axis causes electric displacement only in that direction. The relative dielectric constant is defined as the ratio of the absolute permittivity of the material by the permittivity of free space. The superscript of ε in ε_{11}^{ξ} refers to the permittivity for an electric field applied in the **1** direction, when the material is not restrained.

1.4 Applications of Piezoelectric Materials

The discovery of piezoelectricity generated significant interest within the European scientific community. Subsequently, roughly within 30 years of its discovery, and prior World War I, the study of piezoelectricity was viewed as a credible scientific activity. The first serious application for piezoelectric materials an ultrasonic submarine detector appeared during World War I was built by Paul Langevin and his co-workers in France. This device was used to transmit a high-frequency chirp signal into the water and to measure the depth by timing the return echo. Since then piezoelectric crystals were employed in many classic applications such as sonar applications, frequency stabilizers, ultrasonic transducers, microphones, accelerometers, piezo-ignition systems, sensitive hydrophones and ceramic phono cartridges *etc* [32].

Piezoelectric vibration control has shown promise in a variety of applications ranging from consumer, sporting products, and satellite vibration control systems. Some of the companies like HEAD and K2 have invested in high-performance and novelty items such as composite

piezoelectric tennis racquets, skis, and snowboards. These products typically involve the use of a shunted piezoelectric transducer to decrease vibration, which will increase the user comfort, better handling and performance [32].

Figure 1.8 (a) shows the design of the shoe energy harvesting system, which contains the PVDF piezoelectric film insert and metal spring with coupled generator system. This PVDF insert in the shoe is used to recover some of the power n the process of walking. The natural flexing of the shoe when walking provides the necessary deflection for generating power from the piezoelectric film insert [33]. Fig. 1.8 (b) shows the magic backpack, the straps of this backpack are made using PVDF, generating electrical charges when stress is applied [34]. These nylon-like straps convert that mechanical strain into electrical energy, and researchers have figured out that if you carry a 100 pound pack and walk at 2~3 mph you can generate 45.6 mW of power. That is enough to the power of portable electronic devices, or a head-mounted flashlight.

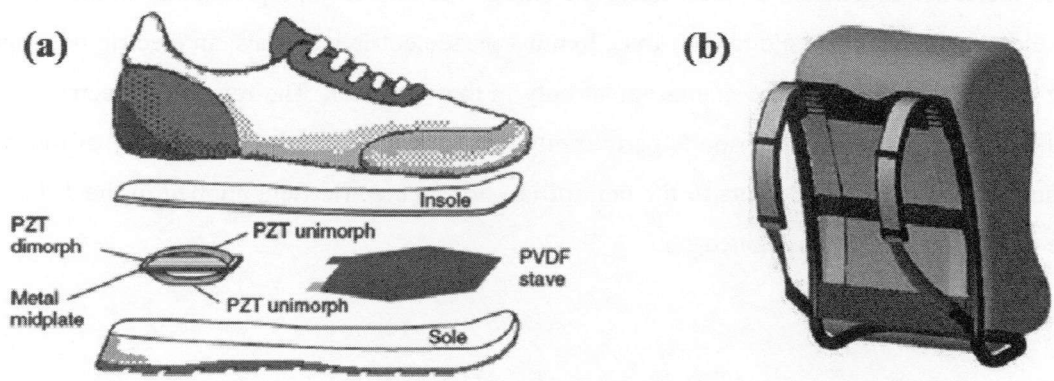

Fig. 1.8 Applications of piezoelectric materials; (a) shoe energy harvesting system (from [28]), and (b) magic backpack straps power generator (from [29])

1.5 Outline of Dissertation

This dissertation describes the results of my studies on the development of a piezoelectric acoustic energy harvester for the fundamental frequency band of a human voice. For a voice of a comparatively low frequency, the diaphragm of the energy harvesters must have high sensitivity to a low acoustic pressure. For this reason, a piezoelectric polymer with lower mechanical impedance than other piezoelectric materials was used in these studies; P(VDF-TeFE) was employed which is a PVDF copolymer. Since the diaphragm of the device fabricated in these studies did not include an elastic substrate, the piezoelectric film had to be sufficiently thin and flat, and chemically pure. This dissertation is organized as follows.

In Chapter 2, the experimental techniques used to form a P(VDF-TeFE) films using the sol-gel method are described. To control the film thickness by applying a spin-coating method, mixtures of solvents were used as casting solutions. Film surfaces were characterized as a function of the annealing temperature. The effect of using mixed casting solutions was also investigated by employing X-ray photoelectron spectroscopy (XPS) and Fourier transform infrared spectroscopy (FTIR).

In Chapter 3, solutions to the issues raised in Chapter 2 are discussed along with a proposed the improved annealing process that removes impurities while preserving the piezoelectric characteristics of the P(VDF-TeFE) film.

In Chapter 4, the design and fabrication of an acoustic energy harvester using MEMS techniques are reported at the fundamental frequency of a human voice. The properties of the devices were measured and characterized experimentally. Also, improvements of the device are discussed along with the energy conversion efficiency calculated from the measured properties.

In Chapter 5, the main conclusions of the present study are described.

References

[1] J.A. Paradiso, "Energy Scavenging for mobile and Wireless Electronics," Massachusetts Institute of Technology Media Laboratory Thad Starner, Georgia Institute of Technology, GVU Center (2008).

[2] C.B. Williams, "Development of an electromagnetic micro-generator," IEEE Proc. Circuits, Devices and Systems **148**(6), 337 (2001).

[3] R. Amirtharajah and A. Chandrakasan, "Self-Powered Signal Processing Using Vibration-Based Power Generation," IEEE J. Solid-State Circuits **33**(5), 687 (1998).

[4] S.J. Roundy, "Energy Scavenging for wireless sensor nodes with a focus on vibration to electricity Conversion," Doctoral dissertation, Dept. of Mechanical Eng., Univ. of California, Berkeley (2003).

[5] N.S. Schenck and J.A. Paradiso, "Energy scavenging with shoe-mounted piezoelectrics," IEEE Micro. **21**(3), 30 (2001).

[6] P. Chapman and M. Raju, "Designing power systems to meet energy harvesting needs," TechOnline India **8**, 42 (2008).

[7] S. Horowitz, A. Kasyap, D. Johnson, T. Nishida, K. Ngo, M. Shelplak, and L. Cattafesta, "Technology Development for Self-powered Sensors," AIAA 1st Flow Control Conference, AIAA Paper 2002 (2002).

[8] R. Taylor, F. Liu, S. Horowitz, K. Ngo, T. Nishida, L. Cattafesta, and M. Sheplak, "Technology Development for Electromechanical Acoustic Liners," Proc. ACTIVE '04, Paper A04-093 (2004).

[9] H. Traunmüller and A. Eriksson, "The frequency range of the voice fundamental in the speech of male and female adults," unpublished manuscript, can be retrieved from http://www2.ling.su.se/staff/hartmut/aktupub.htm (1995).

[10] S. Olcum, M. N. Senlik, and A. Atalar, "Optimization of the Gain-Bandwidth Product of Capacitive Micromachined Ultrasonic Transducers," IEEE Trans. Ultrason., Ferroelect., Freq. Contr. **46**, 1364 (1990).

[11] Morris H. Shamos and Leroy S. Vavine, "Piezoelectricity as a Fundamental Property of Biological Tissues," Nature **213**, 267 (1967).

[12] H. Kawai, "The Piezoelectricity of PVDF," Jpn. J. Appl. Phys. **8**, 975 (1969).

[13] N. Murayama, R. Nakamura, H. Obara, and M. Segawa, "The Strong Piezoelectricity in PVDF," Ultrasonics **14**, 15 (1976).

[14] T. Furukawa, J. Aiba, E. Fukada, "Piezoelectric relaxation in polyvinylidene fluoride," J. Appl. Phys. **50**, 3615 (1979).

[15] E. Fukada, and T. Furukawa, "Piezoelectricity and Ferroelectricity in Polyvinylidene Fluoride," Ultrasonics **19**, 31 (1981).

[16] Y. Wada, and R. Hayakawa, "Piezoelectricity and pyroelectricity of polymers," Jpn. J. Appl. Phys. **15**, 2041 (1976).

[17] C. Lynch, "Polyvinylidene Fluoride (PVDF) Elastic, Piezoelectric, Pyroelectric, and Dielectric Coefficients and Their Non-Linearities," Ferroelectrics **150**, 331 (1993).

[18] R. Ewing, "The electrocaloric effect on the pyroelectric charge in polyvinylidene fluoride,"

Ferroelectric **141**, 243 (1993).

[19] H. Sasabe, T. Nakayama, K. Kumazawa, S. Miyata, and E. Fukada, "Photovoltaic effect in Poly(vinylidene fluoride)," Polymer Journal **13**, 967 (1981).

[20] M. Toda, "Elastic Properties of Piezoelectric PVF_2," J. Appl. Phys. **51**, 4673 (1980).

[21] A. Bune, V. Fridkin, and K. Verkhovskaya, "Some investigations of photoelectric and optic properties in the ferroelectric PVDF," Ferroelectrics **81**, 361 (1988).

[22] J. B. Lando and W. W. Doll, "The polymorphism of poly(vinylidene fluoride). I. the effect of head-to-head structure," J. Macromolecular science-Physics B **2**, 205 (1968).

[23] A. J. Lovinger, G. T. Davis, T. Furukawa, and M. G. Broadhurst, "Crystalline forms in a copolymer of vinylidene fluoride and trifluoroethylene (52/48 mol %)," Macromolecules **15**, 323 (1982) .

[24] B. L. Farmer, A. J. Hopfinger, and J. B. Lando, "Polymorphism of poly(vinylidene fluoride): potential energy calculations of the effects of head-to-head units on the chain conformation and packing of poly(vinylidene fluoride)," J. Appl. Phys. **43**, 4293 (1972).

[25] K. Tashiro, "Ferroelectric polymers," H. S. Nalwa, Ed., Macrel Dekker, New York (1995).

[26] J. F. Legrand, "Structure and ferroelectric properties of P(VDF-TrFE) copolymers," Ferroelectrics **91**, 303 (1989).

[27] M. A. Bachmann and J. B. Lando, "A reexamination of the crystal of phase II of poly(vinylidene fluoride)," Macromolecules **14**, 40 (1981).

[28] T. T. Wang, J. M. Herbert, and A. M. Glass, "The Application of Ferroelectric Polymers," The Blackie Publishing Group, Glasgow, London (1988).

[29] P. E. Bloomfield, "Production of ferroelectric oriented PVDF films," J. Plastic Film and Sheeting **3**, 123 (1988).

[30] R. G. Kepler, R. A. Anderson, "Ferroelectric polymers," Advances in Phys. **41**, 1 (1992).

[31] G. W. Taylor, J. J. Gagnepain, T. R. Meeker, T. Nakamura, and L. A. Shuvalov, "Piezoelectricity," Gordon and Breach, Science Publisher, Inc., New York (1985).

[32] T. Ikeda, "Fundamental of Piezoelectricity," Oxford University Press, USA (1990).

[33] S. O. R. Moheimani and A. J. Fleming, "Piezoelectric Transducer for Vibration Control and Damping," Springer, London (2006).

[34] T. Starner, "Human powered wearable computing," IBM Systems Journal **35**, NOS 3&4 (1996).

[35] H. A. Sodano, G. Park, and D. J. Inman, "Estimation of Electric Charge Output for Piezoelectric Energy Harvesting," Strain **40**, 49 (2004).

Chapter 2

Formation of Poly(vinylidene fluoride - tetrafluoroethylene) Thin Films with Sol-Gel Method

2.1 Introduction

Poly(vinylidene fluoride – tetrafluoroethylene) (P(VDF-TeFE)) is a copolymer of vinylidene fluoride (VDF, CH_2–CF_2) and tetrafluoroethylene (TeFE, CF_2–CF_2) as shown in Fig. 2.1. Unlike VDF, TeFE has no polarity. However, P(VDF-TeFE) can be grown with those of higher crystallinity [1], resulting in greater polarization and a stronger piezoelectric response than those of the semicrystalline PVDF. Compared with the known copolymers, P(VDF-TeFE) is one of the most widely used ferroelectric PVDF copolymers [2].

In an attempt to understand the structure-property relation of P(VDF-TeFE) theoretically, Balta-Calleja *et al.* [3] studied the structure and properties using potential energy calculations to determine the chain conformation and packing energies. They showed that the introduction of TeFE may cause the formation of all-*trans* chains with a lower energy conformation. The great proportion of bulky tetra-fluoride groups in the copolymer will prevent the chains from accommodating the α-chain conformation (or **TGTG'**, where **G** refers to *gauche* and **T** refers to

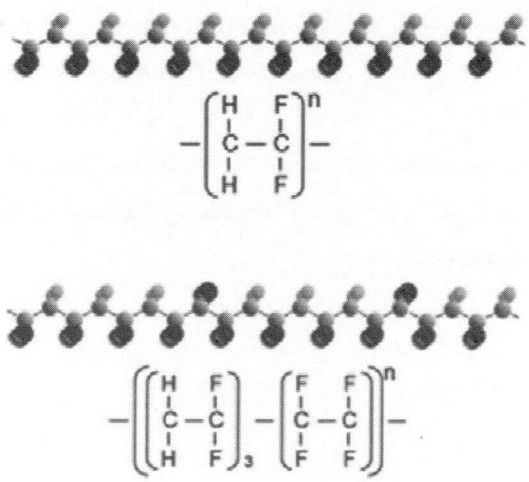

Fig. 2.1 A molecular structure of PVDF (top side) and P(VDF-TeFE) (bottom side)

trans, and the prime in **G'** refers to the dihedral angle being opposite to the **G** conformation with respect to the reference plane **T**). Therefore, the copolymers can directly crystallize at room temperature into a ferroelectric β-phase [3, 4] that possesses polar unit cells (similar to the β-phase of PVDF homopolymer). The copolymer can also be electroprocessed into an enhanced piezoelectric material immediately after crystallization. Ranjan *et al.* [5] calculated the total energy of the α- and β-phases of PVDF and P(VDF-TeFE). The results of their total energy calculation are summarized in Fig. 2.2, which shows the energy difference between the α-and β-phases of PVDF-TeFE as a function of TeFE concentration. The α-phase is lower in energy and hence is the more stable phase in the limit of pure PVDF (TeFE concentration = 0). The transition from the α-phase to the β-phase takes place at TeFE concentration of 12%. In this study, P(VDF-TeFE) (75/25) is

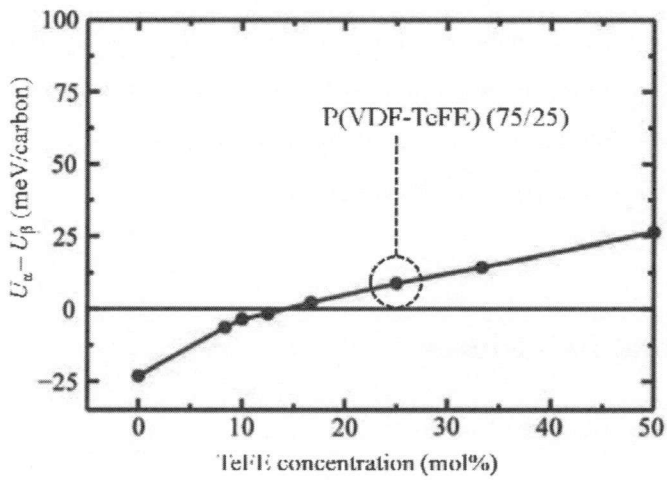

Fig. 2.2 Calculated total energy difference between the α and β phases as a function of TeFE concentration in P(VDF-TeFE) (from [5])

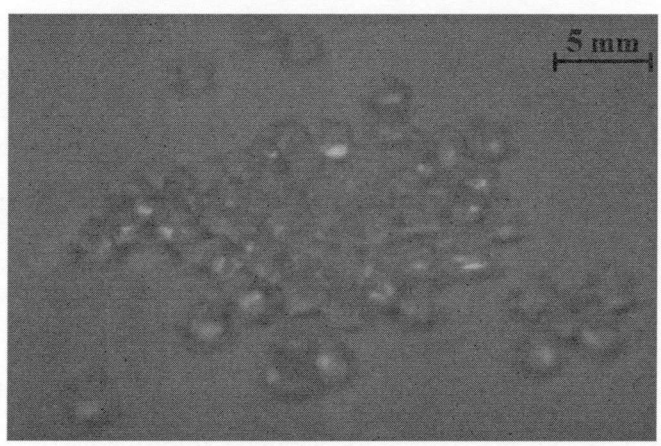

Fig. 2.3 A typical photograph showing granules of P(VDF-TeFE)

used to denote a TeFE concentration of 25%. Note that in general a smaller electric field is required for the $\alpha - \beta$ conversion in the P(VDF-TeFE) than that in PVDF. For this reason, P(VDF-TeFE) is used to form the diaphragm of the acoustic energy harvester in this study.

In this chapter, we discuss the formation of P(VDF-TeFE) thin films using the sol-gel process. Granular P(VDF-TeFE), as shown in Fig. 2.3, was provided by Daikin Co. Ltd. To control the thickness of the thin films, the concentrations of the casting solvents and the coating speed in the spin-coating process were adjusted as controllable parameters in the sol-gel method. To control the thickness of thin films, it is easier to adjust the concentration of the casting solutions than to adjust the coating speed. However, it was observed that when the film which was in the sol-state on the surface of the substrate, it became detached during spin-coating. Since this phenomenon is related to the viscosity of the solvents employed to cast the polymer [6], a reasonable mixing ratio for easily forming a thin film was investigated by mixing two different solvents. Furthermore, it was observed that the surface morphology of the thin film could be improved by controlling the annealing temperature. Finally, the effects of the concentrations of the mixed solvents on the properties of the formed film were investigated experimentally.

2.2 Experimental Procedures

2.2.1 Preparation of Casting Solvents

The formation of P(VDF-TeFE) films by the sol-gel process, a methyl-ethyl-ketone (MEK) is generally used as a solvent [6]. MEK is a chemically stable compound also known as 2-butanone. It has very good solvent properties, a high evaporation rate, and is miscible with organic solvents. Its solubility is very high because of its low viscosity; the properties of MEK are listed in Table 2.1. However, the probability of rearrangement of the polymer chain is reduced by its high solubility. Furthermore, in the case of using a low-concentration casting solution, a film may not be formed or many pinholes form on the surface of the film even when an annealing process is carried out [5]. In this study, an n, n-dimethylacetamide (DMAc) is added to MEK to control the viscosity of the casting solvents as above.

DMAc is a good solvent for a wide range of organic and inorganic compounds, and it is miscible with water, ethers, esters, ketones, and aromatic compounds. However, since the boiling point of DMAc is 165 °C, there is the possibility of solvent remaining in the formed film when DMAc is used in the sol-gel process. Hence, to evaporate all of the DMAc solvent, the annealing must be carried out at a temperature higher than 165 °C. As reported in the section 2.4, the

existence of remaining solvents was investigated for the cases of a mixed solvent and a single solvent.

Table 2.1 Casting solvents [7]

IUPAC name	Methyl-ethyl-ketone	N, N-Dimethylacetamide
Structure	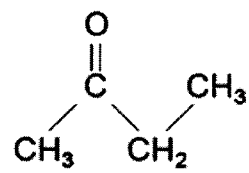	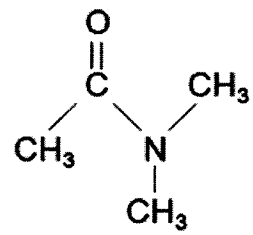
Density	0.81 g/cm^3	0.94 g/cm^3
Boiling Pt.	80 °C	165 °C
Melting Pt.	- 86 °C	- 20 °C
Viscosity	0.43 cP @ 20 °C	0.92 ~ 2.14 cP @ 20 °C
Vapor pressure	74 Torr	1 Torr
Solubility of water	12 % w/w	100 % w/w

2.2.2 Film Coating Process of P(VDF-TeFE)

By varying the mixing ratio of MEK to DMAc, five different casting solutions of P(VDF-TeFE) were made up. The mixing ratios and their names in this study are as follows:

- MEK: 100 wt% (call as K100 single solvent),
- MEK: 75 wt% + DMAc: 25 wt% (call as KD7525 mixed solvent),
- MEK: 50 wt% + DMAc: 50 wt% (call as KD50 mixed solvent),
- MEK: 25 wt% + DMAc: 75 wt% (call as KD2575 mixed solvent),
- DMAc: 100 wt% (call as D100 single solvent).

The concentrations of the casting solutions are classified into two categories: high-concentration (10, 15, and 20 wt%) and low concentration (6 wt% and less). A film was always formed when using one of the high-concentration casting solutions, whereas a film was only

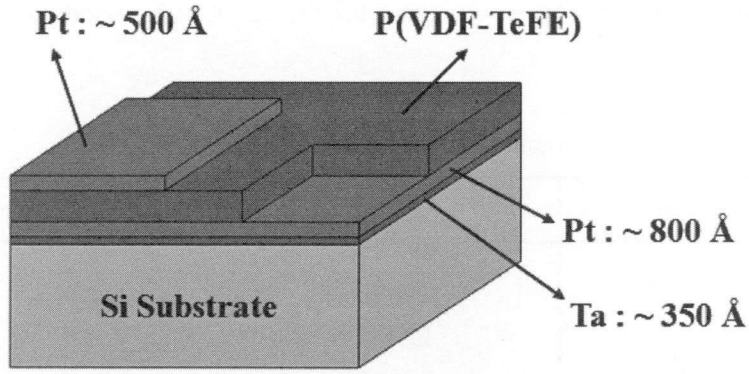

Fig. 2.4 A schematic diagram showing a lumped structure of P(VDF-TeFE) spin-coated on Pt/Ta-deposited Si substrate

sometimes formed when using the low-concentration casting solutions, depending on the mixing ratio of the solvents. For the casting solutions with a concentration over 20 wt%, a film could not be formed by spin-coating because of the poor adhesion between the film and substrate.

Using the five casting solutions, P(VDF-TeFE) thin films were formed on the surface of a Pt/Ta-deposited Si substrate by a standard spin-coating process as shown in Fig. 2.4. The initial spin-coating speed was kept at 1,000 rpm for 5 seconds and the terminal speed was set at 2,000, 3,000, 4,000, or 5,000 rpm for 15 seconds. To reduce the likelihood of defects forming on the film surface during the spin-coating process, induced by moisture in the atmosphere, the spin-coater was filled with before the spin-coating process. DMAc is miscible with water (100% w/w (weight/weight)), thus it is very hygroscopic. In other words, the sol-state P(VDF-TeFE) film cast with DMAc as a single solvent or a mixed solvent is vulnerable to humidity.

After the spin-coating process, an annealing process was carried out to form a β-phase film of P(VDF-TeFE). As discussed in the section 2.3, "treating thickness measurements, according to the previous study [6]," the annealing process was carried out at 120 °C for 1 hour. Alternatively as discussed in the section 2.4, "treating a roughness of the film surface," the annealing process was carried out at 120, 175, or 215 °C for 1 hour to observe the relation between the annealing temperature and the roughness of the film surface.

2.3 Film Thickness Measurement to Optimize Spin-Coating Condition

Classifying the casting solutions into high and low concentrations, the thickness of the deposited P(VDF-TeFE) film was measured by the profile meter (Alpha-Step® 500). Fig. 2.5 shows the measured film thicknesses for the high-concentration casting solutions.

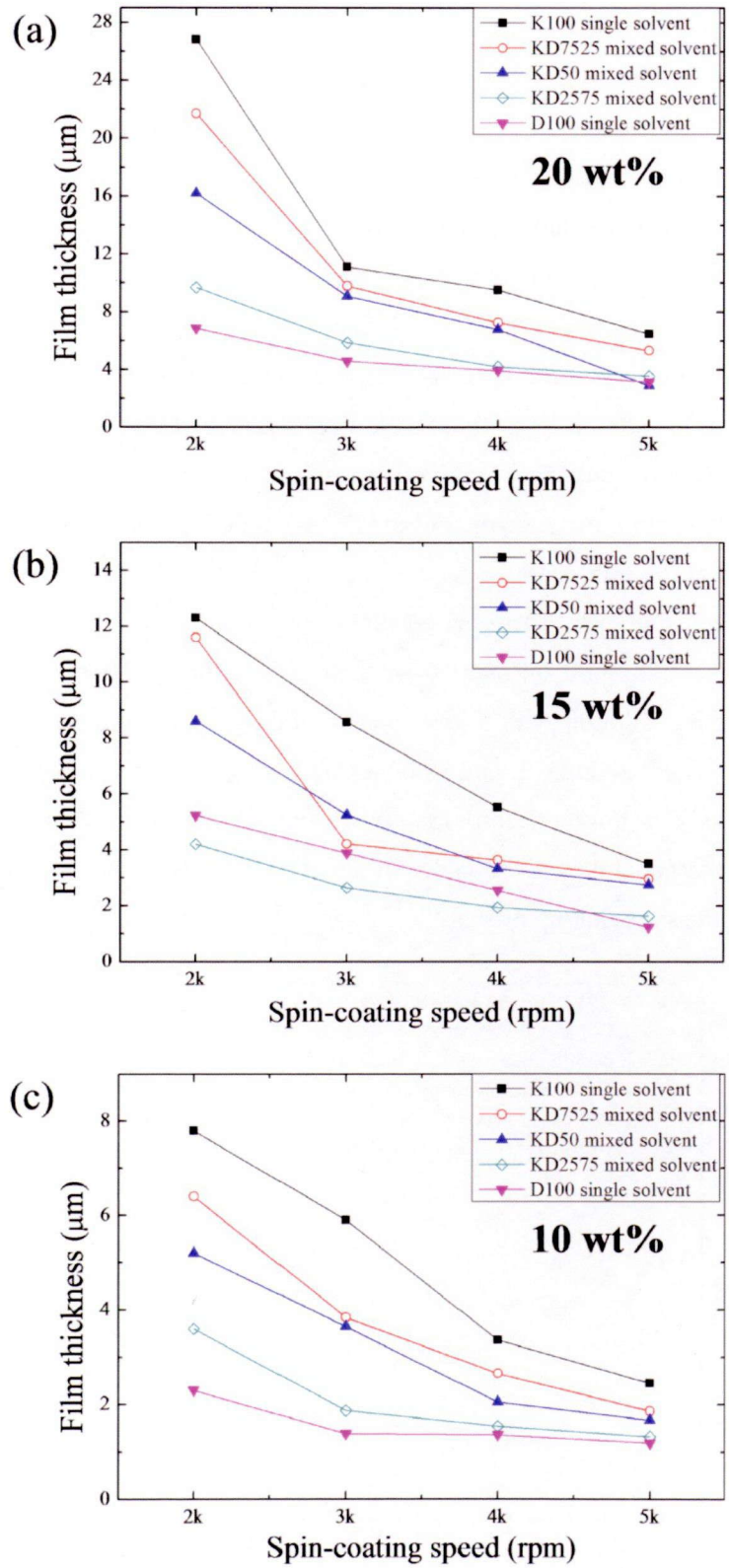

Fig. 2.5 Thickness of P(VDF-TeFE) films spin-coated with various casting solvents as a function of the spin-coating speed for (a) 20 wt%, (b) 15 wt%, and (c) 10 wt% concentration of the casting solution

For the casting solutions with 20 wt% concentration, as shown in Fig. 2.5 (a), the film thickness decreased slightly with increasing spin-coating speed because of the high viscosity of the casting solutions. Considering that the spin-coating process began in earnest at a speed of 2,800 rpm, there were clear changes in the film thickness with the spin-coating speed that depend on the concentration of the casting solutions. The film thickness for the D100 single solvent was less affected by the spin-coating speed than that for the other solvents. However, the film thickness had already reached about 1 μm for the casting solution with 15 wt% concentration, and could not be well controlled when the concentration of the casting solution was less than 15 wt%, as shown in Figs. 2.5 (b) and (c). In addition, even though the film was annealed after the spin-coating process, the film detached from the substrate surface because the adhesion of the spin-coated film to the metal surface was low. With the exception of the D100 single solvent, the measured film thickness was in proportional to the spin-coating speed.

For all the casting solutions, the measured film thickness exceeded 1 μm when using a casting solution with a concentration higher than 10 wt%. Since the film thickness must be less than 1 μm in this study, a casting solution with a low concentration is more suitable for the present study. However, using the KD50, KD2575, and D100 as the casting solvents, no film was formed by the spin-coating process at a low concentration. When the ratio of DMAc was higher than that of MEK, there were interfacial delamination occurred between the substrate and the sol-state P(VDF-TeFE) film during the spin-coating process.

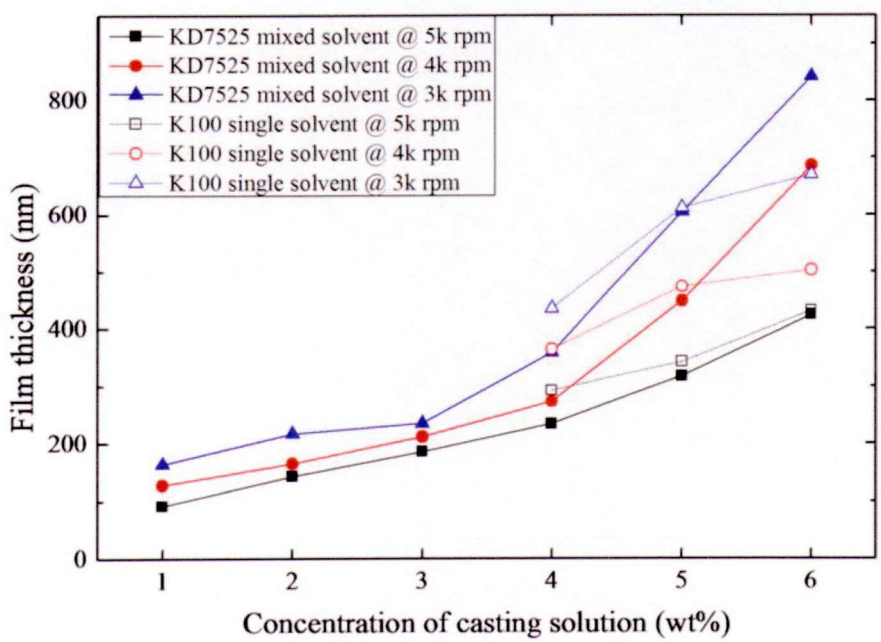

Fig. 2.6 Casting solution concentration dependence of the thickness of the P(VDF-TeFE) film spin-coated with various casting solvents in the low-concentration category

For the low-concentration P(VDF-TeFE) casting solutions, the thickness of the films formed using the K100 single solvent and KD7525 mixed solvent is shown in Fig. 2.6 as a function of the concentration of the casting solutions. Interfacial delamination occurred in the P(VDF-TeFE) film formed using the K100 single solvent. Only the solution cast with the KD7525 mixed solvent resulted in a film via the spin-coating process at a concentration of 3 wt% and less. In the case of the KD7525 mixed solvent, a film was formed at a concentration of 0.5 wt%, while islandlike holes originating from interfacial delamination were formed on the film surface. For the spin-coating speed of 5,000 rpm, it was found that the KD7525 mixed casting solution could be used to effectively control the film thickness. As a result, adjustment of the viscosity through the mixing of solvents is helpful for controlling the film thickness. Since, there have been very few experimental reports on the sol-gel process using mixed solvents, the effects of mixed solvents on the film properties should be investigated in detail. To carry out such an investigation, the two solvents for which P(VDF-TeFE) films formed, i.e., the K100 single solvent and KD7525 mixed solvent, were compared as discussed in the section 2.5.

2.4 Annealing Temperature Dependence of Surface Morphology of P(VDF-TeFE) Films

A P(VDF-TeFE) is known to be more stable in the β-phase, in contrast to PVDF [5]. However, the annealing process is an essential prerequisite to change the phase of the film. In the sol-gel process of P(VDF-TeFE), the objective of the annealing process are to remove the remaining solvents in the sol-state film, supply energy for the rearrangement of P(VDF-TeFE) monomers, and planarize the film surface. As reported in this section, the effects of the annealing temperature on the morphology of the film surface were experimentally investigated.

Using 10 wt% casting solution, for which a film can be formed using all five casting solvents (see section 2.2.2), the relationship between the annealing temperature, T_a, (120, 175, or 215 °C) and the average roughness of the film surface was investigated. The results are shown in Fig. 2.7. Here, the temperature of 120 °C is in the range of the general annealing temperature of PVDF copolymers [8], 175 °C is higher than the melting point of PVDF copolymers, and 215 °C is a temperature at which PVDF copolymer can completely melt. With an increase of the annealing temperature, the roughness of the film surface changed markedly. The roughness decreased with increasing DMAc mixing ratio even though the viscosity of a DMAc is higher than that of a MEK. Since the vapor pressure of DMAc is as low as 1 Torr (the vapor pressure of MEK is 74 Torr), the

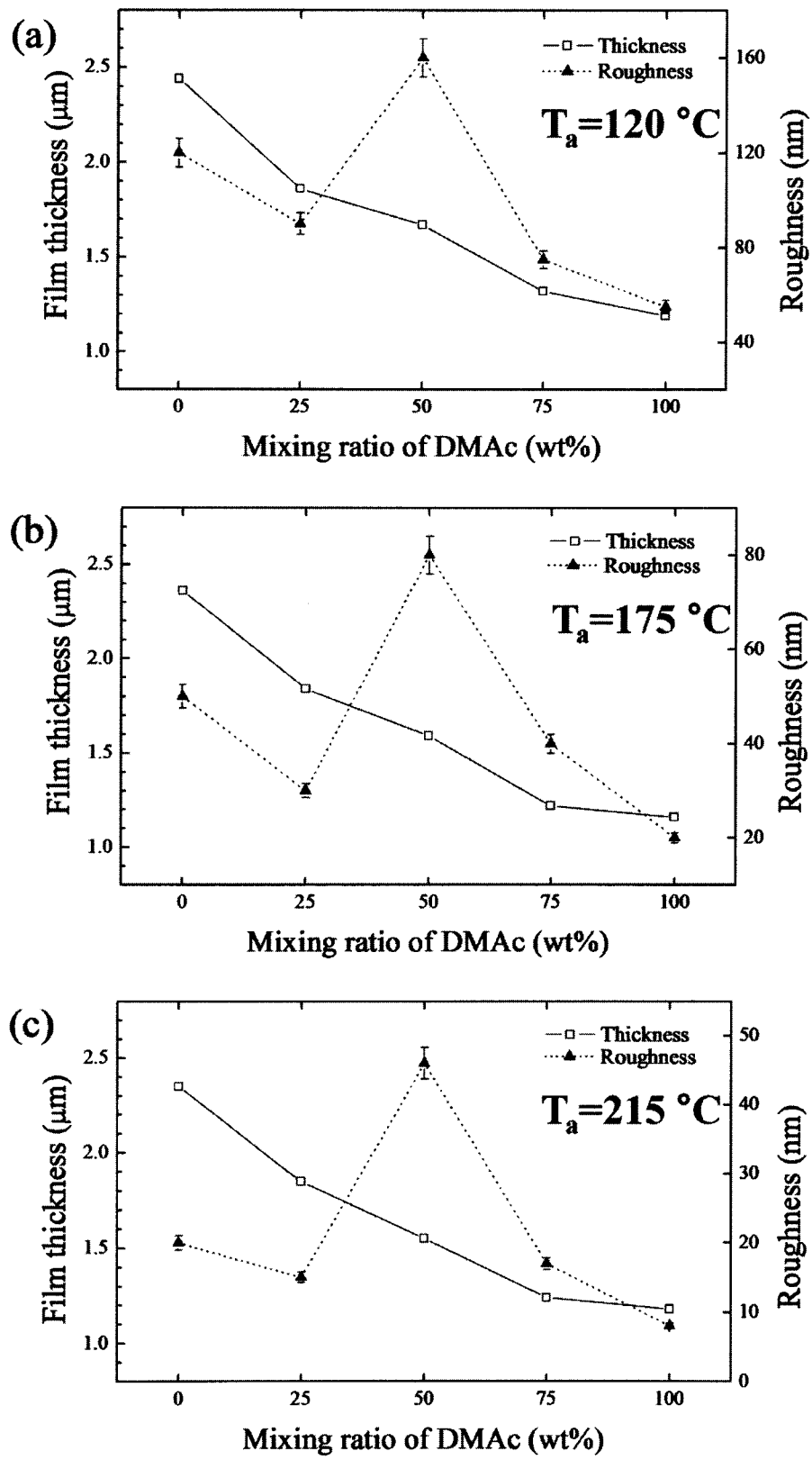

Fig. 2.7 Film thickness and average roughness of the films subsequently annealed at (a) 120 °C, (b) 175 °C, and (c) 215 °C as a function of the mixing ratio of DMAc

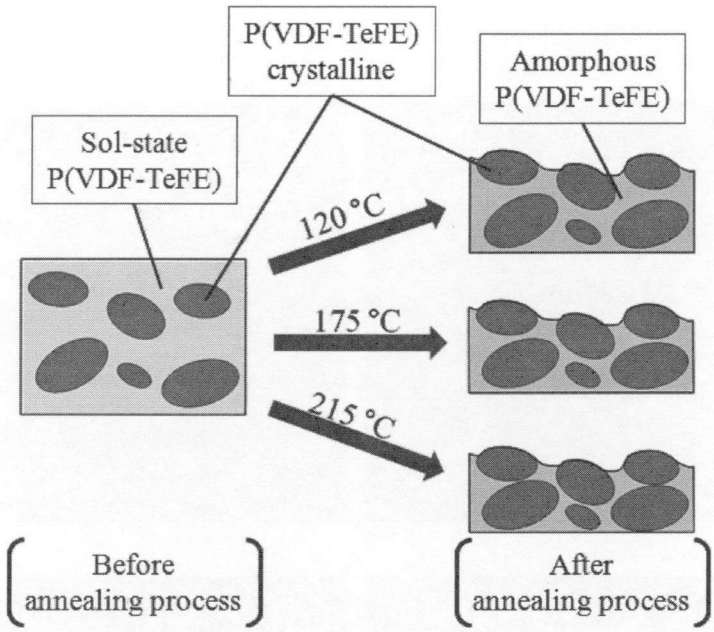

Fig. 2.8 A schematic diagram showing various P(VDF-TeFE) crystalline state for different annealing temperatures

time during which the sol-state P(VDF-TeFE) film is flattened is extended with increasing DMAc mixing ratio. However, in the case of using the KD50 mixed solvent, the film surface was found to be very rough compared with the other cases. The KD50 mixed solvent, which contains the same concentrations of MEK and DMAc, may hinder the planarization of the film. Since the interfacial delamination easily occurred for the cases using the D100 single solvent, the roughness of the film formed with the KD7525 mixed solvent was comparatively low.

With an increase of the annealing temperature, the film thickness slightly decreased. Figure 2.8 shows a schematic diagram of the state inside the film before and after the annealing process. The amorphous-phase P(VDF-TeFE) in the sol-state film contracted during the annealing process. Hence, at annealing temperatures higher than the melting point of a P(VDF-TeFE), it is possible that the film thickness decreased owing to the evaporation of the amorphous-phase P(VDF-TeFE).

For the 4 wt% casting solutions (K100 single solvent and KD7525 mixed solvent), using which P(VDF-TeFE) thin films can be formed, the film surfaces were observed using a scanning electron microscope (SEM, Hitachi High-Technology S-4800). Typical results are shown in Fig. 2.9. The two casting solutions as above produced films with similar decreases in film surface roughness with increasing annealing temperature. However, the films formed with the KD7525 mixed solvent are smoother than those formed with the K100 single solvent. At annealing temperatures of higher than 175 °C, the surface roughness of the film decreased, probably because the annealing

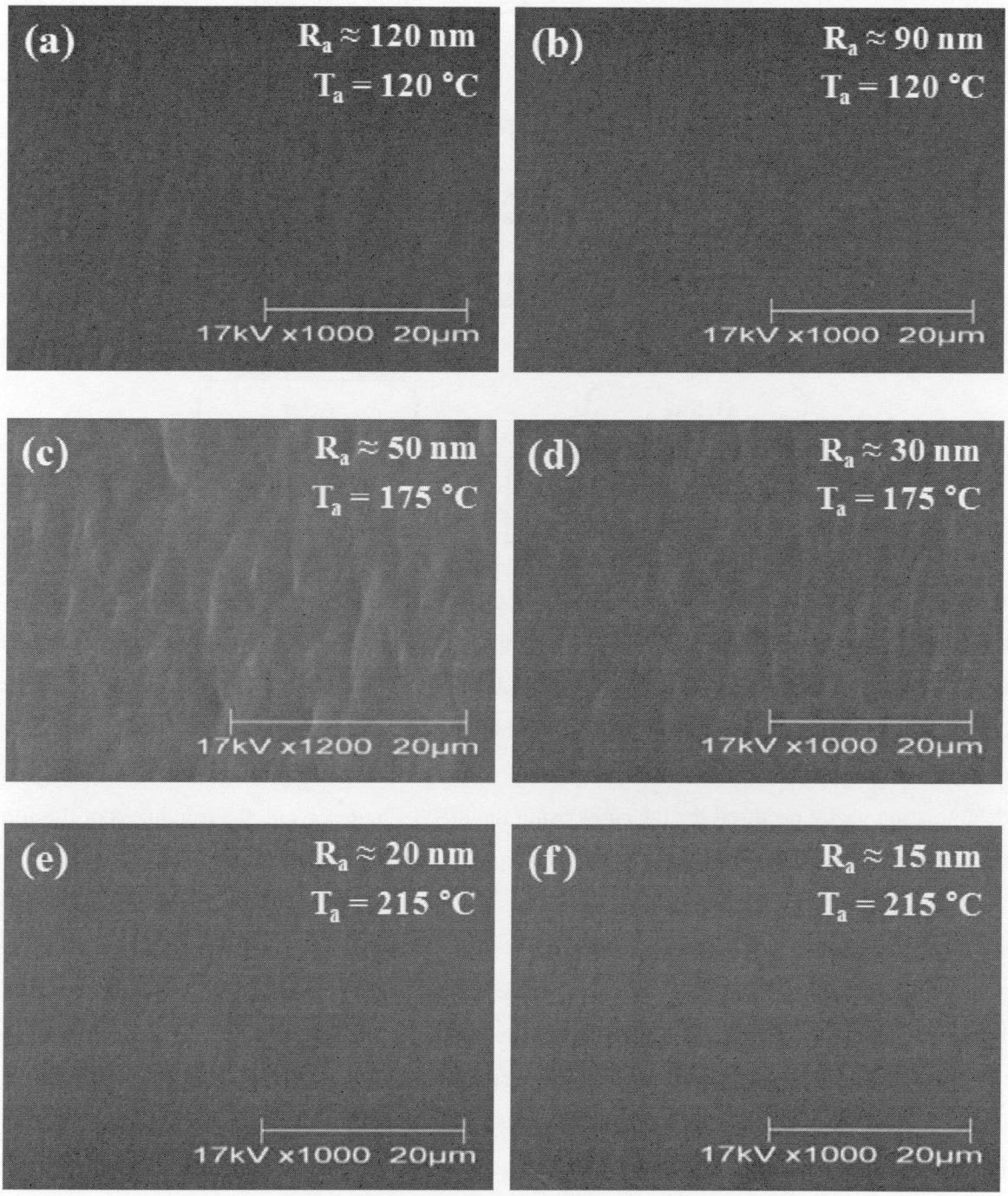

Fig. 2.9 Typical SEM images of the P(VDF-TeFE) film surface annealed at (a), (b) 120°C, (c), (d) 175°C, and (e), (f) 215°C. Samples of (a), (c), and (e) are formed with the K100 single solvent, and samples of (b), (d), and (f) are formed with the KD7525 mixed solvent. The average roughness, R_a, decreased with the increment of the annealing temperature, T_a.

temperature was higher than the melting point of a P(VDF-TeFE). Hence, the film surface can be flattened by melting the P(VDF-TeFE) film. As a result, very flat films can be formed by setting the annealing temperature higher than the melting point. Nevertheless, if the annealing temperature exceeds a certain point, the PVDF copolymer loses its piezoelectric properties [9]. According to the experimental data, the piezoelectricity of a P(VDF-TeFE) is lost at 205 °C. Thus, it is effective that the annealing process is carried out at 195 °C.

2.5 Characterization of Surface and Inside of P(VDF-TeFE) Films

On the surface of a P(VDF-TeFE) film formed by the spin-coating process, a metal film electrode will be deposited as part of a diaphragm. Hence, the film surfaces must be characterized because the film surface becomes the interface between the P(VDF-TeFE) thin film and the top electrode. X-ray photoelectron spectroscopy (XPS, Shimadzu ESCA 850) and the Fourier transform infrared spectroscopy (FTIR, JEOL WIN SPEC-50) were employed to observe the surface and inside of the P(VDF-TeFE) films respectively. In order to examine the films formed with all five casting solutions, P(VDF-TeFE) films were formed using the 10 wt% casting solutions and subsequently annealed at 120, 175, or 215 °C.

Figure 2.10 shows XPS spectra of C_{1s} core electrons whose binding energy is 290.5 eV for the PVDF binder [10] (see Appendix A). Differences in the intensity of the $-CF_2-\underline{C}H_2-CF_2-$ (286.3 eV) and $-CH_2-\underline{C}F_2-CH_2-$ (290.8 eV) peaks, which comprise the VDF structure [11], shows that the surface area is different among the samples treated at different annealing temperatures. The surface area is affected by the grain size of crystalline P(VDF-TeFE). Fig. 2.11 shows the atomic force microscope (AFM) images (Keyence VN-8000) indicating the changes in the grain size of P(VDF-TeFE) with the annealing temperature. The surface area decreases with increasing grain size resulting from the increasing annealing temperature [12]. The $-CF_2-\underline{C}F_2-CF_2-$ peak (292.6 eV) corresponding to the TeFE structure is very small in intensity, and it is hidden by the peaks of the VDF structure. No peaks located at binding energies of less than 285 eV were detected from the normal chain structure of P(VDF-TeFE). The R-$\underline{C}$=O- signal, which has a peak at 282.5 eV [13], represents a carbonyl group and an amide group in the binding structures of a MEK and a DMAc, respectively, indicating the existence of remaining solvents. The bonding structures of both $\underline{C}$-H, which has a peak at 283.5 eV [14], and $\underline{C}$-O-C, which has a peak at 285 eV [15], were detected from the amorphous P(VDF-TeFE) film. The $\underline{C}$-H bonds represent the VDF chain structure along the VDF axis direction, while the $\underline{C}$-O-C bonds are formed by the insertion of O atoms during the recombination or rearrangement of the chain structure of P(VDF-TeFE). In all the graphs in Fig.

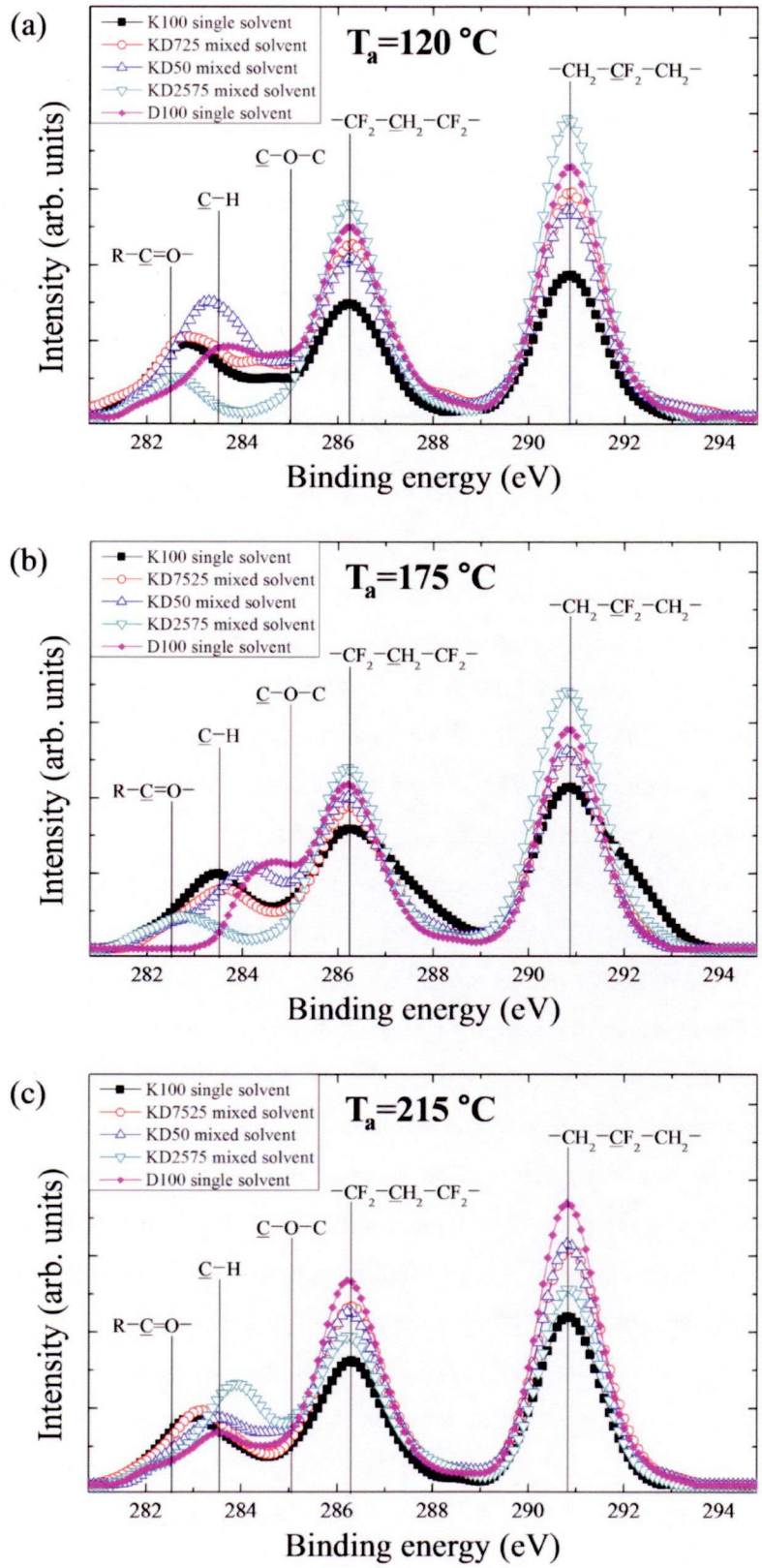

Fig. 2.10 C_{1s} core XPS spectra taken from the films formed with 10 wt% casting solution and subsequently annealed at (a) 120 °C, (b) 175 °C, or (c) 215 °C.

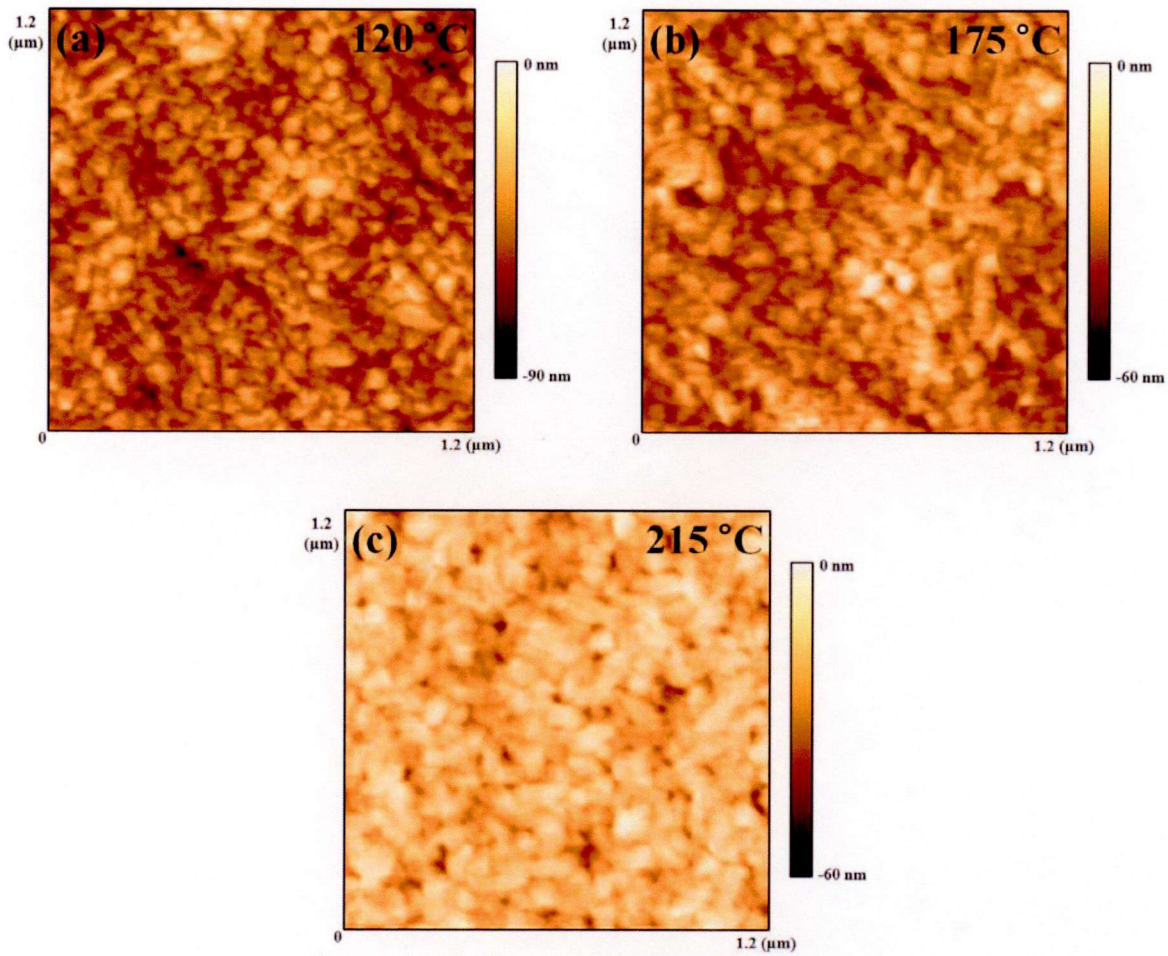

Fig. 2.11 Typical AFM images of the P(VDF-TeFE) film surface annealed at (a) 120 °C, (b) 175 °C, and (c) 215 °C

2.10, hardly any relationship was observed between the peaks related to impurities or solvents and the annealing temperature. Although the film surface roughness decreased with increasing annealing temperature, as discussed in section 2.4, the micro structure of the P(VDF-TeFE) film surface was not well controlled by the subsequent annealing process employed.

Because of the possible existence of C atoms bonded to O atoms, O_{1s} core (533 eV [16]) XPS spectra were also taken. Typical results are shown in Fig. 2.12. Different carbon bonds such as C=O (530.8 eV [15]), R-C=O- (532.4 eV [17]), and C-O-C (533.1 eV [15]) were detected in large quantities. Furthermore, small signals corresponding to the C-O-H bond (534.5 eV [18]) were detected. Since no O atoms exist in a pure P(VDF-TeFE) film, all the detected bonds in this energy region should originate from impurities, which entered the film, and from solvents remaining in the films. Both R-C=O- and C=O bonds are components of MEK and DMAc and have spectra almost the same as C_{1s} core XPS spectra. Considering that the solvents are highly hygroscopic, it

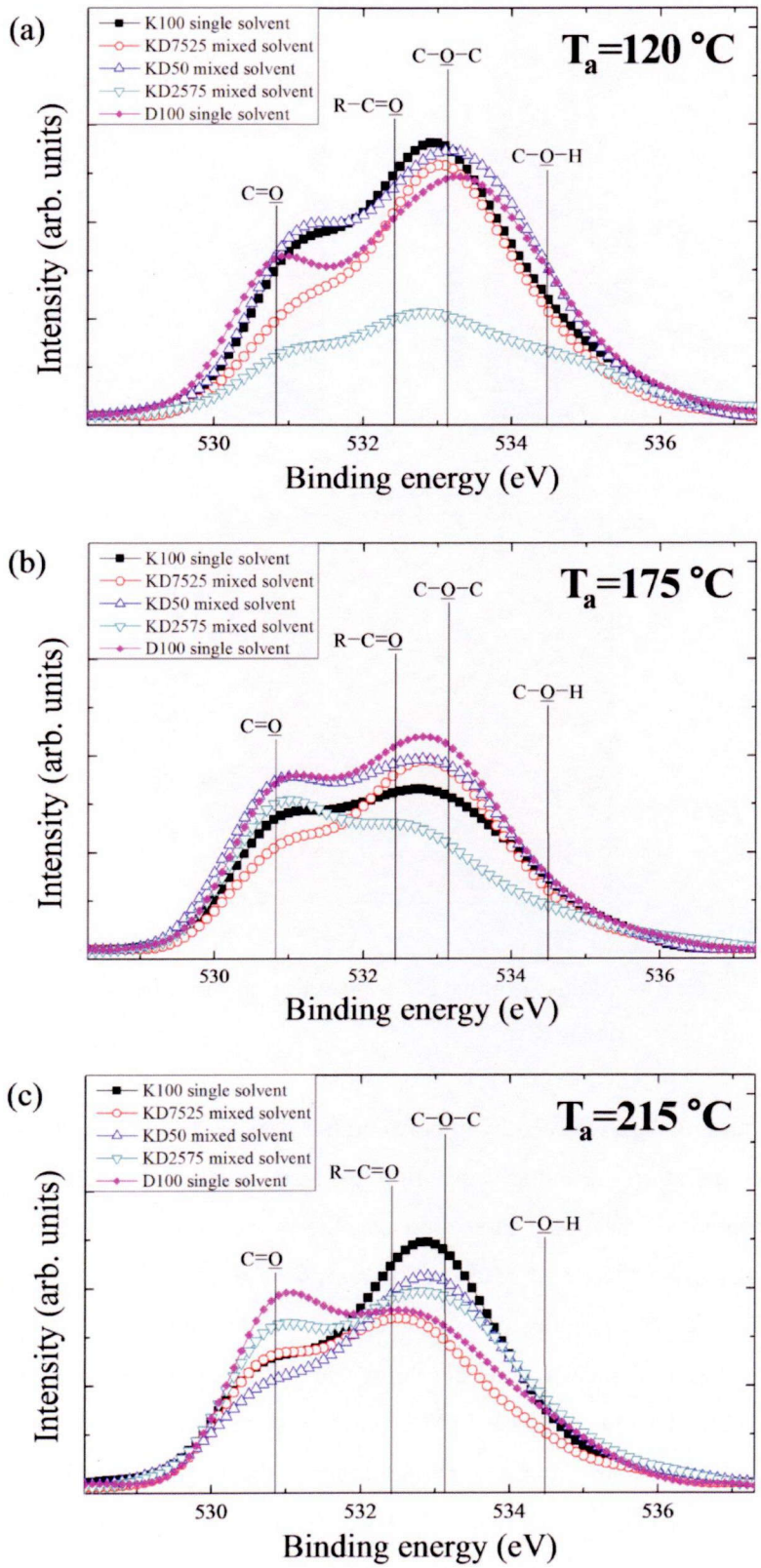

Fig. 2.12 O_{1s} core XPS spectra of the films formed with 10 wt% casting solution and subsequently annealed at (a) 120 °C, (b) 175 °C, and (c) 215 °C

appears that the C-O-H bond in the film is induced by humidity via the solvents. There was no relationship observed among the detected bonds, the mixing ratio, and the subsequent annealing temperature.

In order to confirm the existence of solvents remaining in the films, FTIR measurements were carried out. Typical results are shown in Fig. 2.13. Films that were formed using 10 wt% casting solutions and annealed at 175 °C were used, because the temperature of 175 °C is higher than the melting point of P(VDF-TeFE) (~ 170 °C) and the boiling point of DMAc (~ 165 °C). The $(C\text{-}C)_s$, $(CF_2)_b$, and $(CH_2)_b$ bonds indicated in Fig. 2.13 represent components of the chain structure of P(VDF-TeFE) [19] (see Appendix B). The subscripts s and b of each bond denote the stretching and bending of the covalent bonds in molecules, respectively. Even though the film formed with the KD7525 mixed solvent was the second thickest film among the films deposited with the five solvents, the IR absorption peaks corresponding to the bonds that were components of the chain structure of P(VDF-TeFE) were markedly higher in intensity than those for the other solvents. Considering the film thickness, the probability of the rearrangement of monomers was highest in the case of using the KD7525 mixed solvent.

As shown in Fig. 2.14, IR absorption due to both C=O stretching motion and C-H bending motion, which are related to the solvents, was detected for all the solvents studied [19], and absorption due to N-H bending motion was also detected for the solvents containing DMAc [20, 21], since MEK is a ketone compound (R-C=O-R') and DMAc is an amide compound (R-C=O-N-R'-R'') in carbonyl group (see Appendix C). Even though the annealing process was carried out at higher temperatures than both the melting point and boiling point, it is considered that the existence of solvents remaining in the films is a limitation of the present sol-gel process employed for the P(VDF-TeFE) film deposition. Since no O-H bonds were clearly detected, it was found that the moisture, which was detected by the XPS measurements, only affected the film surface. On the basis of both the XPS and FTIR spectra, it is concluded that the control of surface impurities and the removal of remaining solvents in the film are necessary for the formation of P(VDF-TeFE) films using the sol-gel process employed.

2.6 Relation between Film Formation Conditions and Piezoelectricity

In order to investigate the effect of the film formation conditions (solvent type and annealing temperature) on the piezoelectricity of P(VDF-TeFE) films, the remanent polarization, P_r, was measured. The results are shown in Fig. 2.15. All five casting solutions were used with a concentration of 10 wt%, and the annealing process was subsequently carried out at 120, 175, and

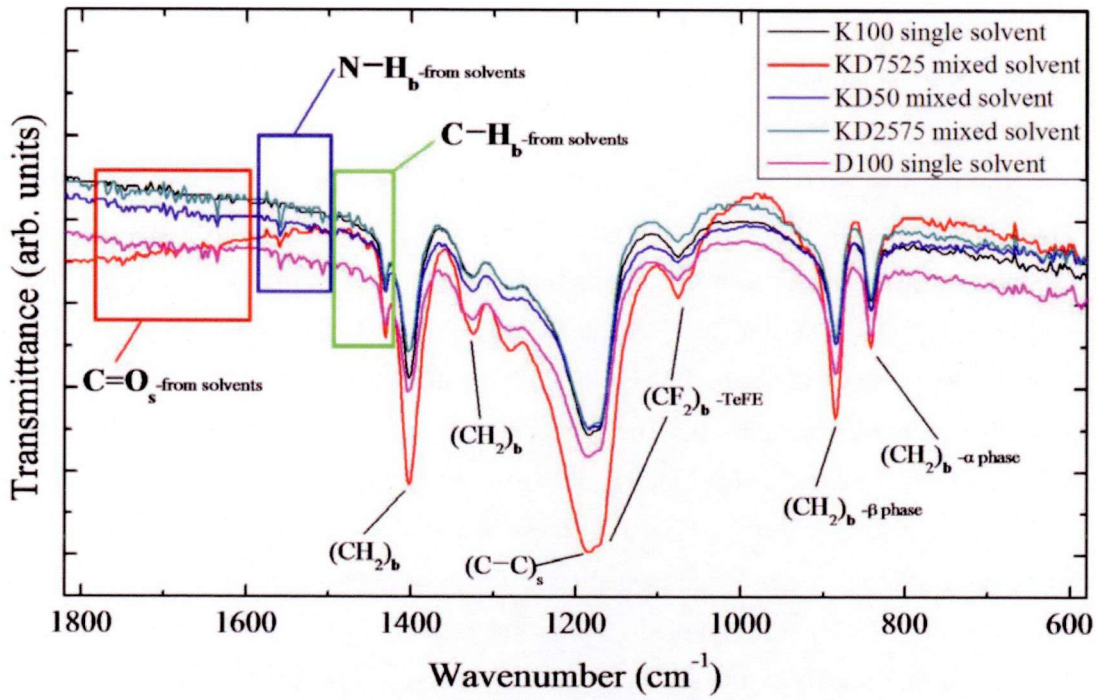

Fig. 2.13 FTIR spectra taken from the films formed with 10 wt% casting solution for all the 5-type solvents. The subscripts, **s** and **b**, represent stretching and bending motion, respectively.

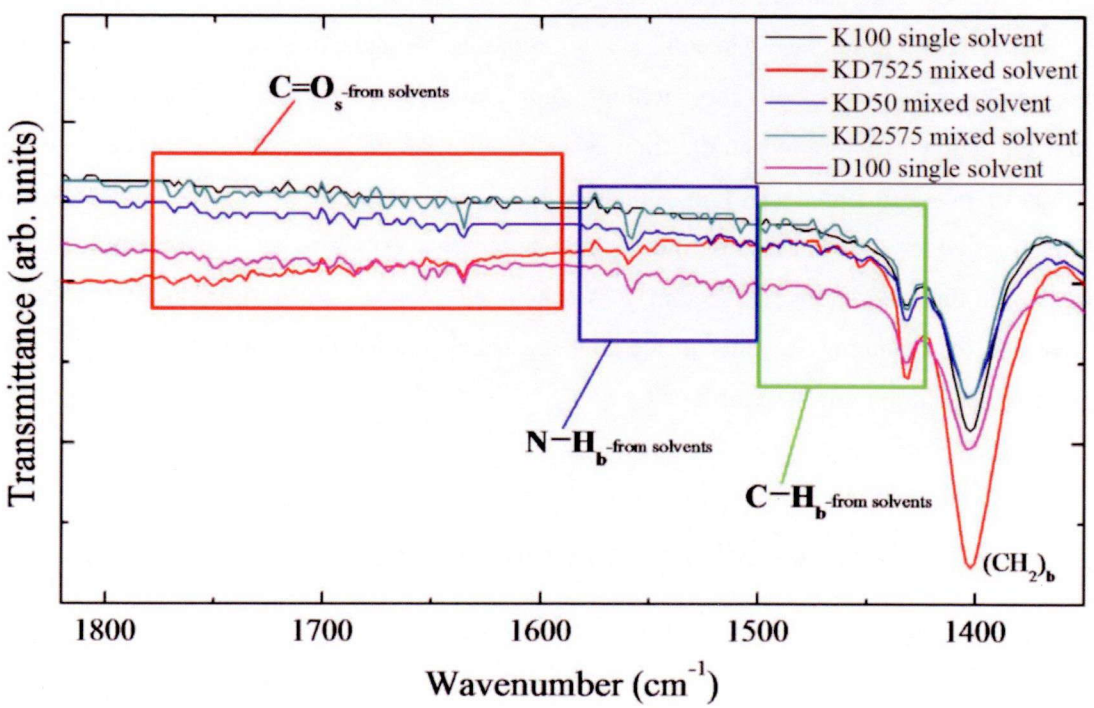

Fig. 2.14 FTIR spectra for the region in which IR absorption due to bonds related to remaining solvents is detected

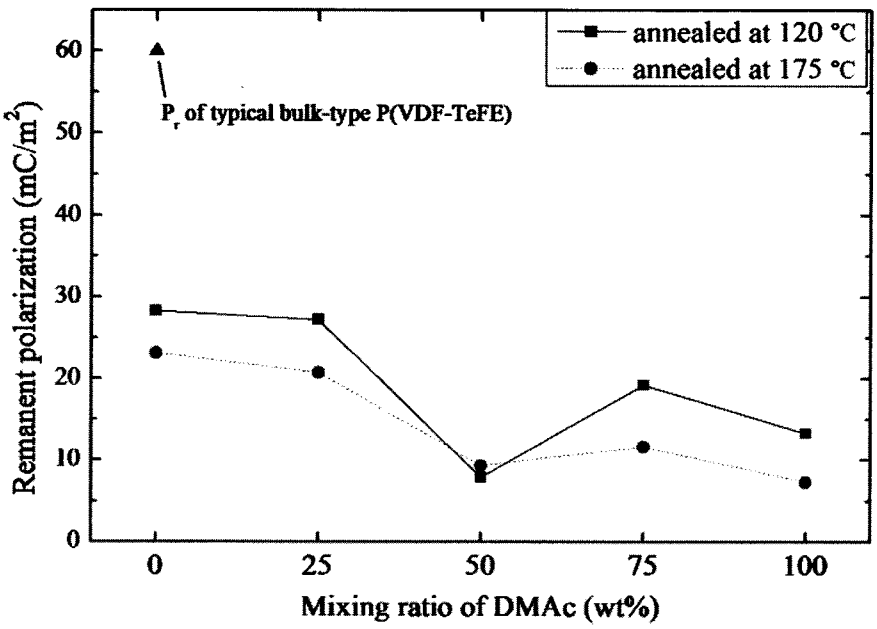

Fig. 2.15 Remanent polarizations obtained for cases with various mixing ratio of DMAc and post annealing temperatures

215 °C. After the annealing process, a Pt layer was deposited on the film surface by sputtering. The remanent polarization was measured using a ferroelectric test system (FCE-1, Toyo Corp., Japan). Since no remanent polarization was observed for the film annealed at 215 °C owing to the loss of piezoelectricity, the measured values for the films annealed at 120 and 175 °C are shown in Fig. 2.15.

The remanent polarization decreased with increasing the DMAc content, and it markedly decreased when the DMAc content increased from 25 to 50 wt%. According to the results for the film roughness described in section 2.3, the KD50 mixed solvent adversely affected the film formation and properties. In a previous study [8], the remanent polarization of a typical bulk-type P(VDF-TeFE) film (for which the thickness is 6~150 μm for commercially available films) was reported to be 60 mC/m^2. However, the remanent polarization measured for the films formed in this study was less than half of the value reported in the previous study. This difference is probably caused by the fact that the films formed in this section were not properly polarized. This means that P(VDF-TeFE) films cannot be well polarized only by the heat energy. In addition, the polarization decreased with increasing annealing temperature. Even though the PVDF copolymer film was annealed at a temperature higher than the Curie point, the polarization of the copolymer recovers to the average value after the annealing process [9]. However, according to the present experimental results, the measured remanent polarization decreased with increasing difference between the Curie point of P(VDF-TeFE) and annealing temperature.

2.7 Conclusion

In this chapter, the techniques used to form the P(VDF-TeFE) films based on the sol-gel process for fabrication of a diaphragm for an acoustic energy harvester have been described. The effect of five solvents and the subsequent annealing temperature were experimentally observed, in addition to the surface and bulk of the formed films. The obtained results are summarized as follows.

1. In the formation of the P(VDF-TeFE) films by the sol-gel process, controlling the concentration of the casting solution was more efficient than controlling the spin-coating speed. The probability of interfacial delamination between the film and substrate increased with increasing the spin-coating speed.

2. Even though a thin film was easily formed using a low-concentration casting solution, interfacial delamination occurred because the viscosity of the casting solution was also low. Hence, solvents in which MEK and DMAc are mixed can be used to control the viscosity of the casting solution.

3. The morphology of the formed films was stable at annealing temperatures of up to 175 °C, which is higher than the melting point of P(VDF-TeFE). However, the piezoelectricity of the film was decreased or lost when the annealing temperature was higher than the Curie point of P(VDF-TeFE).

4. As a result, to apply P(VDF-TeFE) thin films to a diaphragm, both possible impurities on the film surface and remaining solvents in the film have to be removed. Also, remedies are needed to employ the subsequent annealing process at temperatures higher than the Curie point of P(VDF-TeFE).

References

[1] S. Tasaka and S. Miyata, "Effects of crystal structure on piezoelectric and ferroelectric properties of copoly(vinylidenefluoridetetrafluoroethylene)," J. Appl. Phys. **57**, 906 (1985).

[2] K. Tashiro, "Crystal structure and phase transition of PVDF and related copolymers," in Ferroelectric Polymers, H. S. Nalwa, Marcel Dekker, New York (1995).

[3] F. J. Balta-Calleja, A. G. Arche, T. A. Ezquerra, C. Santa Cruz, F. Batallan, B. Frick, and E. Lopez Cabarcos, "Structure and Properties of Ferroelectric Copolymers of Poly(vinylidene) Fluoride," Adv. Polym. Sci. **108**, 1 (1993).

[4] H. Ohigashi, S. Akama, and K. Koga, "Lamellar and Bulk Single Crystals Grown in Annealed Films of Vinylidene Fluoride and Trifluoroethylene Copolymers," Jpn. J. Appl. Phys. **27**, 2144 (1988).

[5] V. Ranjan, L. Yu, S. Nakhmanson, J. Bernholc, and M. B. Nardelli, "Polarization effects and phase equilibria in high-energy-density polyvinylidene-fluoride-based polymers," Acta. Cryst. **66**, 553 (2010).

[6] K. M. Kim, N. G. Park, K. S. Ryu and S. H. Chang, "Physical and Electrochemical Characterizations of Poly(vinylidene fluoride-*co*-hexafluoropropylene)/SiO_2-Based Polymer Electrolytes Prepared by the Phase-Inversion Technique," J. Appl. Poly. Sci. **102**, 140 (2006).

[7] D. S. Viswanath, T. K. Ghosh, D. H. L. Prasad, N. V. K. Dutt, and K. Y. Rani, "Viscosity of Liquids," Springer 1 Ed., London (2006)

[8] J. X. Wen, "Piezoelectricity and Pyroelectricity in a Copolymer of Vinylidene Fluoride and Tetrafluoroethylene," Polymer J. **17**, 399 (1985).

[9] L. F. Brown and A. M. Fowler, "High vinylidene-fluoride content P(VDF-TrFE) films for ultrasound transducers," Ultrasonic Symposium Proceedings, 607 (1998).

[10] L.Zhao, I. Watanabe, T. Doi, S. Okada, and J. Yamaki, "TG-MS analysis of solid electrolyte interphase (SEI) on graphite negative-electrode in lithium-ion batteries," J. Power Sources **161**, 1275 (2006).

[11] Y. Ye, Y. D. Jiang, J. S. Yu, Z. M. Wu, and H. J. Zeng, "X-ray photoelectron spectroscopy characterization of the interface between Ag electrode and PVDF film treated by electric poling," J. Mater. Sci.: Mater. Electron. **17**, 1005 (2006).

[12] K. Müller, D. Mandal, K. Henkel, I. Paloumpa, and D, Schmeiβer, "Ferroelectric properties of spin-coated ultra-thin (down to 10 nm) P(VDF-TrFE) copolymer films," Appl. Phys. Letters **93**, 112901 (2008).

[13] Y. Jiang and W. C. Wang, "Functional membranes prepared by layer-by-layer assembly and its metal ions adsorption property," Polym. Adv. Technol., http://www.interscience.wiley.com, DOI: 10.1002/pat. 1793 (2010).

[14] D. Bar-Tow, E. Peled, and L. Burstein, "A Study of Highly Oriented Pyrolytic Graphite as a Model for the Graphite Anode in Li-Ion Batteries," J. Electrochem. Soc. **146**, 824 (1999).

[15] K. Kanamura, H. Tamura, S. Shiraishi, and Z. Takehara, "Morphology and chemical compositions of surface films of lithium deposited on a Ni substrate in nonaqueous electrolytes," J. Electroanal. Chem. **394**, 49 (1995).

[16] A. M. Andersson, A. Henningson, H. Siegbahn, U. Jansson, and K. Edström, "Electrochemically lithiated graphite characterized by photoelectron spectroscopy," J. Power Sources **522**, 119 (2003).

[17] V. Eshkenazi, E. Peled, L. Burstein, and D. Golodnitsky, "XPS analysis of the SEI formed on carbonaceous materials," Solid State Ion. **170**, 83 (2004).

[18] A. M. Andersson and K. Edström, "Chemical composition and morphology of the elevated temperature SEI on graphite," J. Electrochem. Soc. **148**, A1100 (2001).

[19] S. Lanceros-Méndiz, J. F. Mano, A. M. Costa, and V. H. Schmidt, "FTIR and DSC studies of mechanically deformed β-PVDF films," J. Macromol. Sci. –Physics **B40**, 517 (2001).

[20] M.-J. Brekner and C. Feger, "Curing studies of a polymer precursor," J. Polym. Sci. A Polym. Chem. **25**, 2005 (1987).

[21] M. Beer, H. B. Kessler, and G. B. B. M. Sutherland, "Spectra. Of Homologous Series of Monosubstituted Amides," J. Chem. Phys. **25**, 1097 (1958).

Chapter 3

Improvement on Properties of Poly(vinylidene fluoride - tetrafluoroethylene) Thin Films

3.1 Introduction

Using low-concentration casting solutions, the formation of P(VDF-TeFE) thin films with a suitable sol-gel process has been described in the previous chapter. Also, increasing the post-annealing temperature was suggested as a means of lowering the film roughness. Although a P(VDF-TeFE) thin film formed as above satisfies the mechanical properties required for a diaphragm, its properties as a piezoelectric thin film are unsatisfactory. The problems discussed in Chapter 2 are the reduction or loss of remanent polarization in the post-annealing process employed and the existence of solvents remaining in the film. Furthermore, pinholes appear when using a low-concentration casting solution [1]. The pinholes are molecular-structure defects of the PVDF copolymer, and the cause of their formation has not yet clarified. Such pinholes commonly appear in films formed by the sol-gel process, and cause the functions of such films as piezoelectric and ferroelectric films to be substantially lost depending on the depth of the pinholes. Upon solving the problems noted above, a P(VDF-TeFE) thin film can be formed as a piezoelectric diaphragm.

In order to remove the solvents remaining in the films, a low-pressure chamber is employed in this study. Because it is difficult to use a low-pressure chamber in the spin-coating process, the annealing process in a low-pressure chamber is suggested as a means of effectively removing the remaining solvents in the film. If the spin-coating process is carried out in a low-pressure chamber, the film morphology tends to become rough owing to the substantial rate of evaporation of the solvents, even though a post-annealing process is carried out after the spin-coating process. In the annealing process, since the annealing temperature is higher than the boiling point of the solvents and the melting point of P(VDF-TeFE), the evaporation of both MEK and DMAc and their separation from the liquefied P(VDF-TeFE) film are facilitated. However, the direction of dipole moments should be fixed by an electric field because the remanent polarization decreased at high annealing temperatures as mentioned in the previous chapter [2]. Hence, it is difficult to employ a

high-vacuum chamber for the annealing process because of the difficulty in applying a sufficient electric field, whose intensity is often limited in a high-vacuum chamber. The formation of pinholes can be suppressed by optimizing the post-annealing temperature and the process time, because it is difficult to completely prevent the formation of pinholes.

In this chapter, the remedies by which the problems in the film formation process are solved are proposed, and their effectiveness is experimentally verified.

3.2 Experimental Procedures

3.2.1 Preparation of Samples and Solvents

Among the five single and mixed solvents referred to Chapter 2, the solvents with which thin films with a thickness of 1 μm can be formed are the K100 single solvent (MEK 100 wt%) and KD7525 mixed solvent (MEK 75 wt% + DMAc 25 wt%). Even though a film thinner than 1 μm can be formed using the KD7525 mixed solvent, both the K100 single solvent and KD7525 mixed solvent are employed in this study to investigate the difference between a single solvent and a mixed solvent because a single solvent is commonly applied to form such films [3]. For each solvent, 4 wt% casting solution of P(VDF-TeFE) was made up to form a thin film by the spin-coating process, which was carried out using an initial speed of 1,000 rpm (for 15 seconds) and a

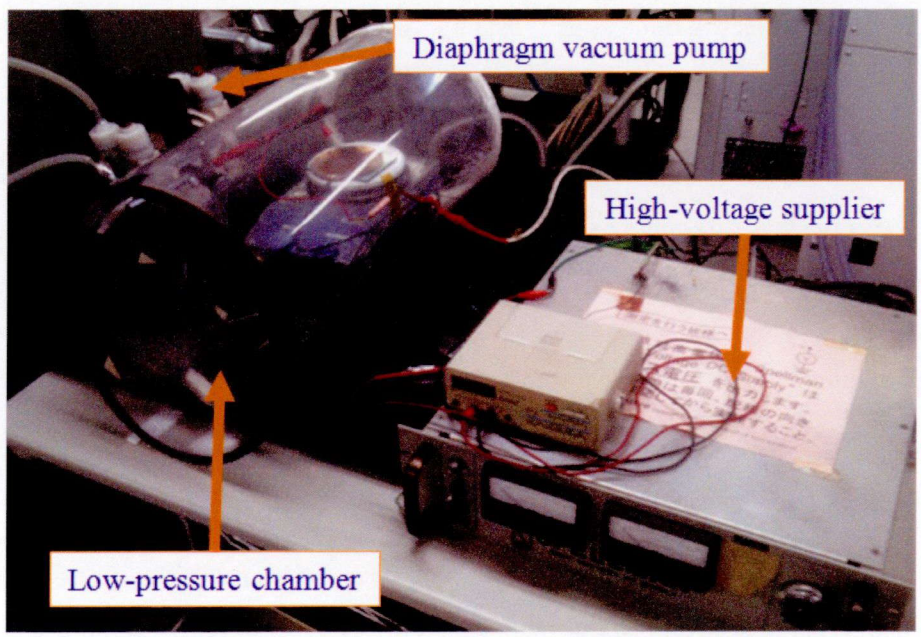

Fig. 3.1 A low-pressure chamber employed for the annealing process under an applied electric field

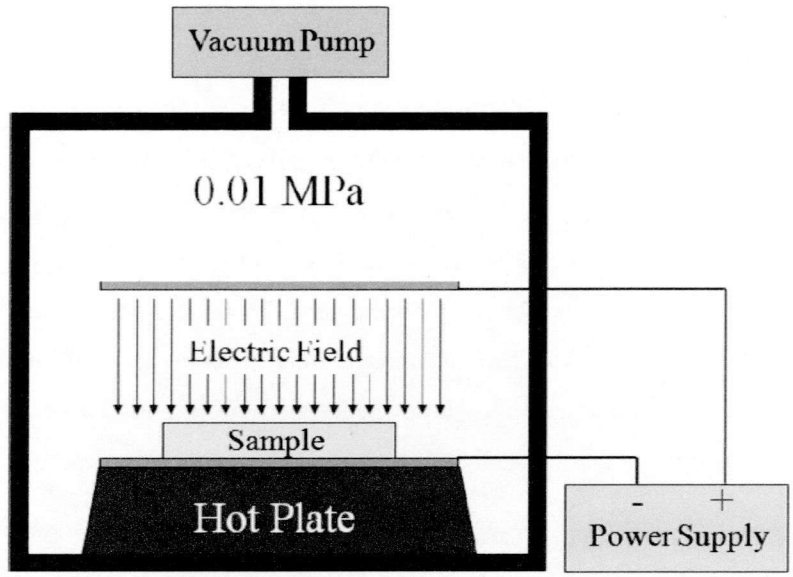

Fig. 3.2 A schematic diagram for the application of an electric field during an annealing process

terminal speed of 5,000 rpm (for 45 seconds). In order to reduce the effect of humidity and dust, the spin-coating process was carried out in an airtight container in which the temperature and humidity were controlled. Also, to prevent impurities from contaminating the film during the spin-coating process, the chamber of the spin-coater was filled with N_2 gas.

3.2.2 Application of Electric Field during Annealing Process

After the spin-coating process, the post-annealing process was carried out in a low-pressure chamber, as shown in Fig. 3.1. In order to reduce the surface roughness of the film, the post-annealing process should be carried out at a temperature higher than the melting point of P(VDF-TeFE) [4]. Also, to remove remaining solvents in the film, the P(VDF-TeFE) film should be liquefied during the post annealing process in the low-pressure chamber. Hence, the post-annealing process proposed in this study was carried out at 195 °C. In order to preserve the remanent polarization of P(VDF-TeFE), an electric field was applied to the sample during the annealing process, as schematically shown in Fig. 3.2. Although the maximum applicable electric field was 2.2 MV/m at the low-pressure of 0.01 MPa, an electric field of 1 MV/m was applied considering the leakage current between electrodes.

3.3 Surface Morphology

In order to investigate the effects of the low-pressure annealing process on the formation of pinholes, the surface of a film formed with the KD7525 mixed solvent was observed with a SEM and an AFM. Fig. 3.3 (a) shows the surface of a film after annealing at atmospheric pressure, while Fig. 3.3 (b) shows the surface of a film annealed in the low-pressure chamber. For the film shown in Fig. 3.3 (a), many pinholes were observed on the sample surface, and the pinhole density was about 6.3 x 10^8 cm^{-2}. Although it was difficult to accurately measure the depth of each pinhole, the average depth was over 100 nm. Several pinholes penetrated into the P(VDF-TeFE) thin film from the film surface to reach the substrate surface [5]. On the film surface annealed in the low-pressure

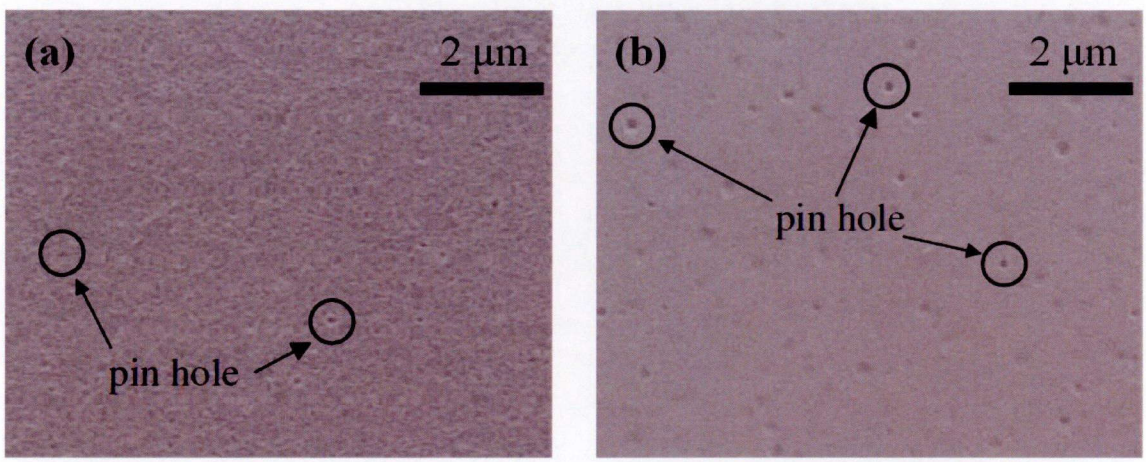

Fig. 3.3 Typical SEM images of the film surface annealed in (a) atmosphere without a chamber and in (b) a low-pressure chamber

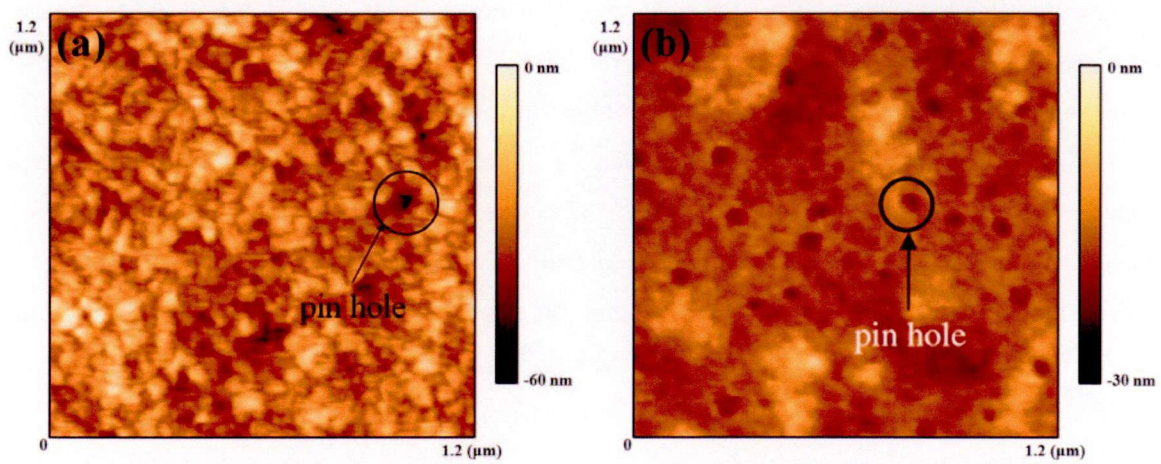

Fig. 3.4 Typical AFM images of the film surface annealed in (a) atmosphere without a chamber and in (b) a low-pressure chamber

chamber, as shown in Fig. 3.3 (b), the pinhole density was about 1.6 x 10^8 cm^{-2}, and a decrease of about 75% compared with that of the film formed by the conventional annealing process. Even though the diameter of each pinhole was larger for the film formed under a low pressure, the pinholes were shallow; if pinholes penetrate deep into a P(VDF-TeFE) thin film, then it cannot be used as a piezoelectric film anymore. As shown in AFM images in Fig. 3.4, the pinholes on the surface of the film annealed using the conventional method were very deep although their diameters were small. In contrast, the pinholes on the surface of the film annealed in the low-pressure chamber were shallow but with large diameters. As a result, the formation of such deep pinholes penetrating into the P(VDF-TeFE) thin film was suppressed by employing the low-pressure annealing process.

3.4 Problem of Remaining Solvents

In the annealing process discussed in the previous chapter, impurities such as remaining solvents and dust were often detected on the film surface. Since such film surfaces become the interfaces upon the deposition of a top electrode, careful treatment of the film surface is important to maintain its electrical properties. From the spin-coating process to the end of the annealing process, contamination by impurities was prevented as far as possible by controlling the temperature and humidity in a sealed chamber. Both XPS and FTIR spectra were measured for such specimens, which were compared with those of specimens formed using the conventional annealing process without a low-pressure chamber (see Appendix A and B). The K100 single solvent and KD7525 mixed solvent were used to make up 4 wt% casting solutions. The two solvents were used to form a 500-nm-thick a P(VDF-TeFE) thin film, which was applied to fabricate a diaphragm.

When an electric field was applied during the annealing process, the sample surface became electrostatically charged as shown in Fig. 3.5. In the case of using the conventional annealing process without a low-pressure chamber, the sample surface became slightly charged, and the XPS spectra were shifted to a slightly higher binding energy. However, in the case of using the low-pressure annealing process with an applied electric field, the sample surface became more highly charged than in case of the conventional annealing process. Hence, all the spectra of C_{1s} and O_{1s} in Figs. 3.6 and 3.7, respectively, were adjusted by the difference between the measured F_{1s} peak and the reference peak for the F_{1s} core electrons, whose binding energy is at 689.3 eV for CF_2 bonds with the VDF structure [6].

Figures 3.6 and 3.7 respectively show XPS spectra of C_{1s} core electrons and O_{1s} core electrons

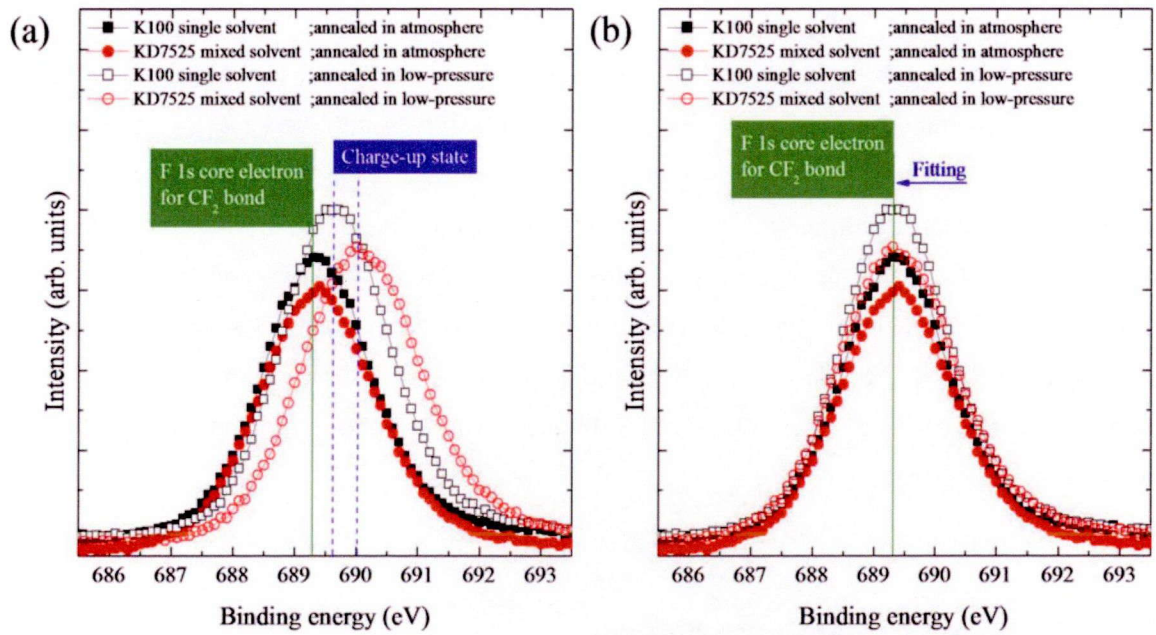

Fig. 3.5 XPS spectra of F_{1s} core electrons taken from the films annealed in atmosphere and in the low-pressure chamber. (a) Original spectra measured and (b) fitted spectra for F 1s core electron of CF_2 bond

for the films formed using the K100 single solvent and KD7525 mixed solvent. In Fig. 3.6, the difference in spectral intensity between the carbon atoms contained in the -CF_2-$\underline{C}H_2$-CF_2- (286.3 eV) and -CH_2-$\underline{C}F_2$-CH_2- (290.8 eV) structures indicates the difference in the density of VDF bonds per unit surface. In the films annealed by using the conventional process, as shown in Fig. 3.6 (a), the R-$\underline{C}$=O- structure (282.5 eV [7]) was commonly detected. The structure is related to a ketone and amide of carbonyl group in the signals of a MEK and a DMAc, respectively, indicating the existence of solvents remaining in the film. By contrast, in the films annealed in the low-pressure chamber under an applied electric field as shown in Fig. 3.6 (b), R-$\underline{C}$=O- was not detected. This indicates that the remaining solvents were removed from the film surface. In the film formed using the K100 single solvent, the $\underline{C}$-H bond (283.5 eV [8]) was detected. This peak, as mentioned in the previous chapter, was observed in the amorphous P(VDF-TeFE) film of the remaining solvents [9]. During the annealing process at temperatures higher than the melting point of P(VDF-TeFE), monomers of P(VDF-TeFE), which are spread out in the film and have a chain structure, lose their preferential orientation. However, the monomers are rearranged by the electric field during the annealing process. With the decreasing substrate temperature after the annealing process, the monomers set in a chain structure with the preferential orientation preserved. Hence, $\underline{C}$-H bonds did not disappear as a result of the low-pressure annealing process but by the rearrangement of the amorphous P(VDF-TeFE) film induced by the electric field applied during the annealing process.

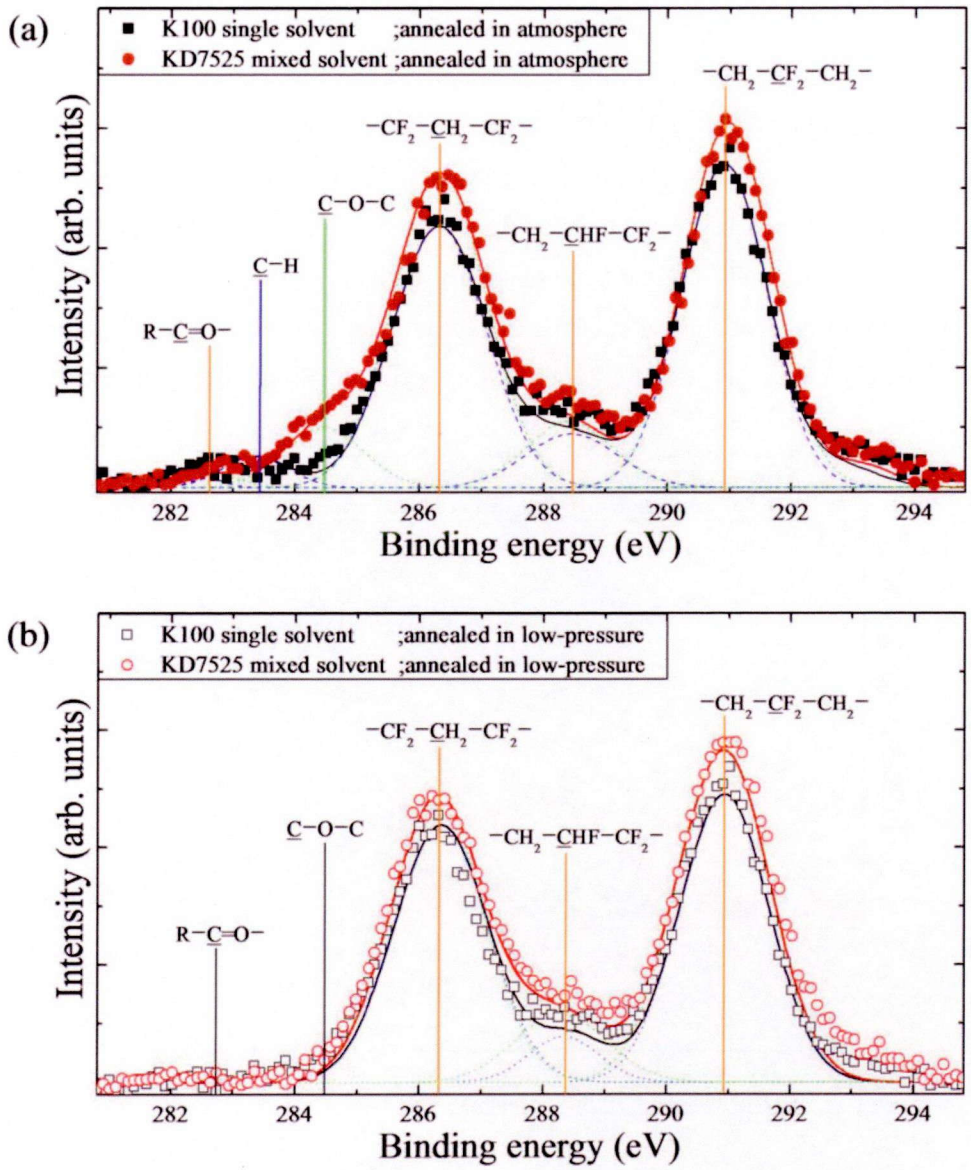

Fig. 3.6 XPS spectra of C_{1s} core electron of the film annealed in (a) atmosphere, and in (b) the low-pressure chamber

C-O-C (284.5 eV [10]) bonds can be formed by the inclusion of an O atom during the recombination of broken chains of P(VDF-TeFE). C-O-C peaks were not detected owing to the removal of the remaining solvents through the low-pressure annealing process. Meanwhile, the peak of the -CH_2-CHF-CF_2- of the TrFE (trifluoroethylene) structure was detected at 288.5 eV [11]. The full width at half maximum (FWHM) of the peak of the TrFE structure is almost the same as that of the VDF structure, although the peaks have a lower intensity than those of the VDF structure. The TrFE structure was detected in wide range owing to its weak binding in the P(VDF-TeFE) film. For this reason, TrFE structures probably exist in the amorphous P(VDF-TeFE) film.

Because of the detection of C atoms bonded to O atoms, O_{1s} core electron (533 eV [12]) XPS spectra were also measured as shown in Fig. 3.7. Among the film annealed with the conventional process as shown in Fig. 3.7 (a), the XPS spectra display a marked distinction between the films formed using the K100 single solvent and using the KD7525 mixed solvent. In the case of the film formed using the K100 single solvent, signals from both the R-C=O- (532.4 eV [13]) bond and the C-O-C (533.1 eV [10]) bond were the main structures in the XPS spectra. On the other hand, in the case of the film formed using the KD7525 mixed solvent, appeared signals corresponding to trapped O ions (529.8 eV [14]) and C=O (530.8 eV [9]) bonds appeared. The existence of these

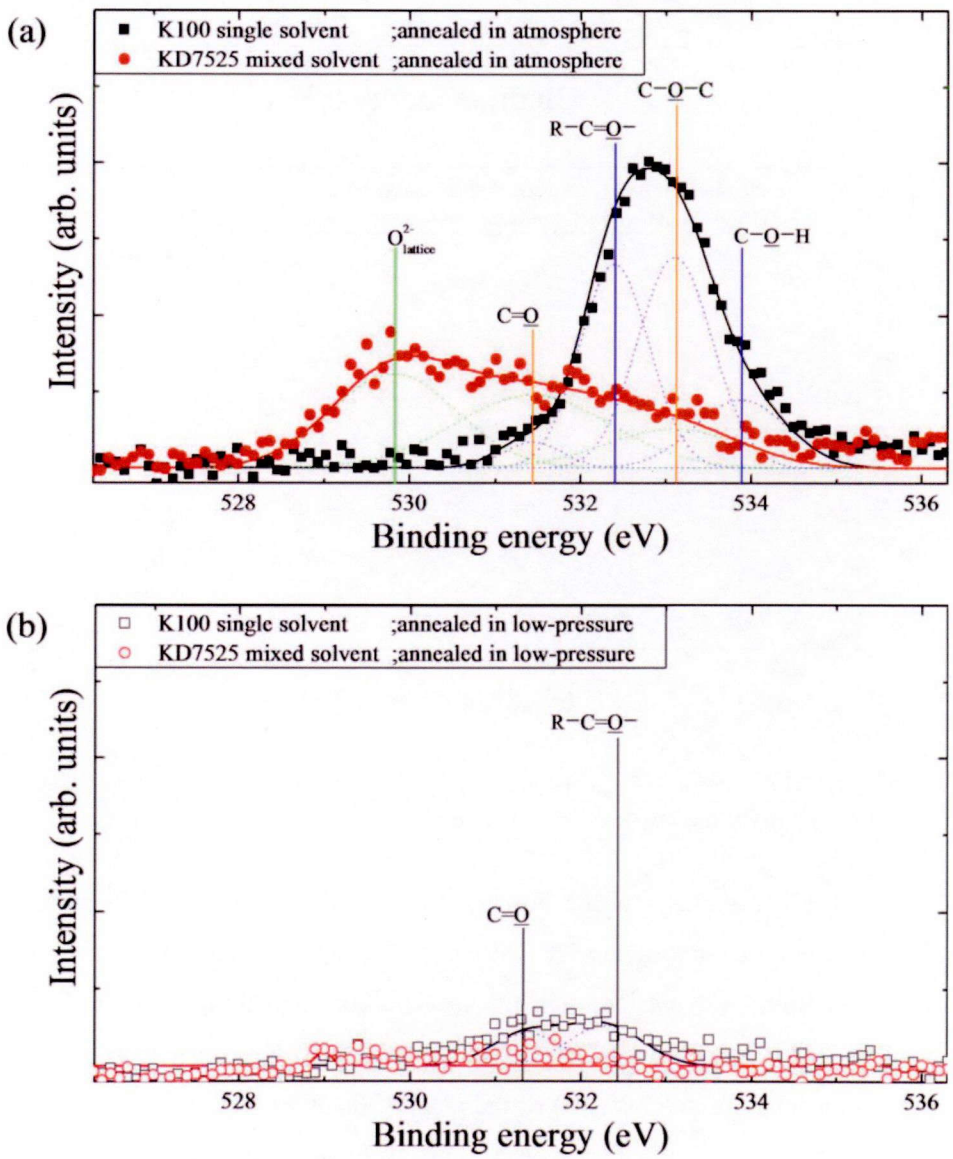

Fig. 3.7 XPS spectra of O_{1s} core electron taken from the film annealed in (a) atmosphere, and in (b) the low-pressure chamber

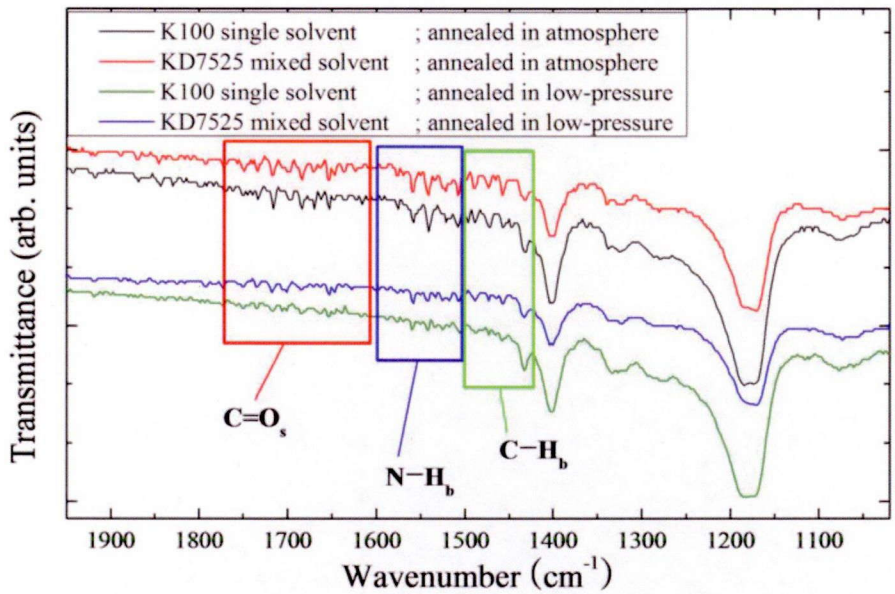

Fig. 3.8 FTIR spectra of the film annealed in atmosphere and in the low-pressure chamber for two solvents, the K100 single solvent and the KD7525 mixed solvent

bonds indicated a difference in the rearrangement process of the P(VDF-TeFE) chain structure that depends on the solvent type. For the film annealed in the low-pressure chamber with the application of an electric field as shown in Fig. 3.7 (b), most of the peaks related to O bonds were not detected. Only for the case of using the K100 single solvent were a few peaks related to the remaining solvents detected.

In order to investigate the internal state of the P(VDF-TeFE) thin films, FTIR measurements were carried out. Typical absorption spectra obtained are shown in Fig. 3.8. As discussed in the previous chapter, absorption due to the excitation of C=O stretching motion and C-H bending motion, respectively, related to the ketone structure (R-C=O-R') in MEK and the amide structure (R-C=O-N-R'-R'') in DMAc, were detected for all the samples measured. Such absorption can also be detected from the solvents employed. Compared with the film annealed by the conventional process, the absorption due to C=O stretching motion and C-H bending motion was markedly lower in the film annealed in the low-pressure chamber with the application of an electric field. The observed decrease in absorption indicates that most of the remaining solvents was removed from the film. As a result, the low-pressure annealing process with an electric field contributed to removing impurities from the bulk and surface of the film. Although the remaining solvents can be almost entirely removed by sufficiently lowering the pressure, it becomes difficult to apply an electric field during the annealing process because dielectric breakdown easily occurs between the two electrodes used to apply an electric field.

3.5 Recovery of Remanent Polarization

As discussed in Chapter 2, increasing the annealing temperature efficiently reduced the roughness of the surface of the P(VDF-TeFE) film. The annealing process was carried out at 195 °C in this study, which is higher than the melting point of P(VDF-TeFE). Hence, the P(VDF-TeFE) film easily lost its piezoelectricity after the annealing process. As reported in this chapter, an electric field was applied during the annealing process to preserve the orientation of the dipole

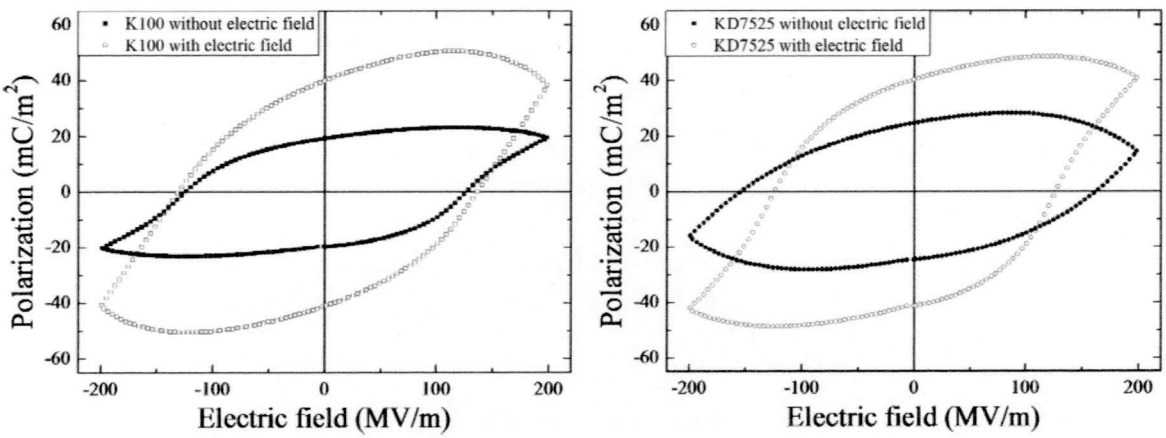

Fig. 3.9 The polarization of the P(VDF-TeFE) film annealed with and without an applied electric field for two solvents, the K100 single solvent (left side) and the KD7525 mixed solvent (right side)

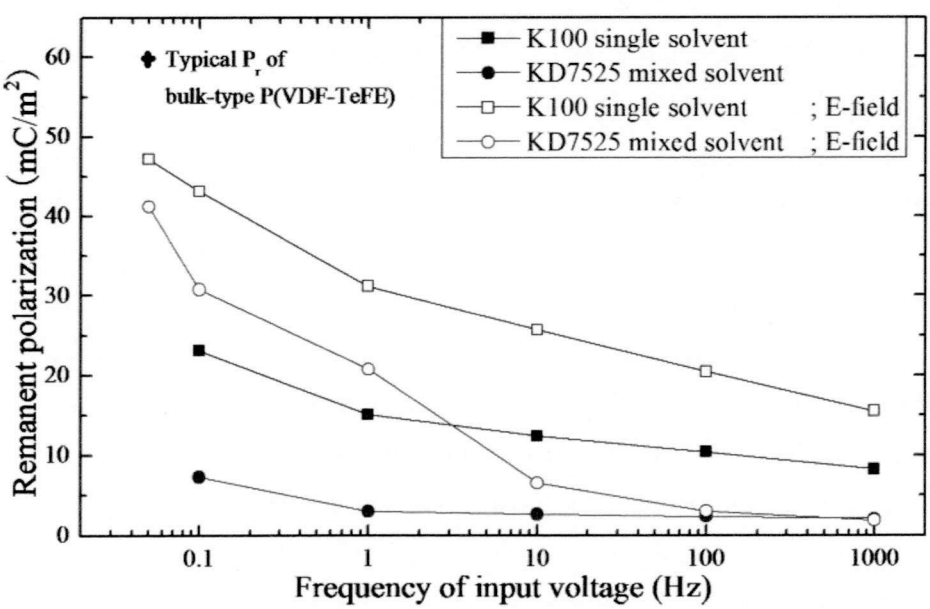

Fig. 3.10 The polarization of the films formed with different solvents with and without an applied electric field as a function of the frequency of the input voltage

moments. In order to measure the remanent polarization, a 60-nm-thick Pt film was sputter-deposited on the surfaces of films that had been annealed at atmospheric pressure and in the low-pressure chamber. Fig. 3.9 shows typical P-E hysteresis loops obtained. The measured remanent polarization markedly differed with the annealing conditions. For the film annealed at atmospheric pressure, the measured polarization was relatively small. This reduction in the polarization may originate from the remaining solvents in the film and impurities on the film surface. Compared with the film annealed at atmospheric pressure without an electric field, the measured polarization of the film annealed in the low-pressure chamber with the application of an electric field was relatively high, probably due to the removal of the remaining solvents and impurities.

Considering the XPS results, it is anticipated that a relationship may exist between the frequency of the input voltage used for measurement and the remanent polarization of the films formed using the single solvent and mixed solvent. Fig. 3.10 shows changes in the remanent polarization as a function of the frequency of the input voltage for frequencies ranging from 0.05 to 1,000 Hz. Since the rate of change of dipole moments is low in a piezoelectric polymer compared with in metallic piezoelectric materials [15], the remanent polarization of the piezoelectric polymer decreased with increasing frequency of the input voltage. In a previous study [3], the polarization was reported to be 60 mC/m^2 for a bulk-type P(VDF-TeFE) film. As a result, compared with the annealing process at atmospheric pressure, it is found that the low-pressure annealing process with the application of an electric field was more effective in preserving the polarization and reducing the surface roughness of the film.

3.6 Conclusion

In order to supplement and improve the weak points of employing the general sol-gel process, the annealing process in a low-pressure chamber while applying an electric field has been proposed in this chapter. By considering the surface morphology, the existence of impurities, and the remanent polarization, the suitability of the proposed annealing process was compared with that of the previously employed conventional annealing process. The results obtained in this chapter are summarized as follows.

1. Although the formation of pinholes cannot be completely suppressed by using the low-pressure annealing process, it changed the morphology of the pinholes, by increasing their diameter and reducing their depth. These changes led to improved electric properties of the P(VDF-TeFE) thin film.

2. According to the XPS and FTIR spectra, the amounts of impurities and amorphous P(VDF-TeFE) in the film were decreased by the low-pressure annealing process by preventing contamination with impurities and removing solvents remaining from the spin-coating process.

3. In order to reduce the roughness of the film surface, the annealing temperature should be higher than the melting point of a P(VDF-TeFE). Although the remanent polarization is at risk of being reduced or lost at high temperatures, the remanent polarization was preserved by applying an electric field during the annealing process.

4. As a result, the problems associated with the formation of a P(VDF-TeFE) thin film by using the sol-gel process and thermal treatment can be solved by applying the proposed annealing process.

References

[1] J. D. Foster and R. M. White, "Electrophoretic Deposition of The Piezoelectric Polymer P(VDF-TrFE)," Proc. of. 201st Meeting of The Electrochemical Society, Philadelphia (2002).

[2] T. Furukawa, M. Date, E. Fukada, Y. Tajitsu, and A. Chiba, "Ferroelectric Behavior in the Copolymer of vinylidenefluoride and Trifluoroethylene," Jpn. J. Appl. Phys. **19**, L109 (1980).

[3] J. X. Wen, "Piezoelectricity and Pyroelectricity in a Copolymer of Vinylidene Fluoride and Tetrafluoroethylene," Polymer J. **17**, 399 (1985).

[4] M. Neidhöfer, F. Beaume, L. Ibos, A. Bernès, and C. Lacabanne, "Structural evolution of PVDF during storage or annealing," Polymer **4**, 1679 (2004).

[5] H. Taunaumang and I. L. Guy, "Electromechanical properties of 1-3 piezoelectric ceramic/piezoelectric polymer composites," J. Appl. Phys. **76**, 484 (1994).

[6] D. T. Clark, W. J. Feast, D. Kilcast, and W. K. R. Musgrave, "Applications of ESCA to Polymer Chemistry. III. Structures and Bonding in Homopolymers of Ethylene and the Fluoroethylenes and Determination of the Compositions of Fluoro Copolymers," J. Polym. Sci., Polym. Chem. Ed. **11**, 389 (1973).

[7] Y. Jiang and W. C. Wang, "Functional membranes prepared by layer-by-layer assembly and its metal ions adsorption property," Polym. Adv. Technol., http://www.interscience.wiley.com, DOI: 10.1002/pat. 1793 (2010).

[8] D. Bar-Tow, E. Peled, and L. Burstein, "A Study of Highly Oriented Pyrolytic Graphite as a Model for the Graphite Anode in Li-Ion Batteries," J. Electrochem. Soc. **146**, 824 (1999).

[9] C. Y. Chiang, Y. J. Shen, M. J. Reddy, and P. P. Chu, "Complexation of poly(vinylidene fluoride): $LiPF_6$ solid polymer electrolyte with enhanced ion conduction in 'wet' form," J. Power Sources **123**, 222 (2003).

[10] K. Kanamura, H. Tamura, S. Shiraishi, and Z. Takehara, "Morphology and chemical compositions of surface films of lithium deposited on a Ni substrate in nonaqueous electrolytes," J. Electroanal. Chem. **394**, 49 (1995).

[11] L. F. Brown and A. M. Fowler, "High vinylidene-fluoride content P(VDF-TrFE) films for ultrasound transducers," Ultrasonic Symposium Proceedings, 607 (1998).

[12] A. M. Andersson, A. Henningson, H. Siegbahn, U. Jansson, and K. Edström, "Electrochemically lithiated graphite characterized by photoelectron spectroscopy," J. Power Sources **522**, 119 (2003).

[13] V. Eshkenazi, E. Peled, L. Burstein, and D. Golodnitsky, "XPS analysis of the SEI formed on carbonaceous materials," Solid State Ion. **170**, 83 (2004).

[14] J. S. Corneille, J. W. He, and D. W. Goodman, "Preparation and characterization of ultra-thin iron oxide films on a Mo(100) surface," Surface Science **338**, 211 (1995).

[15] T. Furukawa, M. Date, and E. Fukada, "Hysteresis phenomena in polyvinylidene fluoride under high electric field," J. Appl. Phys. **51**, 1135 (1980).

Chapter 4

Design, Fabrication, and Characterization of the Acoustic Energy Harvester for the Fundamental Frequency of Human Voice

4.1 Introduction

In a previous study [1], an acoustic energy harvester has been demonstrated that employed a mesoscale Helmholtz resonator fabricated with aluminum (dimensions: 24.8 mm in diameter and 16.1 mm in length with a circular piezoelectric patch of 20.2 mm in diameter), delivering a power of 25 mW to a resistive load at 152 dB SPL. This acoustic energy, which may originate from sound, noise, or a voice, may be used to locally power a wireless active liner for the suppression of engine noise in turbofan engine nacelles, where noise levels typically reach upwards of 150 dB SPL [2]. Note that there is a substantial amount of data on the fundamental frequency of human voices (F_0) in the speech of speakers of different ages and genders. Such data have been published in several languages and for various types of discourse. The data reported nearly always include an average value of F_0, usually expressed in Hz, but in some cases the average duration of a period has been reported instead. Typical values obtained for F_0 are 120 Hz for men and 210 Hz for women [3]. Since the acoustic pressure of a human voice is under 90 dB sound pressure level (SPL) (0.632 Pa at a reference pressure of 20 μPa) from a distance of 5 cm, the human voice has very low energy as an ambient source.

Since the acoustic pressure of a human voice is very low, it is difficult to transmit it to a diaphragm for application in a Helmholtz resonator. Hence, the use of a diaphragm without a bottleneck in a Helmholtz resonator is suggested in this study. Because of the use of an exposed diaphragm, the area that can be reached by acoustic waves is increased and the sensitivity to the frequency is improved. The energy of an acoustic wave reaching the diaphragm of the energy harvester is irregular and very small because the voice is transmitted via air. Therefore, it is necessary to reduce the mechanical impedance and resonant frequency in the design of the energy harvester. In this study, an acoustic energy harvester whose resonant frequency corresponds to the

fundamental frequency of a human voice is theoretically designed, fabricated, and characterized experimentally. On the frequency and acoustic pressure level of a sound source, the output voltage is measured and characterized for a waveform that represents the state of the diaphragm resonating at a specific resonant frequency.

4.2 Design of Energy Harvester

Microscale diaphragm structures play a significant role in microtransducers and micro-nano devices as they can be used as elastic sensing elements for capacitive-type pressure, acceleration, sound and ultrasound, chemical, and biological microtransducers. The microscale diaphragms of these devices are fabricated by using either a surface micromachining sacrificial layer process or bulk micromachining with bonding technology. Circular diaphragms are commonly used, which are fixed on a silicon substrate through a side wall such that there is a thin air gap between the diaphragm and substrate. The air gap is either filled with air or vacuum-sealed. The diaphragm and substrate are both coated by a metal electrode, so that the structure becomes a capacitive-type microtransducer. Since there is a microscale separation, a moderate voltage applied across these two electrodes can produce a large electrostatic force.

Taking acoustic transducer as an example, if the diaphragm is excited by external sound waves, its vibration will result in a change in the capacitance and output voltage of the transducer, which can be exploited to detect acoustic waves, so that the diaphragm acts as a sonic or ultrasonic receiver. In contrast, if the diaphragm is excited by an electrostatic force produced by signal voltage across the two electrodes, its vibration will drive the surrounding medium, which can be utilized to transmit sound waves, so that the diaphragm acts as a sonic or ultrasonic generator. Therefore, microscale diaphragms are key elements in the transduction from the mechanical (or acoustical) to electrical energy domain or from the electrical to mechanical (or acoustical) energy domain. Therefore, it is of fundamental importance to study the dynamic behavior of microscale diaphragms acting as key elements.

Rayleigh gave a fundamental discussion on the vibration of membranes and plates in his book "The Theory of Sound" [4]. Afterward, Wente applied the second-order partial differential equation of membrane vibration developed by Rayleigh to describe the behavior of the diaphragm in the condenser microphones he invented [5]. Henceforth, the membrane model has been widely used to model various condenser microphones. Note that Mason applied the fourth-order partial differential equation of plate vibration developed by Rayleigh to describe the behavior of the diaphragms of telephone receivers, and further studied the issue of stretched plate vibration, where

both the bending stiffness of the diaphragm and the tension were taken into account, from which he developed a mathematical description [6]. He also indicated that if the stiffness of the plate is small compared with the tension, the problem is reduced to membrane vibration, whereas if the tension is small, it is reduced to plate vibration. Because of the use of a micromachining process, the silicon nitride films in a capacitive micromachined ultrasonic transducers (CMUTs) have large residual stress, which provides a uniform radial in-plane force; thus, the classical membrane model was used to describe the behavior of such diaphragms [7], and the stretched plate model developed by Mason was also used to describe their behavior [8]. In order to facilitate the design of systems powered by an acoustic energy harvester, the goal of the following theoretical analysis is to arrive at an equivalent circuit model of an energy harvester.

4.2.1 Resonant Frequency of Diaphragm

Vibration of a rigid body can be caused by several factors such as unbalanced mass in a system, tear and wear of materials and can occur in almost all dynamical systems. The characteristic behavior is unique to each system and can be simply described by two parameters: damping constant and natural frequency. Most commonly, a single degree of freedom lumped spring mass system is utilized to study the dynamic characteristics of a vibrating body associated with energy harvesting. The single degree of freedom helps to study unidirectional response of the system.

Fig. 4.1 shows a diagram of a diaphragm with P(VDF-TeFE) layer on a Si substrate; and equivalent lumped spring mass with external excitation. The source of vibration is shown with a red arrow at the base of the contact point (red dot). The stiffness of the structure depends on the

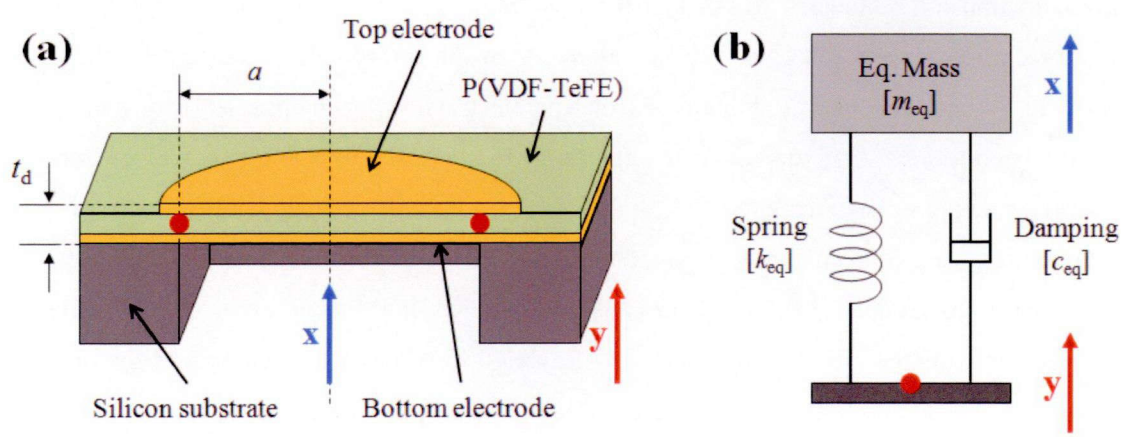

Fig. 4.1 A schematic diagram of (a) the diaphragm on Si substrate, and (b) the equivalent lumped mass-spring-damper system of a vibrating rigid body

loading condition, material, and cross-sectional area perpendicular to the direction of vibration. The governing equation of motion for the system Fig. 4.1 (b) can be obtained from energy balance equation or D'Alembert's principle [9]. The governing equation of motion for a lumped spring mass system can be written as:

$$m_{eq}\ddot{z} + c_{eq}\dot{z} + k_{eq}z = -m_{eq}\ddot{y} \ , \tag{4.1}$$

where m_{eq} is the equivalent mass, c_{eq} is the equivalent damping ratio, and k_{eq} is the equivalent stiffness of the diaphragm. $z = x - y$ is the net displacement of the diaphragm where x and y is the displacement of the diaphragm and substrate respectively. Eq. (4.1) can also be written in terms of damping constant and natural frequency. A damping factor, ζ, is a dimensionless number defined as the ratio of the system damping c_{eq} to critical damping c_c as;

$$\zeta = \frac{c_{eq}}{c_c} = \frac{c_{eq}}{2\sqrt{m_{eq}\, k_{eq}}} \ . \tag{4.2}$$

The natural frequency of a spring mass system is defined by Eq. (4.3) as;

$$\omega_n = \sqrt{\frac{k_{eq}}{m_{eq}}} \ , \tag{4.3}$$

where the stiffness k_{eq} for each loading condition should be initially calculated. The power output of this system will be higher is the system is operating at natural frequency which dictates the selection of material and dimensions. The terms "natural frequency" and "resonant frequency" are used alternatively in literature, where natural frequency of piezoelectric system should not be confused with the natural frequency of mechanical system.

For the circular diaphragm, the equivalent stiffness and mass can be represented as [6] (see Appendix C);

$$k_{eq} = \frac{16\,\pi\, t_d^3 (Y_0 + T)}{a^2(1-\sigma^2)} \quad \text{and} \quad m_{eq} = \frac{9\,\rho\, t_d (\pi a^2)}{5} \ , \tag{4.4}$$

where Y_0 is the Young's modulus, T is the residual stress, and σ is the Poisson's ratio of the diaphragm. Thus, the first natural resonance frequency can be written in terms of the equivalent mass, m_{eq}, and the stiffness, k_{eq}, of the diaphragm [10] as;

$$f_r = \frac{1}{2\pi}\sqrt{\frac{k_{eq}}{m_{eq}}} = \frac{2}{\pi}\left(\frac{t_d}{a^2}\right)\sqrt{\frac{Y_0 + T}{1.8\rho(1-\sigma^2)}} \ . \tag{4.5}$$

4.2.2 Remodeling of Diaphragm Structure

Test samples of the diaphragm structure were fabricated, as shown in Fig. 4.2, to investigate the resonant frequency experimentally. From the samples, the following serious problems were found: an increasing in the residual stress in the diaphragm caused by the self-strain, a reduction in the electrode area caused by self-healing effect of the piezoelectric polymer [11], and short circuiting caused by pinholes formed in the film formation process.

Because of the difference in the deposition method of the top and bottom electrodes, flexure and the formation of wrinkles occur which are caused by the self-strain and residual stress, as shown in Figs. 4.3 (b) and (c), respectively. Residual stress is generated in multilayered diaphragms during the fabrication process, mainly due to mismatches between the thermal expansion coefficients of

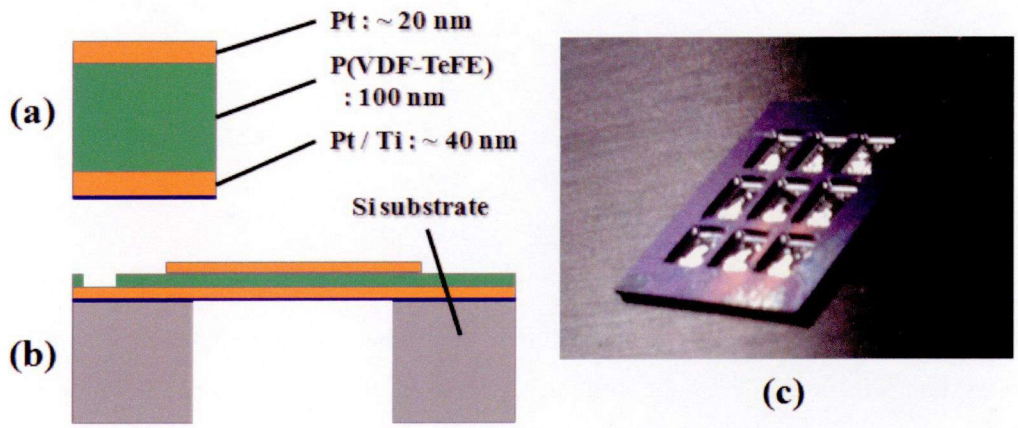

Fig. 4.2 A schematic diagram of (a) the diaphragm structure, (b) cross-sectional view of diaphragm, and (c) a photo image of the test sample

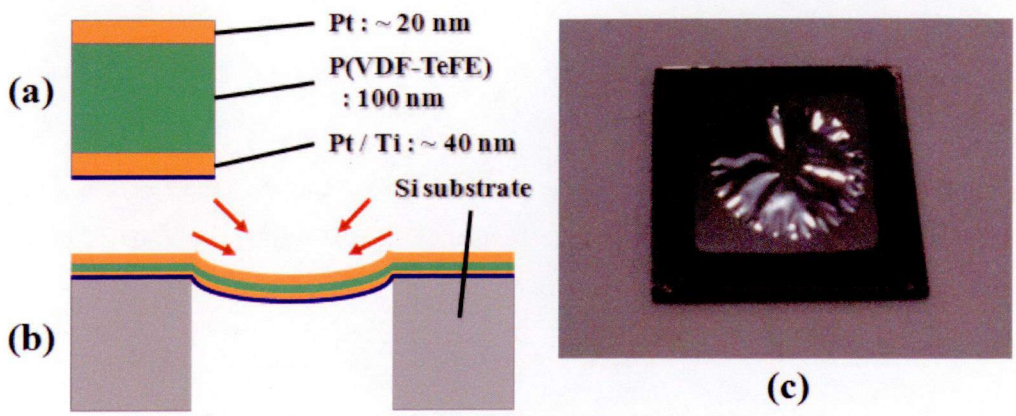

Fig. 4.3 A schematic diagram of (a) the diaphragm structure, (b) cross-sectional view of the diaphragm bent by a self-strain, and (c) a photo image of a test sample, which has an expanded diaphragm

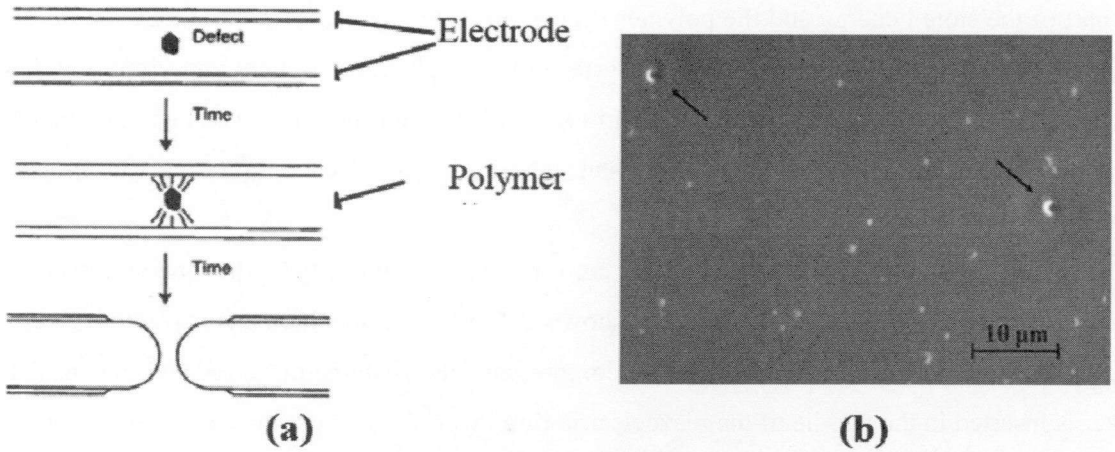

Fig. 4.4 (a) A schematic diagram of self-healing effect in a piezoelectric polymer (from [11]), and (b) a typical microscopic image of holes formed by self-healing effect

different layers. The high-temperature deposition processes, the different thermal and elastic properties of the consecutive layers, and/or some other fabrication issues result in significant residual stress in the device. The stress generated in the device bends the membrane downward or upward depending on whether the stress is tensile or compressive. Moreover, the stress affects the mechanical and electrical properties of the films as well as the resonant frequency and sensitivity of the devices.

Several researchers have investigated the effects of initial tension on the diaphragm's resonant frequency, either theoretically or by finite element analysis [12, 13]. They concluded that initial tension increases the stiffness of the diaphragm and increases its resonant frequency. In fact, the vibrational behavior of the diaphragm changes from that of a plate with negligible tension to that governed by a diaphragm with negligible stiffness owing to the generation of residual stress in the diaphragm.

The self-healing process is schematically illustrated in Fig. 4.4 (a). When electrical breakdown occurs (in many cases around the defects in the polymers), the breakdown results in the discharge

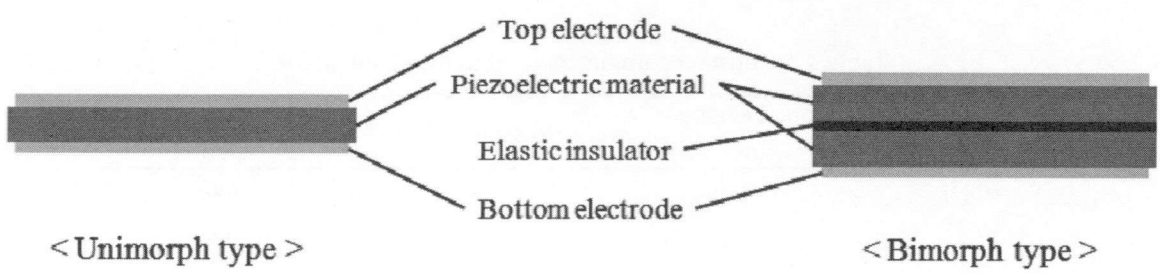

Fig. 4.5 Two types of the diaphragm structure: unimorph type (left side) and bimorph type (right side)

of part of the stored energy and the polymer film is punctured by the released energy. At the same time, the metal electrode deposited on the surface of the polymer is rapidly vaporized and driven outward from the breakdown site as shown in Fig. 4.4 (b). After these processes, the polymer film will break down "open circuit" rather than "short circuit". Hence, piezoelectric properties deteriorate with decreasing electrode area.

In order to solve these problems, the conventional unimorph-type diaphragm structure is remodeled as a bimorph-type diaphragm as shown in Fig. 4.5. In the three layers (bottom electrode, top electrode, and piezoelectric thin film) compressing the diaphragm remodeled, an insulating layer is inserted in the middle of the piezoelectric film layer. As a result, the electrical properties of the piezoelectric film are not changed, although the formation of pinholes and the self-healing effect occur in the piezoelectric thin film. Furthermore, wrinkles and the flexure of the diaphragm can be eliminated by adjusting the thickness of the insulating layer inserted into the piezoelectric film layer. However, insertion of the insulating layer increases the resonant frequency owing to the increased the diaphragm thickness and the mechanical impedance of the inserted insulating layer.

4.2.3 Installation of Proof Mass

For the remodeled diaphragm with the bimorph structure introduced in the previous section, the laminated diaphragm was fabricated. Table 4.1 shows constant parameters of the materials comprising the diaphragm, and Table 4.2 shows the calculated constant parameters and estimated resonant frequency for three test samples with different P(VDF-TeFE) thin-film thicknesses, where the thickness is determined by the concentration of the P(VDF-TeFE) casting solution. After a fabrication of testing samples, the measurement of output voltages was carried out at the resonant frequency calculated for each sample. However, the output voltage was very small because a displacement of a diaphragm decreased with increasing frequency of a sound source. Furthermore, since the output voltages of samples are weak for noises because of high impedance due to the capacitive structure of a diaphragm, the output voltage was concealed by noises.

Table 4.1 Constant parameters used in the calculations

Materials	Density (mg/cm^3)	Poisson's ratio	Young's modulus (GPa)
Ni	8.9	0.31	200
Pt	21.4	0.39	168
AlN	3.6	0.22	345
P(VDF-TeFE)	1.9	0.35	2

Table 4.2 Calculated parameters used in the estimation of resonant frequency

Concentration of P(VDF-TeFE) casting solution		1 wt%	3 wt%	5 wt%
Thickness (nm)	Ni	20		
	Pt*1	120 (60 x2)		
	AlN	40		
	P(VDF-TeFE)*1	200 (100 x2)	360 (180 x2)	1200 (600 x2)
	Total	380	540	1380
Calculated parameters of the diaphragm	Density (mg/cm^3)	8.57	6.6	3.73
	Poisson's ratio	0.347	0.347	0.349
	Young's modulus (GPa)	101	71.6	29.2
Estimated resonant frequency*2 (Hz)		1,441	1,972	4,222

*1. Since the diaphragm is bimorph structure, there are 2 layers of Pt and P(VDF-TeFE).
*2. A radius of the diaphragm is 3.8 mm.

Also, as shown in Table 4.2, the resonant frequency calculated with Eq. (4.5) was higher than the fundamental frequency of a human voice. Therefore, in this study, it was attempted to lower the resonant frequency by increasing the equivalent mass of the diaphragm by installing a proof mass at the center of the diaphragm, as shown in Fig. 4.6, during the fabrication process of the device. The resonant frequency is determined by the equivalent stiffness, k_{eq}, and equivalent mass, m_{eq}, in Eq. (4.4). By installing a proof mass, the resonant frequency is decreased because of the increase in the equivalent mass of the diaphragm, even though the equivalent stiffness is also increased by the increased residual stress of the diaphragm. Since the resonant frequency of the diaphragm with a proof mass is difficult to calculate accurately, it is investigated experimentally.

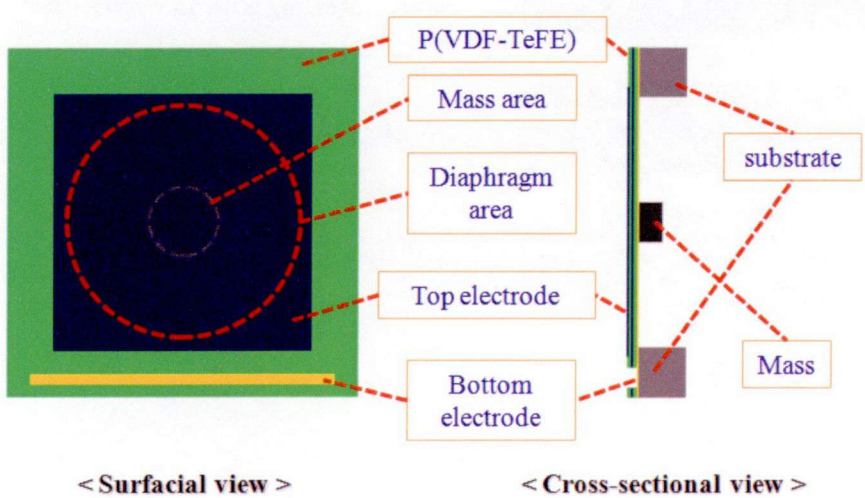

Fig. 4.6 A schematic diagram of the bimorph-type diaphragm with a proof mass

4.3 Fabrication of the Acoustic Energy Harvester

Using the KD7525 mixed solvent referred to in Chapter 2, P(VDF-TeFE) casting solution is made up to form a thin film by the sol-gel process. In order to control the film thickness, three different casting solutions were used with concentrations of 1, 3, and 5 wt%. In order to prevent interfacial delamination between the P(VDF-TeFE) thin film and substrate when using these low-concentration casting solutions, the spin-coating speed is changed flexibly during the spin-coating process.

The fabrication process is shown in Fig. 4.7. The substrate is Si, and Ni is evaporated as a buffer layer between the Si substrate and the bottom Pt layer. The bottom Pt layer is used as a low-resistance electrode. In particular, the bottom Pt layer has two functions; as the bottom electrode and as an etching-stop layer during the RIE process on the backside of the substrate. Then, a P(VDF-TeFE) thin film is coated by a spin-coater in an airtight container in which the temperature and humidity are controlled. The film thicknesses are 100, 180, and 600 nm for casting solution

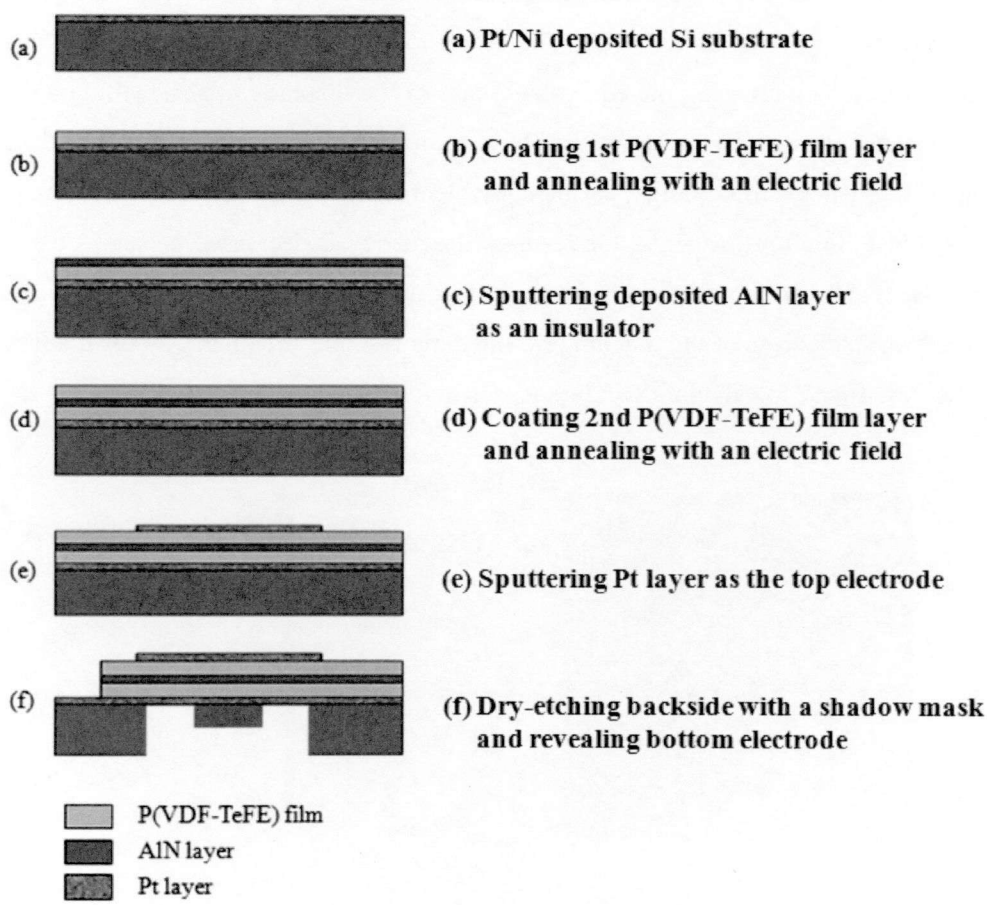

Fig. 4.7 The fabrication procedure of the acoustic energy harvester proposed in the present study

concentrations of 1, 3, and 5 wt%, respectively. After the coating process, the low-pressure annealing process described in Chapter 3 is carried out at 195 °C for 1 hour with the application of an electric field of 1 MV/m. Then, an unpolarized AlN layer is deposited as an insulating layer by sputtering. AlN layer is used to fabricate the bimorph structure of the diaphragm. Then a second P(VDF-TeFE) thin film is coated by the same process as that used for the first P(VDF-TeFE) film. Then, a Pt layer is deposited as the top electrode by sputtering with a shadow mask. Finally, the backside of the Si substrate, which is passivated with a polyimide film, is etched by RIE. The weight of the proof mass is about 1 mg. Fig. 4.8 shows photographs of the fabricated device and a schematic of the layers of the diaphragm.

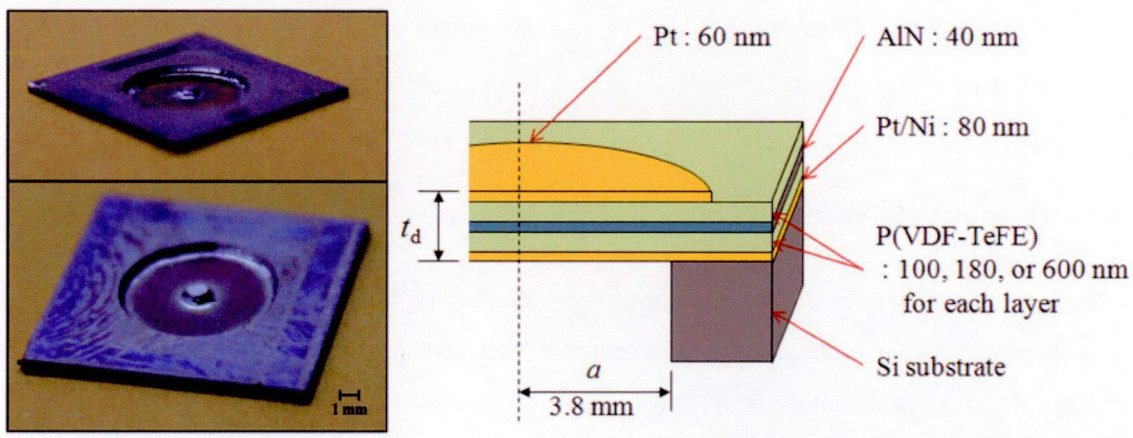

Fig. 4.8 Pictures of the fabricated device (left side) and a schematic diagram of the diaphragm structure with the lamination layer (right side)

4.4 Characteristics of the Acoustic Energy Harvester for the Fundamental Frequency of Human Voice

Since a human voice simultaneously produces sounds of various frequencies, a measuring system is constructed to accurately measure the output voltage of the devices for a sound of single frequency as shown in Fig. 4.9. The distance between the speaker and the device is 5 cm. In order to block the propagation of the vibration by the speaker, shock absorbers are attached to the equipment. Also, a probe set is set up in a sealed cabinet to block environmental noise. The sound source is generated by an amplifier with a DC supply and a function generator to minimize noise signals from the surrounding environment. The range of frequencies is 59~259 Hz, and the acoustic pressure level is 80~120 dB SPL.

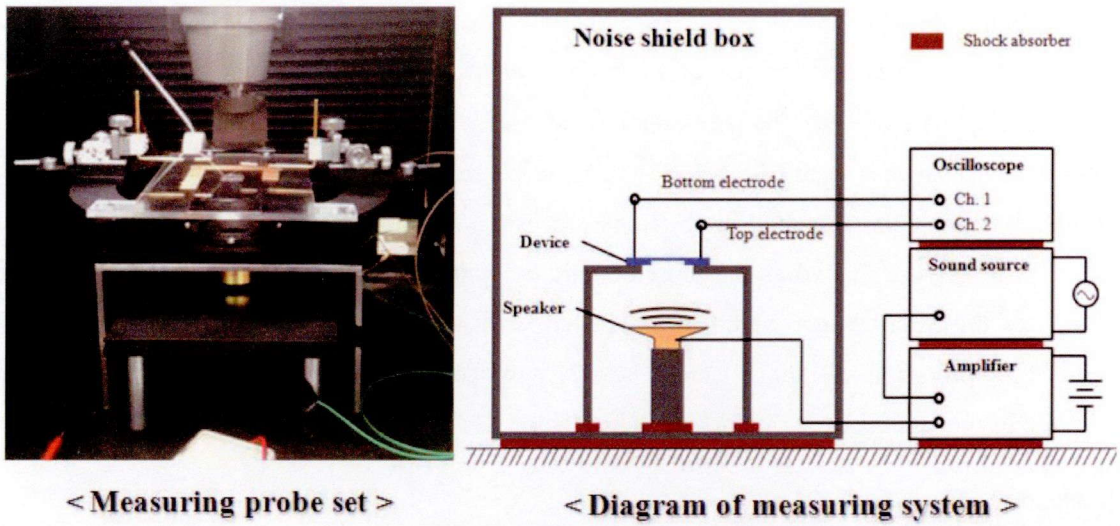

Fig. 4.9 A picture and a schematic diagram of the measuring system for the acoustic energy harvester

4.4.1 Output Voltage for Frequency of Sound

Since the proof mass is very heavy compared with the diaphragm of the samples, the effect of the proof mass on the vibration of the diaphragm was investigated. Fig. 4.10 shows the output voltages of the top and bottom electrodes for each sample. A piezoelectric film generates both positive and negative voltages on each side of the electrode depending on the strain direction. However, the top electrode of the sample only generates positive voltages and the bottom electrode only generates negative voltages. In piezoelectric materials, a surface on which a strain stress is applied generates positive voltages, and a surface on which a compressive stress is applied generates negative voltages. This means that the top electrode is subjected to a strain stress and the bottom electrode is subjected to a compressive stress. Therefore, it was found that the diaphragm

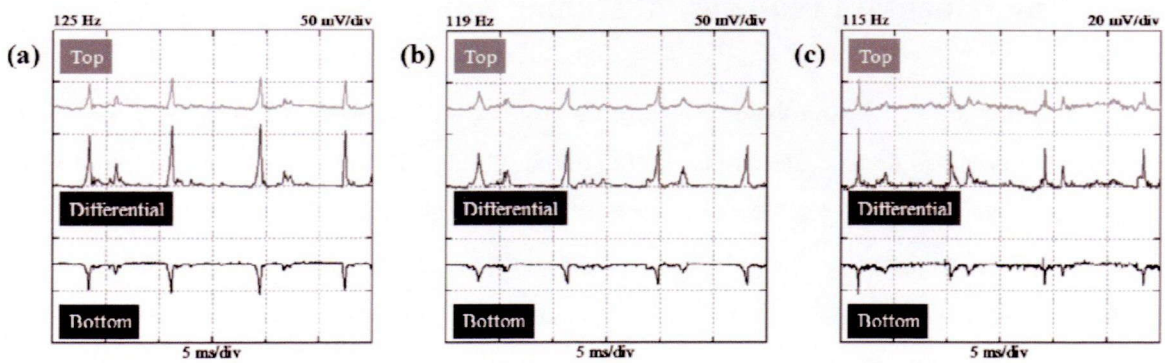

Fig. 4.10 Output voltages of top and bottom electrodes, and differential voltage of (a) sample 1, (b) sample 2, and (c) sample 3, which diaphragm thicknesses are 380, 540, and 1380 nm

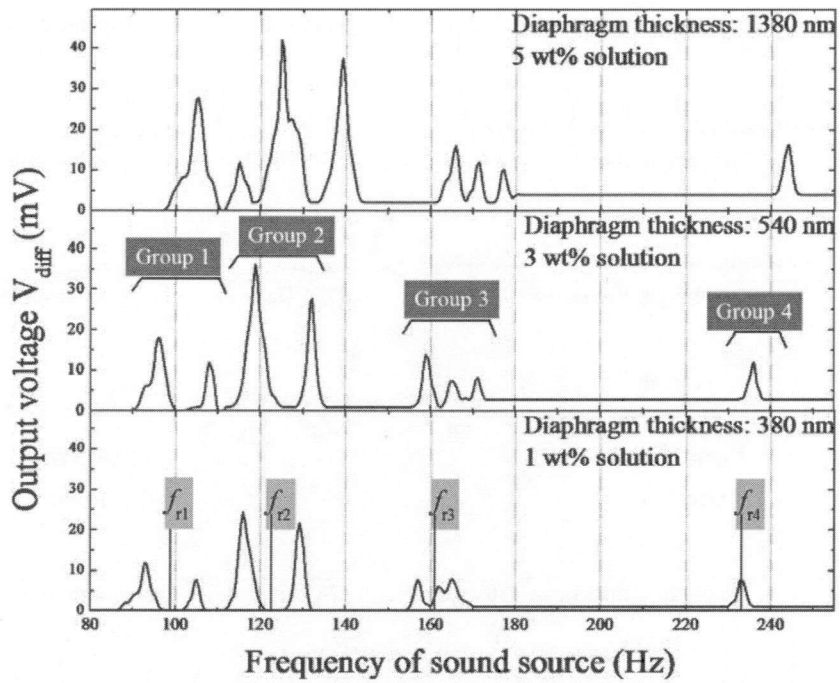

Fig. 4.11 Output voltages measured for three diaphragm thicknesses of (a) 1,380 nm, (b) 540 nm, and (c) 380 nm as a function of the frequency of a sound source (Z_{in} = 1 MΩ)

was vibrated by the proof mass and that the tension of the diaphragm was not in a single direction but in alternating directions. As a result, the waveforms of the output voltage are affected by the limited direction of vibration.

The output voltage, which is the difference between the voltages of the top and bottom electrodes, was measured for different sound frequencies with increments of 0.1 Hz. The acoustic pressure level was fixed at 110 dB SPL because the pressure level changes with the sound frequency. The reference point for the measured voltages is the peak-to-peak voltage of the differential voltage between the top and bottom electrodes. Fig. 4.11 shows the relationship between the output voltage and sound frequency for the three devices with different diaphragm thicknesses. Since the measured voltage is slightly changed by noises and vibrations from the surrounding environment, the output data averaged over 30 measurement results are recorded in Fig. 4.11.

As previously mentioned, the resonant frequency of the diaphragm can be decreased by the installation of a proof mass. All three devices with different diaphragm thicknesses exhibited strong resonance for sounds of 115-125 Hz frequency. The resonant frequency bandwidth depends on the thickness of the diaphragm and the weight of the proof mass. The output voltage also depends on the thickness of the diaphragm, because it is determined by the degree of diaphragm distortion and the number of dipole moments. The diaphragm of 380 nm thickness resonated at

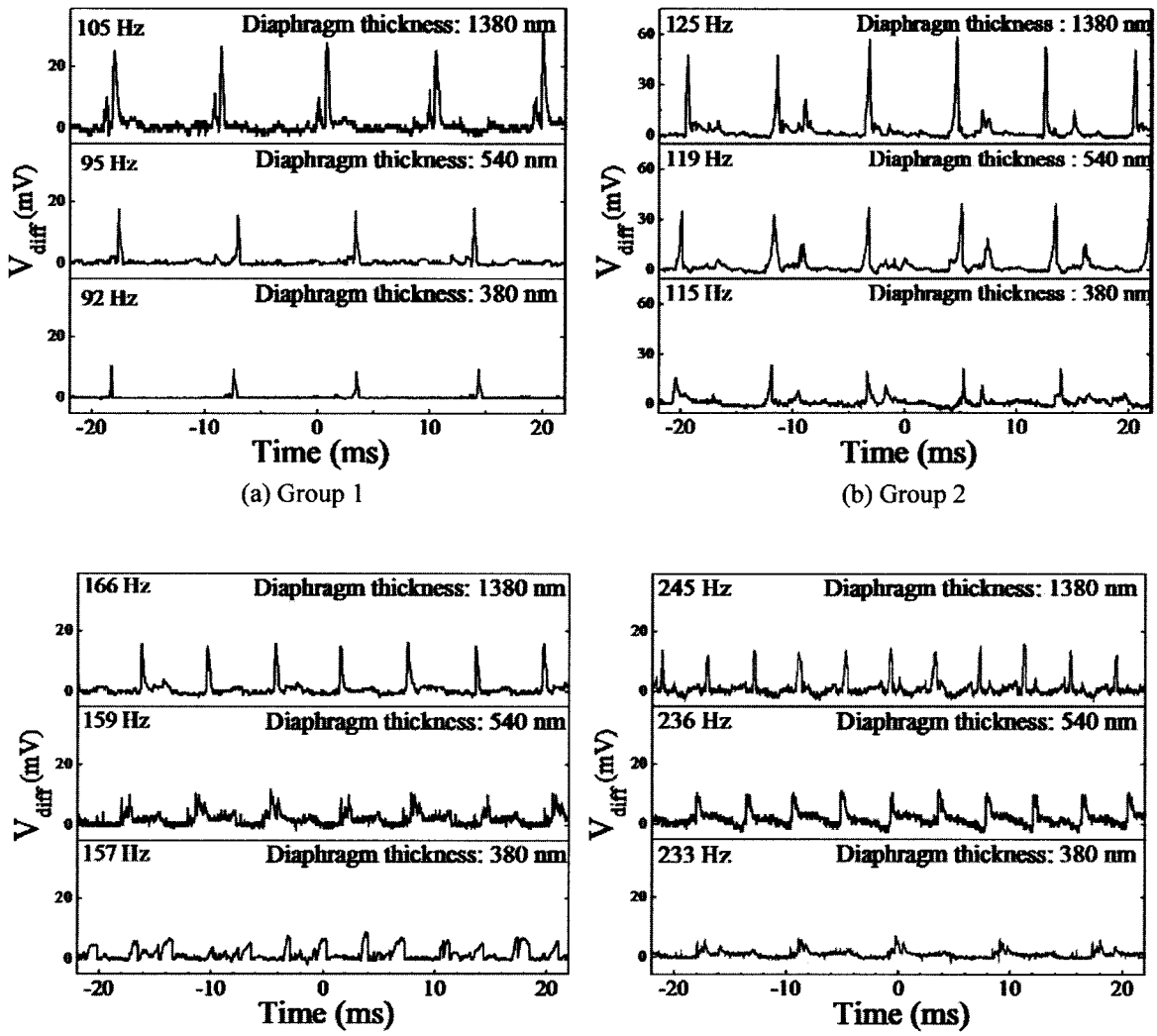

(a) Group 1 (b) Group 2

(c) Group 3 (d) Group 4

Fig. 4.12 Four waveform groups of the measured output voltage for specific frequency of sound source

Table 4.3 Frequency bandwidth of each waveform group for the three fabricated devices

Sample number		1	2	3
Diaphragm thickness (nm)		1380	540	380
Bandwidth (Hz)	Group 1	98 ~ 118	90 ~ 110	87 ~ 106
	Group 2	120 ~ 143	114 ~ 135	112 ~ 132
	Group 3	162 ~ 180	156 ~ 173	155 ~ 170
	Group 4	242 ~ 246	234 ~ 238	230 ~ 235

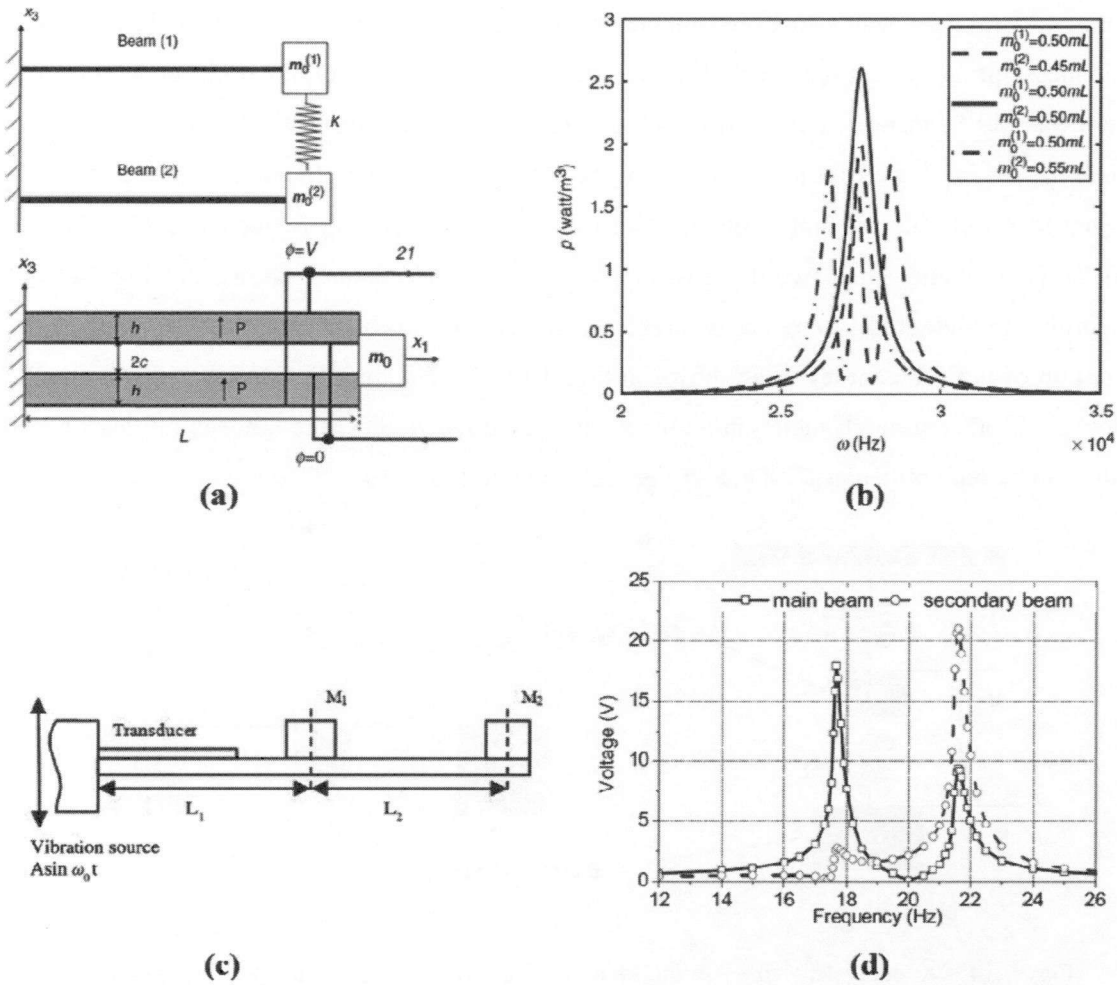

Fig. 4.13 (a) Two beams with end masses elastically connected at their ends, and cross-sectional view of a bimorph beam (form [14]), (b) Power density vs. frequency for different end masses (from [14]), (c) a conventional 2-DOFs cantilever piezoelectric energy harvester (from [15]), and (d) output voltage with secondary mass (from [15])

frequencies from 87 Hz, as shown in Fig. 4.11 (c), whereas the diaphragm of over three times the thickness (1,380 nm) resonated at frequencies from 98 Hz, as shown in Fig. 4.11 (a). For these two cases, the output voltages differed by a factor of two. As shown in Fig. 4.11, the frequency of the first output voltage peak, referred to as the first resonant point, shifted to a higher frequency with increasing diaphragm thickness. However, it is also considered that the concentration of P(VDF-TeFE) casting solution used to control the diaphragm thickness is also related to the output voltage. All the peaks are classified according to the waveform of the measured output voltage, as shown in Fig. 4.12, and Table 4.3 shows the frequency range of each group, in which the same waveform was observed.

Two peaks were observed in each waveform group, excluding group 4. Z. Yang and J. Yang (2009) [14] reported the mathematical analysis of a cantilever with a bimorph structure. As shown

in Fig. 4.13 (a), two beams are used to represent the top and bottom surfaces of an elastic substrate. This mass-spring system represented the interfacial effect of a bimorph cantilever with beams of masses as $m_0^{(1)}$ and $m_0^{(2)}$ and a stiffness assigned between the beams as shown in Fig. 4.13 (b). When $m_0^{(1)} = m_0^{(2)}$, the cantilever vibrates at the resonant frequency. In contrast, if the two masses are not identical, the resonant frequency is divided into two resonant frequencies. Also, Wu *et al.* (2012) [15] studied the two-degrees-of-freedom (2-DOF) system shown in Fig. 4.13 (c). According to their study, there are two resonant frequencies of the main cantilever induced by the vibration of the sub-cantilever, as shown in Fig. 4.13 (d). The main cantilever and sub-cantilever affect each other through their vibration. As in the above studies, the devices fabricated in this study can be represented as a 2-DOF system as shown in Fig. 4.14.

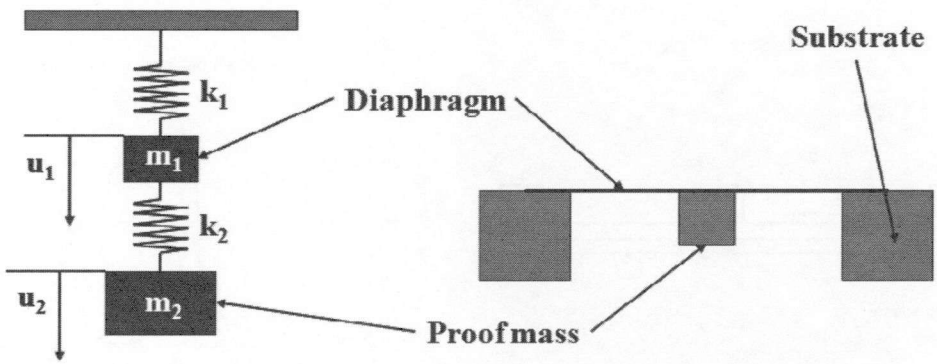

Fig. 4.14 A equivalent mass-spring model of a 2-DOF system for the energy harvester fabricated in this study, where m_1 is a weight of a diaphragm, m_2 is a weight of a proof mass, and k_1 is a stiffness of a diaphragm regardless of k_2, which a stiffness is occurred by a proof mass

The equivalent model in Fig. 4.15 can be discribed as follows.

$$\begin{bmatrix} m_1 & 0 \\ 0 & m_2 \end{bmatrix} \begin{bmatrix} \ddot{u}_1 \\ \ddot{u}_2 \end{bmatrix} + \begin{bmatrix} k_1 & 0 \\ 0 & k_2 \end{bmatrix} \begin{bmatrix} u_1 \\ u_2 \end{bmatrix} = \begin{bmatrix} 0 \\ 0 \end{bmatrix} \tag{4.6}$$

Assume that the system undergoes harmonic motion of the form

$$u_1(t) = U_1 \cos(\omega t - \alpha) \quad \text{and}$$

$$u_2(t) = U_2 \cos(\omega t - \alpha) \ , \tag{4.7}$$

where U_1 and U_2 are signed constants that determine the amplitudes of the two respective sinusoidal motions. Equation (4.7) is substituted into Eq. (4.6) to obtain the following algebraic eigenvalue problem:

$$\left[\begin{bmatrix} (k_1+k_2) & -k_2 \\ -k_2 & k_2 \end{bmatrix} - \omega^2 \begin{bmatrix} m_1 & 0 \\ 0 & m_2 \end{bmatrix} \right] \begin{bmatrix} U_1 \\ U_2 \end{bmatrix} = \begin{bmatrix} 0 \\ 0 \end{bmatrix} \tag{4.8}$$

Since Eq. (4.8) is a set of homogeneous linear algebraic equations, the nontrivial solutions of Eq. (4.8) correspond to values of ω^2 that satisfy the characteristic equation

$$\left|\begin{bmatrix}(k_1+k_2) & -k_2 \\ -k_2 & k_2\end{bmatrix} - \omega_n{}^2 \begin{bmatrix}m_1 & 0 \\ 0 & m_2\end{bmatrix}\right| = 0 \tag{4.9}$$

that is, values of $\omega_n{}^2$ for which the determinant of the coefficients of Eq. (4.8) is equal to zero. Solving to obtain the two roots of the characteristic equation,

$$\omega_n = \sqrt{\frac{1}{2m_1m_2}\left[\{k_2m_1+(k_1+k_2)m_2\} \pm \sqrt{\{k_2m_1+(k_1+k_2)m_2\}^2 - 4m_1m_2k_2(k_1+k_2)}\right]} \tag{4.10}$$

If $m_1 = m_2 = m$ and $k_1 = k_2 = k$,

$$\omega_{n1} = \sqrt{\frac{k}{m}} \qquad \text{and} \qquad \omega_{n2} = \sqrt{\frac{2k}{m}} \tag{4.11}$$

According to Eq. (4.10), there are two natural frequencies in the region of a resonance. Thus, the vibration of the diaphragm is affected by the vibration of the proof mass, and the effect is represented by the waveform of the output voltage. Considering groups 1, 2, and 3 in Fig. 4.11, for a group into which the same waveforms are classified, two resonant frequencies occur as a result of the alternating vibration between the diaphragm and the proof mass. Therefore, the actual resonant frequency exists at the midpoint of the two peaks of the output voltage.

Since a resonant frequency is a constant proportion of the natural frequency for the simple harmonic vibration, it is found that the fabricated devices are vibrated by the vibration modes. The vibration modes are caused by the interference between reflected waves, which are reflected by the edge of the diaphragm, and traveling waves, which propagate from the center of the diaphragm to the edge. When the diaphragm vibrates with the vibration modes, the resonant frequency is not a constant proportion, unlike in electrical resonating systems. According to studies of the vibration modes for a piezoelectric microdiaphragm [16], a diaphragm vibrates with a particular vibration mode at specific frequencies as shown in Fig. 4.15 (a). For a circular diaphragm, the resonant frequencies and their corresponding deflection profiles at different mode shapes are obtained as follows [17]:

$$f_{mn} = \frac{1}{2\pi}\sqrt{\frac{1}{\rho h}\left(\gamma_{mn}{}^4 D + \gamma_{mn}{}^2 T\right)} \tag{4.12}$$

where ρ is the diaphragm density, h is the diaphragm thickness, D is the flexural rigidity, T is the initial tension of the diaphragm per unit length, and γ_{mn} are the eigenvalues, which can be calculated by solving the characteristic equation numerically. Since the devices fabricated in this study correspond to 2-DOF system, D is not a fixed value in Eq. (4.12). When waves of a certain

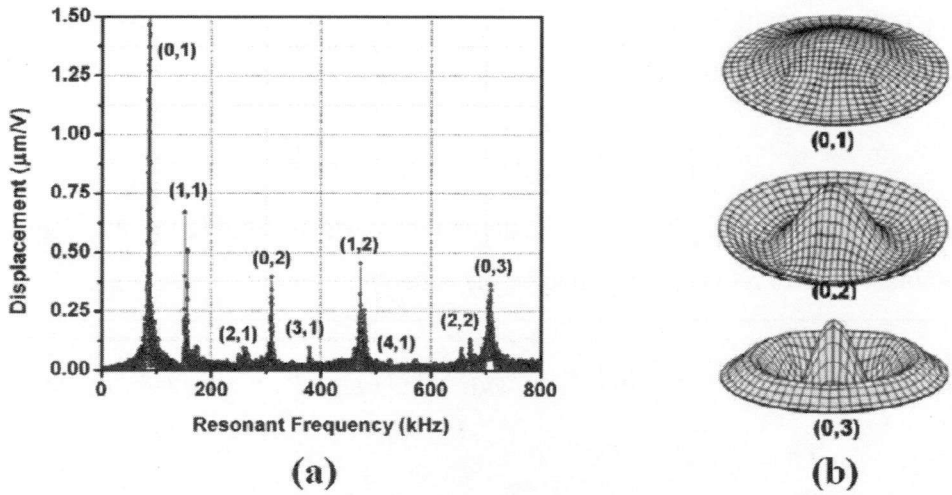

Fig. 4.15 (a) The frequency response of the diaphragm measured by a vibrometer, showing the first nine resonances of the diaphragm (from [16]), and (b) the finite element modeling of the (0, 1), (0, 2), and (0, 3) modes (from [16])

frequency are applied to the diaphragm, the proof mass and diaphragm vibrate with different frequencies, implying the occurrence of a vibration mode.

Since the proof mass has an area on the diaphragm, the traveling and reflected waves are not symmetrical in the axis along which they propagate [18]. If the diaphragm on which a proof mass is installed vibrates with the vibration mode symmetrical to the axis of propagation, the diaphragm will be broken by torsion because of the heavy proof mass. Considering the result from [16], groups 1, 2, and 3 correspond to the (0, 1), (0, 2), and (0, 3) modes, as shown in Fig. 4.15 (b), respectively. In Fig. 4.11, the resonant frequency of each group is different from those of the reported vibration modes. As shown in Fig. 4.15 (a), the (0, 2) mode appears at a frequency 2.3 times higher than that of the (0, 1) mode. The (0, 3) mode also appears at a frequency 5.5 times higher than that of the (0, 1) mode. For the devices fabricated in this study, however, the vibration modes are compressive.

Assigning the groups shown in Fig. 4.12 to the vibration mode, the morphology of the diaphragm for each group can be obtained as shown in Fig. 4.16. In the case of group 1, corresponding to the (0, 1) mode, although the displacement of the diaphragm was largest among the modes, the measured output voltages were lower than those of group 2. As shown in Fig. 4.16 (a), the displacement of the diaphragm is small because of the heavy proof mass. In the case of group 2, corresponding to the (0, 2) mode, the voltage is only generated the distortion of the diaphragm regardless of the proof mass as shown in Fig. 4.16 (b). Since the voltage of the second peak, which appeared along with the first peak as shown in Fig. 4.12 (b), is almost the same as that of the peak in group 1 in Fig. 4.12 (a), the mode transition from (0, 2) to (0, 1) may have been

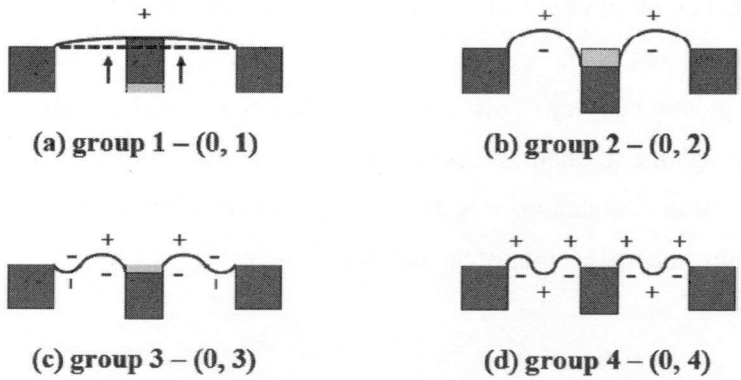

Fig. 4.16 The assignments of vibration modes to each group

induced by the proof mass along with the stiffness of the diaphragm. In the cases of groups 3 and 4, corresponding to the (0, 3) and (0, 4) modes, respectively, the output voltage was lower and the waveform was distorted because of the increased curvature of the diaphragm surface between the substrate and the proof mass, as shown in Figs. 4.16 (c) and (d). In particular, for sample 3 (380 nm) in group 4, the frequency of the output voltage decreased to half the frequency of the sound source. Since the diaphragm of sample 3 is too thin to keep up a proof mass, its elasticity is also low. Thus, for a high-frequency of the sound source, it is considered that the lack of elasticity of the diaphragm makes it difficult to vibrate the proof mass.

The maximum measured voltage is about 50 mV, the peak power calculated from the internal impedance of the used measuring system (1 MΩ) is 50 pW. Table 4.4 shows a comparison of the performance characteristics of the devices in this study and those in the other studies [19-21]. Compared with the previous acoustic energy harvesters, the generated power of the device fabricated in this study is relatively high and its resonant frequency is the lowest. Since the

Table 4.4 Comparison of performances among the acoustic energy harvesters

	Diaphragm diameter (mm)	Resonant frequency (Hz)	Generated power (pW)	Acoustic pressure (db SPL)	Piezoelectric material
S.B. Horowitz *et al.* [19]	3.6	5232	0.7	133	PZT
S. Shinoda *et al.* [20]	2.0	18020	5.1	100	PZT
S. Iizumi *et al.* [21]	2.0	4920	82.8	100	PZT
This study	7.6	120	50	110	P(VDF-TeFE)

piezoelectric properties of P(VDF-TeFE) are inferior to those of PZT, which was used in the acoustic energy harvesters in the previous studies, and the diaphragm distortion is very small because the sound pressure is very small, it is difficult to obtain a high output voltage.

As a result, although the resonant frequency region can be lowered by the installation of a proof mass, the vibration of the diaphragm was disturbed by the proof mass. A high electric power can be expected by controlling the weight of the proof mass.

4.4.2 Output Power in terms of Acoustic Power

Sound is a sequence of pressure waves that propagate through a compressible medium such as air or water, and these waves generate the ambient atmospheric pressure. A piezoelectric film generates the electric potential from a strain or pressure applied to the film. Since the pressure or strain applied to the piezoelectric film increases with increasing sound pressure reaching the film, the output voltage of the piezoelectric film also increases. Therefore, the output voltage as a function of the acoustic pressure level was measured as shown in Fig. 4.17. The acoustic pressure level or sound pressure level was measured at a distance of 5 cm from the sound source using a digital sound level meter (Smart Sensor® AR814). The frequencies of the sound source applied were 116, 119, and 125 Hz, at which the three samples generated the maximum output voltage. For the same acoustic pressure level, the output voltage increased with increasing diaphragm thickness [18]. However, the mechanical impedance of the diaphragm also increased with increasing diaphragm thickness. Thus, the acoustic pressure level at which the diaphragm was vibrated also increased. The acoustic pressure level L_p is defined as,

$$L_p = 20 \log_{10} \left(\frac{p_{\text{rms}}}{p_{\text{ref}}} \right) , \tag{4.13}$$

where p_{rms} is a measured root-mean-square (rms) sound pressure, and p_{ref} is a reference sound pressure, typically 20 μPa, which is generally considered the threshold of human hearing.

Using Eq. (4.13), the sound pressure at a specific distance can be calculated. From the area reached by the sound, the acoustic power P_{ac} can be calculated as the product of the acoustic intensity (I) and the area (A) reached by the acoustic waves:

$$P_{\text{ac}} = I \cdot A = \frac{p^2 \cdot A}{Z} , \tag{4.14}$$

where p is the acoustic pressure and Z is the acoustic impedance. The acoustic impedance can be expressed as $Z = c \cdot \rho$, where c is the sound speed and ρ is the density of the medium. The acoustic

impedance of sound in air is 413.3 Pa·s/m at 20 °C, and the area of the diaphragm, A, was 3.8π x 10^{-6} m^2.

Fig. 4.18 shows the relationship between the acoustic power, calculated using Eq. (4.14), and the output power, calculated from the measured output voltage and internal impedance of the measuring system. The output power is directly proportional to the acoustic power up to a point, and the power subsequently converges to a constant value. This constant value is proportional to

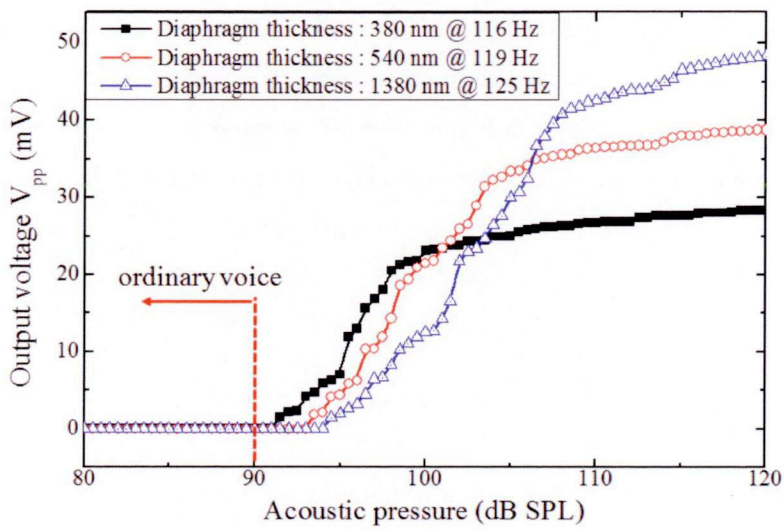

Fig. 4.17 Output voltages obtained from the devices as a function of the acoustic pressure for different diaphragm thicknesses

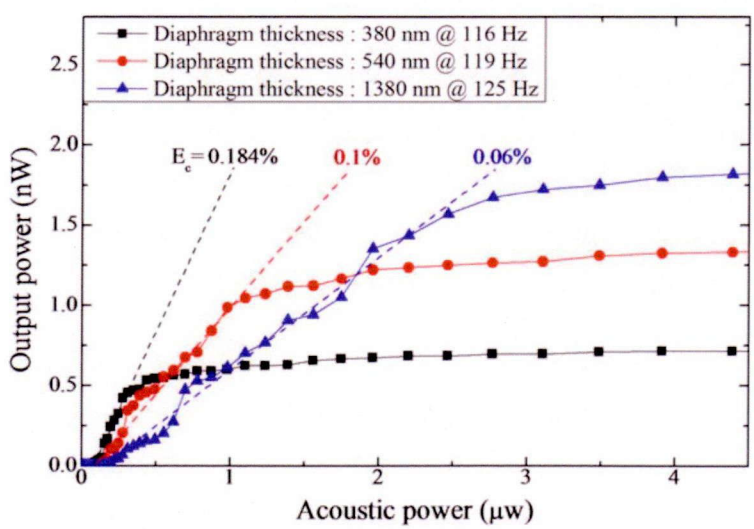

Fig. 4.18 Output powers obtained from output voltages and an impedance of the measuring system as a function of the acoustic power calculated by an acoustic pressure level

the maximum output voltage that can be generated by the sample. The slope of the measured data gives the conversion efficiency E_c. In the region where the output power is proportional to the acoustic power, the conversion efficiencies of the three samples with diaphragm thickness of 380, 540, and 1380 nm are 0.184%, 0.1%, and 0.06%, respectively. The maximum output power is directly proportional to the diaphragm thickness, and the conversion efficiency is inversely proportional. The conversion efficiencies of the samples fabricated in this study are low compared with that of a microphone; the conversion efficiency of a typical microphone (sensitivity: 10 mV/Pa, impedance: 660 Ω) is about 30%. The sensitivities of a typical microphone and the fabricated samples are similar; however, there is a large difference in internal impedance. The fabricated samples have a capacitive structure; thus, their impedance is very high. As a result, to obtain high conversion efficiency and a output voltage, the diaphragm should be thin to reduce the impedance and the material of the diaphragm should have high piezoelectricity.

4.5 Conclusion

As reported in this chapter, the author fabricated an acoustic energy harvester in which acoustic energy is converted to electric energy using a piezoelectric diaphragm fabricated with MEMS techniques. The resonant frequency of the diaphragm was calculated with an equivalent circuit so that the laminated diaphragm could be fabricated. The fabricated device was resonated at the fundamental frequency of a human voice. The results are summarized as follows.

1. With an equivalent circuit of the device, the resonant frequency was calculated to determine an appropriate thickness for the diaphragm. In the first design, the calculated frequency was 535.5 Hz. Although the calculated frequency was near the fundamental frequency of a human voice, critical problems, such as pinholes problem and self-healing effect, occurred in the fabricated devices.

2. In order to fabricate a pinhole-free structure and to reduce residual stress, the laminated structure of the diaphragm was redesigned to change the diaphragm from a unimorph structure to a bimorph structure. Since the thickness of the diaphragm was increased by changing the structure, a remedy was needed to reduce the resonant frequency. In this study, the installation of a proof mass was chosen.

3. Using the remodeled diaphragm structure, the acoustic energy harvester was fabricated and measurements were carried out for sound in the range of 59~259 Hz. The fabricated devices were resonated at 115~125 Hz near the fundamental frequency of a human voice. Through the analysis of the waveforms of the output voltage, it was observed that the vibration mode number affects the shape of the vibrating diaphragm. The maximum generated power was 50 pW for sound of 110 dB SPL.

4. The maximum conversion efficiency of the device fabricated in this study was 0.184 %. This efficiency is very low compared with a typical microphone. The efficiency of a typical microphone is about 30%. The fabricated device and a typical microphone are different in internal impedance, so that the conversion efficiencies are different.

5. The reasons for the improved performance of the fabricated devices were considered by analyzing the output voltage in terms of the acoustic pressure level. Since the output voltage was very small even though the resonant frequency was the fundamental frequency of a human voice, it is necessary to remodel the laminated structure of the diaphragm and to improve the piezoelectric material.

References

[1] J. D. Foster and R. M. White, "Electrophoretic Deposition of The Piezoelectric Polymer P(VDF-TrFE)," Proc. of. 201st Meeting of the Electrochemical Society, Philadelphia (2002).

[2] R. Taylor, F. Liu, S. Horowitz, K. Ngo, T. Nishida, L. Cattafesta, and M. Sheplak, "Technology Development for Electromechanical Acoustic Liners," Proc. ACTIVE '04, Paper A04-093 (2004).

[3] H. Traunmüller and A. Eriksson, "The frequency range of the voice fundamental in the speech of male and female adults," unpublished manuscript, can be retrieved from http://www2.ling.su.se/staff/ hartmut/ aktupub.htm (1995).

[4] L. Rayleigh, "The theory of sound," Macmillan, London, 2nd ed. Vol. I (1894), Vol. II (1896).

[5] E. C. Wente, "A condenser transmitter as a uniformly sensitive instrument for the absolute measurement of sound intensity," Phys. Rev. **10**, 39 (1917).

[6] W. P. Mason, "Electromechanical Transducers and Wave Filters," Van Nostrand D. Company Inc., New York, 2nd ed. (1948).

[7] M. I. Haller and B. T. Khuri-Yakub, "A surface micromachined electrostatic ultrasonic air transducer," IEEE Trans. Ultrason. Ferroelect. Freq. Contr. **43**, 1 (1996).

[8] I. Ladabaum, X. Jin, H. T. Soh, and B. T. Khuri-Yakub, "Surface Micromachined Capacitive Ultrasonic Transducers," IEEE Trans. Ultrason. Ferroelect. Freq. Contr. **45**, 678 (1998).

[9] R. D. Blevin, "Formulas for natural frequencies and mode shape," Robert E. Krieger Publishing, Malabar, Florida (1979).

[10] S. Olcum, M. N. Senlik, and A. Atalar, "Optimization of the Gain-Bandwidth Product of Capacitive Micromachined Ultrasonic Transducers," IEEE Trans. Ultrason., Ferroelect., Freq. Contr. **46**, 1364 (1990).

[11] K. Ren, S. Liu, M. Lin, Y. Wang, and Q. M. Zhang, "A compact electroactive polymer actuator suitable for refreshable Braille display," Sensors and Actuators A **143**, 335 (2008).

[12] S. Lee, T. Tanaka, K. Inoue, J. Kim, Y. Shin, and M. Okuyama, "Stress influences on the ultrasonic transducers," Sensors and Actuator A **119**, 405 (2005).

[13] P. Muralt, A. Kholkin, M. Kohli, and T. Maeder, "Piezoelectric actuation of PZT thin-film diaphragms at static and resonant conditions," Sensors and Actuators A **53**, 398 (1996).

[14] Z. Yang and J. Yang, "Connected Vibrating Piezoelectric Bimorph Beams as a Wide-band Piezoelectric Power Harvester," J. Intell. Mater. Syst. Struct. **20**, 569 (2009).

[15] H. Wu, L. Tang, Y. Yang, and C. K. Soh, "A novel two-degrees-of-freedom piezoelectric energy harvester," J. Intell. Mater. Syst. Struct. **24**(3), 357 (2012).

[16] M. Olfatnia, V. R. Singh, T. Xu, J. M. Miao, and L. S. Ong, "Analysis of the vibration modes of piezoelectric circular microdiaphragms," J. Micromech. Microeng. **20**, 085013 (2010).

[17] M. Olfatnia, T. Xu, L. S. Ong, J. M. Miao, and Z. H. Wang, "Investigation of residual stress and its effects on the vibrational characteristics of piezoelectric-based multilayered microdiaphragms," J.

Micromech. Microeng. **20**, 015007 (2010).

[18] H. G. Yu, L. Zou, K. Deng, R. Wolf, S. Tadigadapa, and S. T. McKinstry, "Lead zirconated titanate MEMS accelerometer using interdigitated electrodes," Sensors and Actuators A **107**, 26 (2003).

[19] S. B. Horowitz, M. Sheplak, L. N. Cattafesta III and T. Nishida, "A MEMS acoustic energy harvester," J. Micromech. Microeng. **16**, S174-181 (2006).

[20] S. Shinoda, T. Tai, and Y. Nishioka, "Lead Zirconate Titante Acoustic Energy Harvester Proposed for Microelectromechanical System/IC integrated Systems," Jpn. J. Appl. Phys. **49**, 04DL21 (2010).

[21] S. Iizumi, S. Kimura, S. Tomioka, and Y. Nishioka, "Lead Zirconate Titanate Acoustic Energy Harvesters Utilizing Different Polarizations on Diaphragm," Procedia Engineering **25**, 187 (2011).

Chapter 5
Conclusions

In this dissertation, I have studied the development of an acoustic energy harvester for the fundamental frequency of a human voice using a piezoelectric polymer. For a voice with a comparatively low frequency, the diaphragm of the device has to be highly sensitive to low acoustic pressures. For this reason, a piezoelectric polymer with lower mechanical impedance than other piezoelectric materials was used in these studies; the polymer used was P(VDF-TeFE), which is a PVDF copolymer. Since the diaphragm of the device fabricated in this study does not employ an elastic substrate, the piezoelectric film has to be thin and flat, and chemically pure.

In Chapter 2, on the basis of the sol-gel process, the techniques used to form P(VDF-TeFE) films based on the sol-gel process for the fabrication of the diaphragm of the acoustic energy harvester are described. The effects of a mixture of solvents, and the annealing temperature were experimentally observed, in addition to the internal and external of the formed films.

- In the formation of P(VDF-TeFE) films by the sol-gel process, controlling the concentration of the casting solvents is more efficient than controlling the spin-coating speed. The probability of interfacial delamination between the film and substrate is increased with increasing spin-coating speed.
- Even though a thin film is easily formed using a low-concentration casting solution, interfacial delamination occurs because the viscosity of the casting solution is also low. Hence, the mixed solvents containing MEK and DMAc can be used to control the viscosity.
- The morphology of the formed film is stable even though the annealing temperature is higher than the melting point of P(VDF-TeFE). However, the piezoelectricity of the film is decreased or lost when the annealing temperature is higher than the Curie point of P(VDF-TeFE).
- As a result, in order to apply P(VDF-TeFE) thin films to the diaphragm, it is necessary to remove the impurities on the film surface and the remaining solvents in the film. Also, remedies are needed to carry out an annealing process at a temperature higher than the Curie point of P(VDF-TeFE).

In Chapter 3, in order to supplement and improve the weak points of the general sol-gel process, the annealing process in a low-pressure chamber with the application of an electric field is proposed. By considering the surface morphology, the existence of impurities, and the remanent polarization, the suitability of the proposed annealing process is compared with that of the conventional annealing process.

- The formation of pinholes cannot be eliminated by the low-pressure annealing process. However, the process changes the morphology of the pinhole. The pinhole diameter is increased and the depth is reduced, resulting in improved electric properties of P(VDF-TeFE) films.
- According to the XPS and FTIR spectra, the amounts of impurities and amorphous P(VDF-TeFE) are decreased by the low-pressure annealing process through the prevention of the contamination with impurities and the removal of solvents remaining from the spin-coating process.
- In order to reduce the roughness of the film surface, the annealing temperature should be higher than the melting point of P(VDF-TeFE). Although here is a risk of reducing or eliminating the remanent polarization at high temperatures, the remanent polarization is preserved by applying an electric field during the annealing process.
- As a result, the problems associated with the formation of a P(VDF-TeFE) thin film by the sol-gel process and thermal treatment can be solved by employing the proposed annealing process.

As reported in Chapter 4, I fabricated an acoustic energy harvester in which acoustic energy is converted to electric energy using a piezoelectric diaphragm fabricated with MEMS techniques. The resonant frequency of the diaphragm is calculated with an equivalent circuit, so that the laminated diaphragm can be fabricated. The fabricated device is resonated at the fundamental frequency of a human voice.

- Using the Mason model, the resonant frequency of the diaphragm is calculated to determine an appropriate thickness for the diaphragm. In the first design, the calculated frequency is 535.5 Hz. Although the calculated frequency is near the fundamental frequency of a human voice, critical problems occur in the fabricated devices.
- In order to fabricate a pinhole-free structure and to reduce residual stress, the laminated structure of the diaphragm is redesigned to change the diaphragm from a unimorph structure to a bimorph structure. Since the thickness of the diaphragm is increased by changing the

diaphragm structure, some remedies are needed to reduce the resonant frequency. In this study, the installation of a proof mass is chosen.

- Using the remodeled diaphragm structure, the acoustic energy harvester is fabricated and measurements are carried out for sound in the range of 59~259 Hz. The fabricated devices are resonated at 115~125 Hz, near the fundamental frequency of a human voice. Through analysis of the waveforms of the output voltage, the vibration mode number affects the shape of the vibrating diaphragm. The maximum generated power is 50 pW for a sound of 110 dB SPL.
- The maximum conversion efficiency was 0.184 %. This efficiency is very low compared with a typical microphone. The efficiency of a typical microphone is about 30%. The fabricated device and a typical microphone are different in internal impedance, so that the conversion efficiencies are different.
- The reasons for the improved performance of the fabricated devices are considered by analyzing the output voltage in terms of the acoustic pressure level. Since the output voltage is very small even though the resonant frequency is the fundamental frequency of a human voice, it is necessary to remodel the laminated diaphragm structure and to improve the piezoelectric material.

The major advantages of using the piezoelectric polymer P(VDF-TeFE) for actuation are its flexibility, light weight, and relatively low Young's modulus. Another benefit of using P(VDF-TeFE) is that it can be used as a sensor as well as an actuator, if required, in a given application. Even though the fabrication of an integrated microdevice will involve multiple layers and more complicated fabrication techniques, the use of P(VDF-TeFE) is expected to help in integrating the diaphragm fabrication process with that of the piezoelectric device.

A more detailed simulation-based study of the effects of the interfacial microstructure on the pressure and deflection of the P(VDF-TeFE) diaphragm would help to improve its performance further through the achievement of either low deflection or a small acoustic pressure. More comprehensive work is required to model and fabricate the acoustic energy harvester so that human voices can be used as a source of electric power.

Appendix. A

X-ray Photoelectron Spectroscopy

In this chapter, the XPS spectra, referred in Chapter 2 and 3, are described. Surface analysis by x-ray photoelectron spectroscopy (XPS), more commonly known as electron spectroscopy for chemical analysis (ESCA), is accomplished by irradiating a sample with monoenergetic soft x-rays and energy analyzing the electrons emitted. The XPS process is schematically represented in Fig. A.1 for the emission of an electron from the shell of an atom. MgK_α x-rays or AlK_α x-rays are ordinarily used. These photons have limited penetrating power in a solid, of the order of 1 ~ 10 μm. They interact with atoms in this surface region by the photoelectric effect, causing electrons to be emitted. The emitted electrons have kinetic energies given by;

$$K.E. = h\upsilon - B.E. - \phi_s \tag{A.1}$$

where $h\upsilon$ is the energy of the photon, B.E. is the binding energy of the atomic orbital from which the electron ordinates, and ϕ_s is the spectrometer work function. In a first approximation, the work function is the difference between the energy of the Fermi level E_F and the energy of the vacuum level E_V, the zero point of the electron energy scale;

$$\phi_s = E_F - E_V \tag{A.2}$$

This quantity is to be determined by calibration for the spectrometer employed. From equation (A.1) it is clear that only binding energies lower than the exciting radiation (1253.6 eV for MgK_α

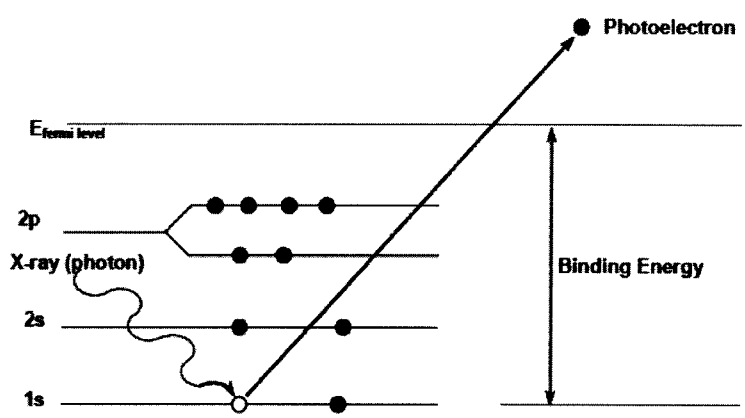

Fig. A.1 A schematic diagram of the XPS process (from [1])

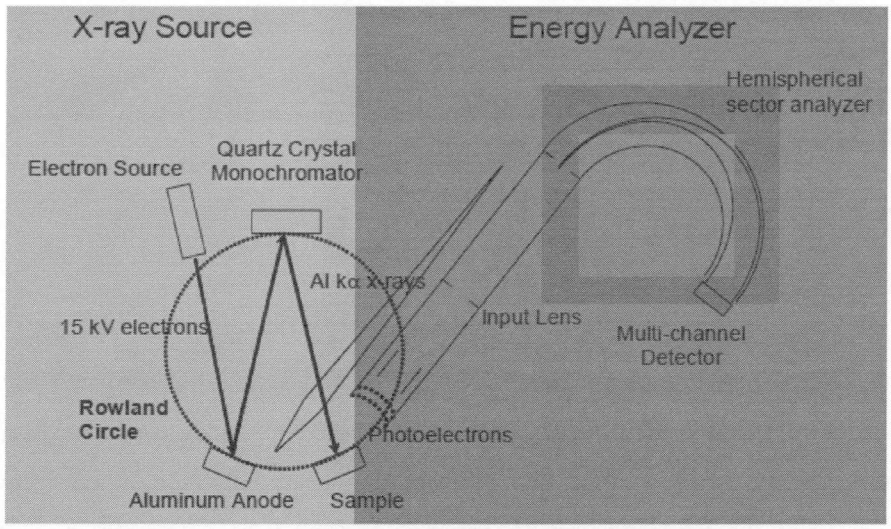

Fig. A.2 A schematic diagram of an XPS set-up with an hemispherical sector analyzer (from [1])

and 1486.6 eV for AlK_{α}) are probed.

The schematic diagram of XPS set-up is shown in Fig. A.2. X-rays illuminate an area of a sample causing electrons to be ejected with a range of energies and directions. The electron optics, which may be a set of electrostatic and/or magnetic lens units, collect a proportion of these emitted electrons defined by those rays that can be transferred through the apertures and focused onto the analyzer entrance slit. Electrostatic fields within the hemispherical analyzer (HSA) are established to only allow electrons of a given energy (the so called Pass Energy, PE) to arrive at the detector slits and onto the detectors themselves. Electrons of a specific initial kinetic energy are measured by setting voltages for the lens system that both focus onto the entrance slit the electrons of the required initial energy and retards their velocity so that their kinetic energy after passing through the transfer lenses matches the pass energy of the hemispherical analyzer. To record a spectrum over a range of initial excitation energies it is necessary to scan the voltages applied to these transfer lenses and the prescription for these lens voltages is known as the set of lens functions. These lens functions are typically stored in some configuration file used by the acquisition system.

In Chapter 2 and 3, there are XPS spectra of carbon 1s and fluorine 1s core electron taken from the P(VDF-TeFE) films. The carbon 1s peak shapes are almost identical, but reveal slight differences in overlay as well as different charging shifts. The asymmetric peak fit for homopolymers of ethylene is after the method of Beamson et al. [2] mirroring their findings with respect to resolution of vibrational levels and again hinting at a 5th level. On the data processing of the XPS spectra of P(VDF-TeFE), the carbon 1s and fluorine 1s binding energies for homopolymers of the ethylene and the fluoroethylene are listed in Table A.1 [3, 4].

Table A.1 Binding energies of the homopolymers of the ethylene and the fluoroethylene

Bonding structure	C_{1s} (eV)	F_{1s} (eV)
$-CH_2-\underline{C}H_2-CH_2-$	285.0	–
$-CH_2-\underline{C}H_2-CFH-$	285.4	–
$-CFH-\underline{C}H_2-CFH-$	285.7	–
$-CH_2-\underline{C}H_2-CF_2-$	285.7	–
$-CFH-\underline{C}H_2-CF_2-$	286.1	–
$-CF_2-\underline{C}H_2-CF_2-$	286.4	–
$-CH_2-\underline{C}FH-CH_2-$	287.9	689.3
$-CH_2-\underline{C}FH-CFH-$	288.4	689.3
$-CH_2-\underline{C}FH-CH_2-$	288.7	689.3
$-CFH-\underline{C}FH-CFH-$	288.7	689.3
$-CH_2-\underline{C}FH-CF_2-$	289.1	690.1
$-CF_2-\underline{C}FH-CF_2-$	289.8	690.1
$-CH_2-\underline{C}F_2-CH_2-$	290.9	689.6
$-CH_2-\underline{C}F_2-CFH-$	291.3	690.1
$-CFH-\underline{C}F_2-CFH-$	291.7	690.1
$-CH_2-\underline{C}F_2-CF_2-$	291.7	690.2
$-CFH-\underline{C}F_2-CF_2-$	292.1	690.2
$-CF_2-\underline{C}F_2-CF_2-$	292.5	690.3

On the data processing of peaks in XPS spectra related to O atoms, the XPS data of the solid electrolyte interphase (SEI) was imposed on this study [5]. The SEI is a solid layer formed with a decomposition of electrolytes in the researches of a Li-ion battery. According to the researches, the electrolyte which is used in a Li-ion battery is an organic solvent such as ethylene carbonate and dimethyl carbonate. Both methyl-ethyl-ketone (MEK) and dimethylacetamide (DMAc), employed in this study, are also an organic solvent. MEK is carbonyl group (R-C=O-R') and DMAc is amide group (R-C=O-N-R'-R"). The most straightforward O_{1s} deconvolution model comprises only two peaks, at around 531 and 533 eV for singly and doubly bond oxygen, respectively [6]. Models based on greater differentiation use up to 5 or more peaks for the O_{1s} deconvolution [7]. The deconvoluted binding energies of C_{1s} and O_{1s} in different chemical environments are listed in Table A.2 and Table A.3.

Table A.2 Deconvolution of the C_{1s} spectra

C_{1s} peak position (eV)	Assignment
283.7 [8], 284 [9], 284.3 [10], 284.4 [11], 284.8 [10], 285.0 [12]	C–H, sp2 carbon
285.5 [13], 286.0 [14], 286.1 [15]	C–OH
286.5 [11]	$-(CH_2-CH_2-O)_n-$
285.0 [14], 285.5 [13], 286.0 [12], 286.5 [9]	C–O–C
286-287 [13], 287.0 [16], 287-288 [10]	C–O–C ether carbon
287.0 [14], 287.3 [15]	C=O
287.6 [17], 289-290 [10]	COOR or C–(OR)(CO_2Li)
288-291 [9], 290.6 [16]	RO–CO_2Li

Table A.3 Deconvolution of the O_{1s} spectra

O_{1s} peak position (eV)	Assignment
532.4 [18], 533.8 [16], 534.5 [10],	RO–CO_2Me (various carbonates)
532.5 [13], 533.0 [10], 534.0 [18]	C–O–C or C–O–H
531.0 [14]	C=O
530.8 [14]	C–O–Me

References

[1] G. W. Nelson, M. Perry, S.-M. He, D. L. Zechel, and J. Hugh Horton, "Characterization of covalently bonded proteins on poly(methyl methacrylate) by X-ray photoelectron spectroscopy," Coll. Surf. **B78**, 61 (2010).

[2] G. Beamson, D. T. Clark, J. Kendrick, and D. Briggs, "Observation of vibrational asymmetry in the high resolution monochromatized XPS of hydrocarbon polymers," J. Electr. Spectroscopy & Rel. Phenom. **57**, 79 (1991).

[3] D. T. Clark, W. J. Feast, D. Kilcast, and W. K. R. Musgrave, "Applications of ESCA to Polymer Chemistry. III. Structures and Bonding in Homopolymers of Ethylene and the Fluoroethylenes and Determination of the Compositions of Fluoro Copolymers," J. Polym. Sci. Polym. Chem. **11**, 389 (1973).

[4] G. Beamson and D. Briggs, "High Resolution XPS of Organic Polymers: The Scienta ESCA 300 Database," Wiley, New York, (1992).

[5] E. Peled, "The Electrochemical Behavior of Alkali and Alkaline Earth Metals in Nonaqueous Battery Systems - The Solid Electrolyte Interphase Model", J. Electrochem. Soc. **126**, 2047 (1979).

[6] S. Kundu, Y.-M. Wang, W. Xi, M. Muhler, "Thermal stability and reducibility of oxygen-containing functional groups on multiwalled carbon nanotube surfaces: A quantitative high-resolution XPS and TPD/TPR study," J. Phys. Chem. C **112**(43), 16869 (2008).

[7] J.-H. Zhou, Z.-J. Sui, P. Li, D. Chen, Y.-C. Dal, W.-K. Yuan, "Structural characterization of carbon nanofibers formed from different carbon-containing gases," Carbon **44**(15), 3255 (2006).

[8] D. Bar-Tow, E. Peled, and L. Burstein, "A Study of Highly Oriented Pyrolytic Graphite as a Model for the Graphite Anode in Li-ion Batteries," J. Electrochem. Soc. **146**(3), 824 (1999).

[9] S.-H. Kang, D. P. Abraham, A. Xiao, and B. L. Lucht, "Investigating the solid electrolyte interphase using binder-free graphite electrodes," J. Power Sources **175**, 526 (2008).

[10] A. M. Andersson and K. Edstrom, "Chemical Composition and Morphology of the Elevated Temperature SEI on Graphite," J. Electrochem. Soc. **148**(10), A1100 (2001).

[11] H. Bryngelsson, M. Stjerndahl, T. Gustafsson, K. Edstrom, "How Dynamic is the SEI?" J. Power Sources **174**, 970 (2007).

[12] K. Edstrom, M. Herstedt, and D. P. Abraham, "A new look at the solid electrolyte interphase on graphite anodes in Li-ion batteries," J. Power Sources **153**(2), 380 (2006).

[13] V. Eshkenazi, E. Peled, L. Burstein, and D. Golodnitsky, "XPS analysis of the SEI formed on carbonaceous material," Solid State Ion. **170**, 83 (2004).

[14] K. Kanamura, H. Tamura, S. Shiraishi, Z.-I. Takehara, "Morphology and chemical compositions of surface films of lithium deposited on a Ni substrate in nonaqueous electrolytes," J. Electroanal. Chem. **394**, 49 (1995)..

[15] C. Moreno-Castilla, M.V. López-Ramón, and F. Carrasco-Marín, "Changes in surface chemistry of activated carbons by wet oxidation," Carbon **38**(14), 1995 (2000).

[16] K. Morigaki and A. Ohta, "Thermodynamic studies of cobalt and cadmium additions to nickel hydroxide as material for positive electrodes," J. Power Sources **76**, 159 (1998).

[17] L. Zhao, I. Watanabe, T. Doi, S. Okada, J.-I. Yamaki, "TG-MS analysis of solid electrolyte interphase (SEI) on graphite negative-electrode in lithium-ion batteries," J. Power Sources **161**(2), 1275 (2006).

[18] M. Lu, H. Cheng, Y. Yang, "A comparison of solid electrolyte interphase (SEI) on the artificial graphite anode of the aged and cycled commercial lithium ion cells," Electrochim. Acta **53** (2008) 3539.

Appendix. B

Assignments of IR spectra

In this chapter, the FTIR spectra, referred in Chapter 2 and 3, are described. Fourier transform infrared spectroscopy (FTIR) is a technique which is used to obtain an infrared spectrum of absorption, emission, photoconductivity or Raman scattering of a solid, liquid or gas. In infrared spectroscopy, IR radiation is passed through a sample. Some of the infrared radiation is absorbed by the sample and some of it is transmitted. The resulting spectrum represents the molecular absorption and transmission, creating a molecular fingerprint of the sample. Like a fingerprint, no two unique molecular structures produce the same infrared spectrum. Therefore, infrared spectroscopy can result in a positive identification (qualitative analysis) of every different kind of material. In addition, the size of the peaks in the spectrum is a direct indication of the amount of material present.

The FTIR spectra of PVDF and P(VDF-TrFE) were investigated as a preliminary to analyzing FTIR spectra of P(VDF-TeFE). The technique of infrared absorption is suitable to characterize PVDF and its copolymers because the absorption energy of the *gauche* and *trans* configurations of

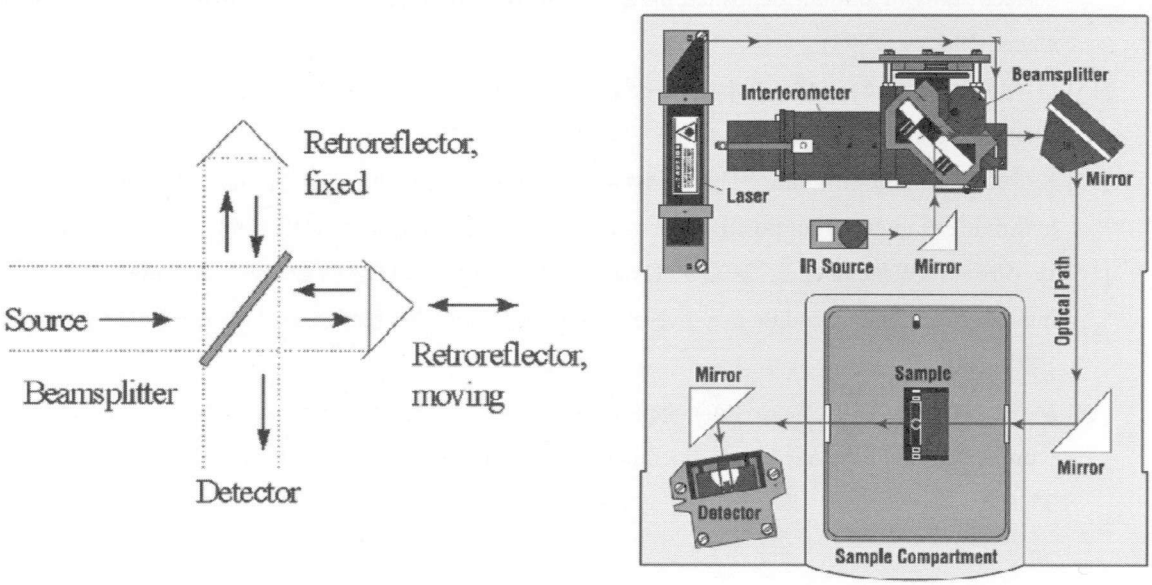

Fig. B.1 A schematic diagram of a Michelson interferometer adapted for FTIR (left side), and a simple spectrometer layout of FTIR (right side) [from http://mmrc.caltech.edu]

Table B.1 Assignments of the FTIR bands of the α-PVDF and P(VDF-TrFE) [1, 2]

PVDF		P(VDF-TrFE)	
Band (cm^{-1})	Assignments	Band (cm^{-1})	Assignments
531	CF_2 δ	840	CF_2 ν_s; CC ν_s
613	CF_2 δ; CCC δ	877	CH_2 r; CF_2 ν_a; CF_2 r
762	CF_2 δ; CCC δ	1067	CC ν_a; CF_2 w; CH_2 w
794	CH_2 r	1178	CF_2 ν_a; CF_2 r
869	CF_2 ν_s; CCC δ	1287	CH_2 ν_s; CC ν_s; CCC δ
974	CH_2 t	1301	CH_2 w; CC ν_a
1067	CF_2 ν_s; CH_2 w	1430	CF_2 δ
1146	CC ν_a; CF_2 ν_s		
1178	CF_2 ν_a; CH_2 w		
1209	CH_2 δ; CH_2 w		
1382	CH_2 δ; CH_2 w		
1401	CH_2 δ; CH_2 w; CC ν_a		

* ν_s, symmetric stretching; ν_a, antisymmetric stretching; δ, scissoring; w, wagging; t, twisting; r, rocking

Table B.2 Assignments of the principal FTIR bands of a MEK and DMAc

Type	Assignments	Band (cm^{-1})
carbonyl – general	C=O stretching	1665 ~ 1760
ketone	C=O stretching	1665 ~ 1745
amide	C=O stretching	1630 ~ 1680
	N-H bending	1515 ~ 1640
alkane	C-H bending	1450 ~ 1470

the PVDF and its copolymers occurs in different wavelengths. The different crystalline phases of the PVDF and its copolymers, or the predominance of some of the crystalline phases, also can be identified by FTIR, because each crystalline phase bands with characteristic relative intensities [1]. The assignments for the main FTIR bands of PVDF and P(VDF-TrFE) are listed in Table B.1.

On the same method as the data processing of XPS spectra, the assignments which are related to two solvents, methyl-ethyl-ketone (MEK) and dimethylacetamide (DMAc), were investigated with studies about the solid electrolyte interphase (SEI). Fig. B.2 shows FTIR spectra of a MEK

and DMAc. The solvents are organic compounds which are a ketone-type and amide-type as a carbonyl group respectively. On the bonding structure of which the organic compounds consist, their assignments are listed in Table C.2 [3-9].

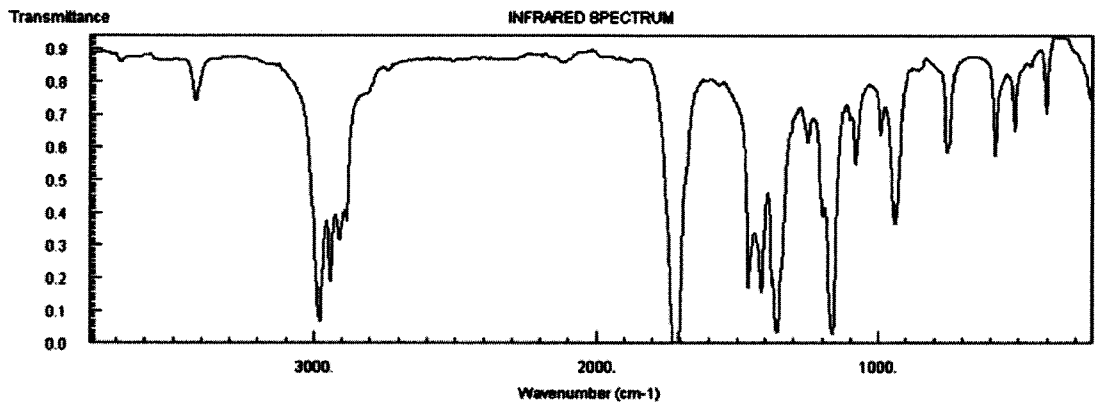

(a) methyl-ethyl-ketone

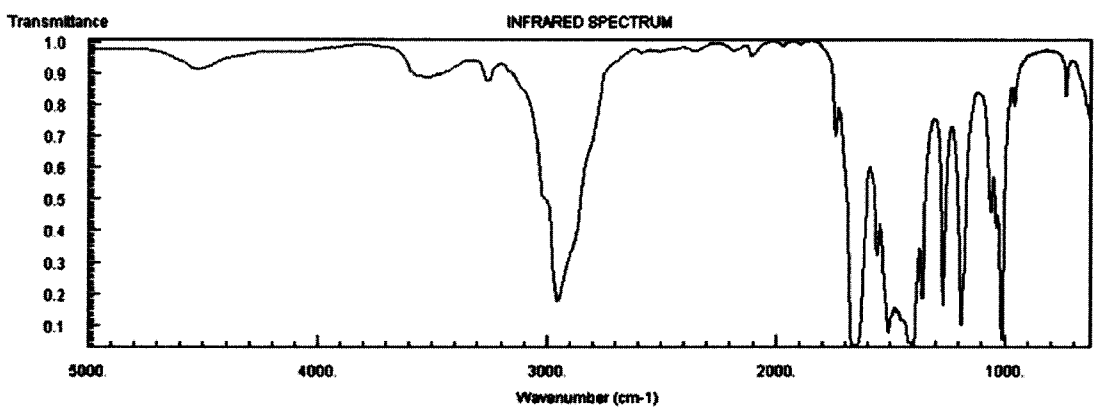

(b) n,n-dimethylacetamide

Fig. B.2 FTIR spectra of two organic compounds for the condensed pahse [Data from NIST Standard Reference Database 69:NIST Chemistry WebBook]

References

[1] M. Kobayashi, K. Tashiro, and H. Tadokoro, "Molecular Vibrations of Three Crystal Forms of Poly(vinylidene fluoride)," Macromolecules **8**, 158 (1975).

[2] R. Gregorio, Jr. and M. Cestari, "Effect of crystallization temperature on the crystalline phase content and morphology of poly(vinylidene fluoride)," J. Polym. Sci., Part B: Polym. Phys. **32**, 859 (1994).

[3] S. Lanceros-Méndiz, J. F. Mano, A. M. Costa, and V. H. Schmidt, "FTIR and DSC studies of mechanically deformed β-PVDF films," J. Macromol. Sci. –Physics **B40**, 517 (2001).

[4] M. Bai, M. Poulsen, A. V. Sorokin, and S. Ducharme, "Infrared spectroscopic ellipsometry study of vinylidene fluoride (70%)-trifluoroethylene (30%) copolymer Langmuir–Blodgett films," J. Appl. Phys. **94**(1), 195 (2003).

[5] Y. Ein-Eli, B. Markovsky, D. Aurbach, Y. Carmeli, H. Yamin, and S. Luski, "The dependence of the performance of Li-C intercalation anodes for Li-ion secondary batteries on the electrolyte solution composition," Electrochim. Acta **39**, 2559 (1994).

[6] D. Aurbach, B. Markovsky, A. Shechter, Y. Ein-Eli, and H. Cohen, "A Comparative Study of Synthetic Graphite and Li Electrodes in Electrolyte Solutions Based on Ethylene Carbonate-Dimethyl Carbonate Mixtures," J. Electrochem. Soc. **143**(12), 3809 (1996).

[7] D. Aurbach, Y. Gofer, M. Ben-Zion, and P. Aped, "The Behavior of Lithium Electrodes in Propylene and Ethylene Carbonate: The Major Factors That Influence Li Cycling Efficiency," J. Electroanal. Chem. **339**, 451 (1992).

[8] D. Aurbach, M.D. Levi, E. Levi, and A. Schechter, "Failure and Stabilization Mechanisms of Graphite Electrodes," J. Phys. Chem. B **101**, 2195 (1997)..

[9] K. Morigaki and A. Ohta, "Thermodynamic studies of cobalt and cadmium additions to nickel hydroxide as material for positive electrodes," J. Power Sources **76**, 159 (1998).

Appendix. C

Variational Equation of Motion for Circular diaphragm

In this chapter, detailed procedure that both equivalent stiffness and mass of the diaphragm, as referred in Chapter 4, are described with Mason model [1]. The potential energy of bending for a thin plate vibrating in flexure depends on two radii of curvature R_1 and R_2 rather than a single radius as does the bar bent in flexure. It is shown in "The Theory of Sound," (Rayleigh) [2] that the potential energy of bending is given by

$$\text{P.E.} = \frac{Y_o t_d^3}{24\,(1-\sigma^2)}\left(\frac{1}{R_1^2} + \frac{1}{R_2^2} + \frac{2\sigma}{R_1 R_2}\right), \tag{C.1}$$

where Y_0 is the Young's modulus, σ is the Poisson's ratio or the ratio of the lateral contraction to the longitudinal expansion of the material, and t_d is a thickness of the plate. This energy is calculated by calculating the energy of stretching part of the plate and compressing the other part about the center line of the plate which is assumed not to change length. This compares to the expression

$$\frac{Y_o t_d^3}{24}\left(\frac{1}{R_1^2}\right), \tag{C.2}$$

for a bar bent in flexure which has only one radius of curvature.

If, in addition, there is a tension which stretches the plate as a whole another term has to be added to the potential energy. In calculating this addition to the potential energy, the assumption is made that the tension T is so high that the change in tension due to displacing the membrane will be small compared to T. Under these assumptions, the increase in potential energy is found by multiplying the tension by the increase in area. If w is the displacement normal to the plane of the diaphragm, the altered area is given by

$$\iint \sqrt{1 + \left(\frac{\partial w}{\partial x}\right)^2 + \left(\frac{\partial w}{\partial y}\right)^2}\, dS, \tag{C.3}$$

where dS is an element of area. Hence the potential energy is

$$\text{P.E.} = T \iint \left(\sqrt{1 + \left(\frac{\partial w}{\partial x}\right)^2 + \left(\frac{\partial w}{\partial y}\right)^2} - 1 \right) dS$$

$$\simeq \frac{1}{2} T \iint \left(\left(\frac{\partial w}{\partial x}\right)^2 + \left(\frac{\partial w}{\partial y}\right)^2 \right) dS = \frac{1}{2} T \iint \nabla^2 w \, dS \ , \qquad \text{(C.4)}$$

where ∇w is the gradient of w.

If w is the displacement perpendicular to the plane of the plate at the point where rectangular coordinates are x and y, it has been shown from geometrical consideration that

$$\frac{1}{R_1^2} + \frac{1}{R_2^2} = \frac{\partial^2 w}{\partial x^2} + \frac{\partial^2 w}{\partial y^2} = \nabla^2 w \ ;$$

$$\frac{1}{R_1^2 R_2^2} = \frac{\partial^2 w}{\partial x^2} \frac{\partial^2 w}{\partial y^2} - \left(\frac{\partial^2 w}{\partial x \, \partial y}\right)^2 \ . \qquad \text{(C.5)}$$

Hence the complete expression for the potential energy of a thin stretched plate is

$$\text{P.E.} = \iint \left\{ \frac{(Y_0 + T)\, t_d^3}{24 (1 - \sigma^2)} \left[(\nabla^2 w)^2 - 2 (1 - \sigma) \left(\frac{\partial^2 w}{\partial x^2} \frac{\partial^2 w}{\partial y^2} - \left(\frac{\partial^2 w}{\partial x \partial y}\right)^2 \right) \right] + \frac{T}{2} (\nabla w)^2 \right\} dS \ . \qquad \text{(C.6)}$$

The added term T to the Young's modulus occurs because the added tension increases the effective modulus as shown by Rayleigh in connection with stretched bars.

For a complicated system of this type the equation of motion is usually found by employing the variation equation which states that the increase of the potential energy is due to the impressed forces acting though the displacement δw. If p is the transverse pressure on the diaphragm (which may be the resultant of pressure on the two sides of the diaphragm) and ρ is the density of the material, the vibration equation of motion is

$$\delta \text{P.E.} - \iint p \delta w \, dS + \iint \rho t_d \frac{\partial^2 w}{\partial t^2} \, p \delta w \, dS = 0 \ . \qquad \text{(C.7)}$$

This equation states that the increase in potential energy due to a displacement δw is equal to the pressure minus the mass times acceleration multiplied by the displacement δw and integrated over the surface of the plate.

By employing Green's theorem, Rayleigh has shown that the variation of the first term of P.E. can be expressed in terms of the variation in δw and ($d\delta w$ / dn) by

$$\delta \text{P.E.}_1 = \frac{(Y_0 + T)\, t_d^3}{12\,(1-\sigma^2)} \left[\iint \nabla^4 w \delta w \; dS \right.$$
$$- \int \delta w \, dl \left[\frac{\partial}{\partial n} \nabla^2 w - (1-\sigma) \frac{\partial}{\partial l} \left(\frac{\partial^2 w}{\partial n \, \partial t} \right) \right]$$
$$\left. + \int \frac{\partial \delta w}{\partial n} \, dl \left[\frac{\partial^2 w}{\partial n} + \sigma \left(\frac{1}{R} \frac{\partial w}{\partial n} + \frac{\partial^2 w}{\partial l^2} \right) \right] \right] \qquad \text{(C.8)}$$

where

$$\nabla^4 = \left(\frac{\partial^2}{\partial x^2} + \frac{\partial^2}{\partial y^2} \right) \left(\frac{\partial^2 w}{\partial x^2} + \frac{\partial^2 w}{\partial y^2} \right), \qquad \text{(C.9)}$$

dS is an element of area, dl is an element of length along the boundary, dn is an element of length normal to the edge, dt is an element of length along the tangent to the edge at the point under consideration and R is the radius of curvature of the edge of the diaphragm at the point under consideration. Simpler expressions for the last two terms are given later for square and circular boundaries.

In a similar manner the variation of the second term in (C.6) has been shown to be

$$\delta \text{P.E.}_2 = T \left[- \iint \nabla^2 w \delta w \, dS + \int \frac{\partial w}{\partial n} \delta w \, dl \right]. \qquad \text{(C.10)}$$

Hence the equation to be satisfied for every point of the surface is

$$\frac{(Y_0 + T)\, t_d^3}{12\,(1-\sigma^2)} \nabla^4 w - T \nabla^2 w - p + t_d \rho \frac{\partial^2 w}{\partial t^2} = 0 \; . \qquad \text{(C.11)}$$

From equation (C.11) the equation of motion satisfied by every point of a thin plate is

$$\frac{Y_0 t_d^3}{12(1-\sigma^2)} \nabla^4 w - p + t_d \rho \frac{\partial^2 w}{\partial t^2} = 0 \quad . \tag{C.12}$$

We assume here simple harmonic motion and a symmetrical motion about the circle. Hence equation (C.12) takes the form

$$\frac{Y_0 t_d^3}{12(1-\sigma^2)} \nabla^4 w - \omega^2 t_d \rho w - p = 0 \quad . \tag{C.13}$$

Setting

$$\frac{\omega^2 t_d \rho}{\frac{Y_0 t_d^3}{12(1-\sigma^2)}} = \frac{12\ \omega^2 \rho (1-\sigma^2)}{Y_0 t_d^2} = k^4 \tag{C.14}$$

the equation can be written

$$\left(\frac{d^2}{dr^2} + \frac{1}{r}\frac{d}{dr} + k^2\right)\left(\frac{d^2}{dr^2} + \frac{1}{r}\frac{d}{dr} - k^2\right) w = \frac{12 p (1-\sigma^2)}{Y_0 t_d^3} \quad . \tag{C.15}$$

The solution of this equation will be the sum of the solutions of the two separate factors in w. Since the Bessel's functions of second kind are inadmissible for this case on account of their infinite values at $r = 0$, a solution of this equation is

$$w = A J_0(kr) + B J_0(jkr) - \frac{p}{\omega^2 \rho\ t_d} \tag{C.16}$$

where

$$J_0(jkr) = I_0(kr) = 1 + \frac{1}{4}k^2 r^2 + \frac{1}{64}k^4 r^4 + \cdots \tag{C.17}$$

is the Bessel's function of zero order with imaginary argument.

To obtain the constants A and B, we assume first that the plate is rigidly clamped, i.e., $w = dw/dr = 0$ when $r = a$. Inserting these conditions, the constants A and B are determined by solving the equations

$$w = 0 = A\, J_0(ka) + B\, J_0(jka) - \frac{p}{\omega^2 \rho\ t_d}$$

$$\frac{dw}{dr} = 0 = k\left[-A\,J_1(ka) + B\,I_1(ka)\right] \tag{C.18}$$

where

$$I_1(kr) = -jJ_1(jka) = \frac{kr}{2} + \frac{k^3r^3}{16} + \frac{k^5r^5}{384} + \cdots . \tag{C.19}$$

Solving these equations, the value of the displacement w at any point becomes

$$w = \frac{p}{\omega^2\rho\, t_d}\left[\frac{I_1(ka)\,J_0(kr) + J_1(ka)\,I_0(kr)}{I_1(ka)\,J_0(ka) + J_1(ka)\,I_0(ka)} - 1\right] . \tag{C.20}$$

Integrating over the surface to find the volume velocity, one finds that the volume velocity is

$$V = j\omega 2\pi \int_0^a rw\,dr = \frac{j\pi pa^2}{\omega\rho t_d}\left[\frac{1}{\frac{ka}{4}\left[\frac{J_0(ka)}{J_1(ka)} + \frac{I_0(ka)}{I_1(ka)}\right]} - 1\right] . \tag{C.21}$$

Hence the impedance of the plate is

$$Z_p = \frac{p}{V} = +\frac{j\omega\rho t_d}{S}\left[\frac{\frac{ka}{4}\left[\frac{J_0(ka)}{J_1(ka)} + \frac{I_0(ka)}{I_1(ka)}\right]}{\frac{ka}{4}\left[\frac{J_0(ka)}{J_1(ka)} + \frac{I_0(ka)}{I_1(ka)}\right] - 1}\right] . \tag{C.22}$$

where S is the area of the plate.

The low-frequency values of the equivalent network can be obtained by expanding this expression in series form. Since

$$J_0(ka) = 1 - \frac{k^2a^2}{4} + \frac{k^4a^4}{64} - \frac{k^6a^6}{2304} + \frac{k^8a^8}{147456} + \cdots ,$$

$$I_0(ka) = 1 + \frac{k^2a^2}{4} + \frac{k^4a^4}{64} + \frac{k^6a^6}{2304} + \frac{k^8a^8}{147456} + \cdots ,$$

$$J_1(ka) = \frac{ka}{2} - \frac{k^3a^3}{16} + \frac{k^5a^5}{384} - \frac{k^7a^7}{18432} + \frac{k^9a^9}{1474560} + \cdots , \text{ and}$$

$$I_1(ka) = \frac{ka}{2} + \frac{k^3a^3}{16} + \frac{k^5a^5}{384} + \frac{k^7a^7}{18432} + \frac{k^9a^9}{1474560} + \cdots ,$$

it is easily shown that the impedance Z_d at low frequencies becomes

$$Z_d = -\frac{j16\, t_d^3\,(Y_0 + T)}{\omega a^4(\pi a^2)(1-\sigma^2)}\left[\,1 - \frac{9\,\omega^2\rho\,(1-\sigma)\,a^4}{80\, t_d^2\,(Y_0+T)} + \cdots\right], \qquad \text{(C.23)}$$

This will be the impedance of a compliance $\boldsymbol{C}$ in series with an acoustic inertance $\boldsymbol{M}$ having the values;

$$\boldsymbol{C} = \frac{a^4(\pi\, a^2)\,(1-\sigma^2)}{16\, t_d^3\,(Y_0+T)} \quad \text{and} \quad \boldsymbol{M} = \frac{9\,\rho\, t_d}{5\,(\pi\, a^2)}\ . \qquad \text{(C.24)}$$

In Fig. 4.1 (b), the series resonant circuit $\boldsymbol{C}_1$ and $\boldsymbol{M}_1$ represent the compliance, $1/k_{eq}$, and mass of the diaphragm, m_{eq}, which in mechanical impedance units will be

$$\boldsymbol{C}_1 = \frac{a^2(1-\sigma^2)}{16\,\pi\, t_d^3(Y_0+T)} \quad \text{and} \quad \boldsymbol{M}_1 = \frac{9\,\rho\, t_d(\pi\, a^2)}{5}\ .$$

$$k_{eq} = \frac{1}{\boldsymbol{C}_1} = \frac{16\,\pi\, t_d^3(Y_0+T)}{a^2(1-\sigma^2)} \quad \text{and} \quad m_{eq} = \boldsymbol{M}_1 = \frac{9\,\rho\, t_d(\pi\, a^2)}{5}\ , \qquad \text{(C.25)}$$

where πa^2 is the area of the diaphragm and air chamber. These are obtained from Eq. (C.24) by multiplying by $(\pi a^2)^2$.

References

[1] W. P. Mason, "Electromechanical Transducers and Wave Filters," Van Nostrand D. Company Inc., New York, 2nd ed. (1948).

[2] L. Rayleigh, "The theory of sound," Macmillan, London, 2nd ed. Vol. I (1894), Vol. II (1896).

Acknowledgements

First and foremost, I would like to express my deepest thanks to my supervisors, Professor Takashi Sugino and Professor Masanori Ozaki, for their guidance and encouragement throughout this dissertation work and my study.

I would like to thanks Professor Toshimichi Ito, Professor Tetsuya Yagi, Professor Yusuke Mori, Professor Mitsuhiro Katayama, Professor Toshiaki Suhara, Professor Masahiko Kondow, and Professor Yutaka Ohmori. Their helpful guidance and advices for my dissertation work are greatly appreciated.

I would like to express sincere gratitude to Emeritus Professor Seizo Morita, Emeritus Professor Kenji Taniguchi and Emeritus Professor Masanori Okuyama, Osaka University, for their supports and encouragements during the period of my study. I would like to thanks Associate Professor Hidemitsu Aoki. His helpful guidance, advices, and supports are greatly appreciated. I am very grateful to Professor Jonghyun Lee, Kyoungpook University, for his kind support throughout my study and life at Kyoungpook University. I would like to express sincere thanks to Mr. Hitoshi Kubo for his experimental assistance, scientific guidance and advices.

I would like to thanks Dr. Chiharu Kimura, Mr. Tetsuhiro Kodani of Daikin Co. Ltd., Mr. Daisuke Watanabe of Daikin Co. Ltd. about the support of research materials, Mr. Tunehisa Tanaka of Technology Research Institute of Osaka Prefecture, Dr. Takashi Futatsuki of Organo Corporation, Professor Katsuhiko Tanaka of Ritsumeikan University, Dr. Deuk-Soo Jang of UNIVE Co. Ltd.

Thanks are due to Dr. Hiroyuki Yoshida, Mr. Yo Inoue, Mr. Tetsuro Hori, Dr. Keiko Masumoto, Mr. Naoki Ooi, Mr. Eitaro Kubo, Mr. Daiki Terashima, Mr. Jung-min Park, Mr. Kyoung-gun Oh, Dr. Naoyuki Komatsu, Mr. Jae-ki Kim, Mr. Hoe-Kyoung Kim, Mr. Takuro Masuzumi, Mr. Masatomo Honjo, Mr. Yuji Yamauchi, Ms. Yuko Matsuhisa, and Ms. Saori Higashi for their support and friendship.

I appreciate sincerely to my mother for boundless love and being the anchor of my life.

Achievements

Publication

1. Jong-Hyeon Jeong, Chiharu Kimura, Hidemitsu Aoki, Masanori Okuyama, and Takashi Sugino, "Formation and Characterization of P(VDF-TeFE) Films Using Sol-Gel Methods for Application to Micro-Generators," Electrochemical Soc. Transactions vol.**19** (18), pp. 59-65 (2009).

2. Jong-Hyeon Jeong, Chiharu Kimura, Hidemitsu Aoki and Takashi Sugino, "Study about the effect of an electric field and a solvent during thermal treatment in film formation process of P(VDF-TeFE)," Japanese Journal of Applied Physics vol.**49**, 04DK23, 3pp (2010).

3. Jong-Hyeon Jeong, Daiki Terashima, Chiharu Kimura, and Hidemitsu Aoki, "Influences of Intensity of Electric Field on Properties of Poly(vinylidene fluoride-tetrafluoroethylene) Thin Films during Annealing Process," Japanese Journal of Applied Physics vol.**50**, 04DK09, 5pp (2011).

4. Jong-Hyeon Jeong, Chiharu Kimura, Hidemitsu Aoki, Masanori Okuyama and Takashi Sugino, "Properties of P(VDF-TeFE) thin film formed by annealing process with electric field," MRS Proceedings vol.**1218**, 1218-Z05-20 (2009).

5. Jong-Hyeon Jeong, Daiki Terashima, Chiharu Kimura and Hidemitsu Aoki, "The Study about the Control of Defect Factors to Improve Properties of P(VDF-TeFE) Thin Film," MRS Proceedings vol.**1312**, MRSF10-1312-HH03-14 (2011).

6. Hidemitsu Aoki, Daisuke Watanabe, Naoki Ooi, Jong-Hyeon Jeong, Chiharu Kimura, and Takashi Sugino, "High Rate Etching of Ru and TaN using Electrochemical Reaction for Bevel Cleaning," Electrochemical Soc. Transactions vol.**16** (19), pp. 9-14 (2009).

7. Hidemitsu Aoki, Daisuke Watanabe, Naoki Ooi, Jong-Hyeon Jeong, Chiharu Kimura, and Takashi Sugino, "Electrochemical Etching of Ru Film for Bevel Cleaning of Back End of Line," Japanese Journal of Applied Physics vol.**48**, 04C019, 3pp (2009).

8. Daisuke Watanabe, Hidemitsu Aoki, Jong-Hyeon Jeong, Chiharu Kimura, and Takashi Sugino, "Effect of Light Irradiation on Galvanic Corrosion of Metal Gate," Japanese Journal of Applied Physics vol.**48**, 04C003, 3pp (2009).

9. Naoki Ooi, Hidemitsu Aoki, Daisuke Watanabe, Jong-Hyeon Jeong, Chiharu Kimura, and Takashi Sugino,"Cu Electroplating Process with Magnetic Field for Flexible Device," Japanese Journal of Applied Physics vol.**48**, 046504, 3pp (2009).

10. Eitaro Kubo, Naoki Ooi, Hidemitsu Aoki, Daisuke Watanabe, Jong-Hyeon Jeong, Chiharu Kimura and Takashi Sugino, "Influence of Magnetic Field on Permeability of Electroplating Permalloy for Micro Energy Harvesting," Japanese Journal of Applied Physics vol.**49**, 04DB17, 3pp (2010).

11. Do-Wook Kim, Duk-Su Eun, Young-Ho Bae, In-Sik Yu, Chang-Gil Suk, Jong-Hyeon Jeong, Chan-Seop Cho and Jong-Hyun Lee, "Photoresist spray coating for three-dimensional micro structure," The Korean Sensors Society vol.**15** (3), pp. 153-157 (2006).

12. Sung-Jin Kong, Jong-Hyeon Jeong, Hee-Sung Kim, Dae-Young Kong, Duk-Soo Eun and Jong-Hyun Lee, "Study for Fabrication of micro-fluidic channel using micro-blaster," The Korean Physical Society vol.**24**, pp. 168 (2006).

13. Duk-Soo Eun, Jong-Hyeon Jeong, Jang-Kyoo Shin and Jong-Hyun Lee, "Fabrication of a Biofilter Using Anodic Reaction for Filtering Blood," Sensors and Materials vol.**20** (8), pp. 397-407 (2008).

International Conference Presentation

1. Jong-Hyeon Jeong, Chiharu Kimura, Hidemitsu Aoki, Masanori Okuyama and Takashi Sugino, "Formation and Characteristics of P(VDF-TeFE) Thin Films for Micro-generator," 215th ECS Conference, Hilton San Francisco Hotel, San Francisco, CA, USA (2009.5).

2. Jong-Hyeon Jeong, Chiharu Kimura, Hidemitsu Aoki and Takashi Sugino, "The study about the post-treatment of P(VDF-TeFE) thin film to improve internal structure using an electric field in forming process," Solid State Devices and Materials 2009, Miyagi, Japan (2009.10).

3. Jong-Hyeon Jeong, Chiharu Kimura, Hidemitsu Aoki and Takashi Sugino, "Application of P(VDF-TeFE) film to Energy Harvesting Devices," 2009 MRS Fall Meeting, Hynes Convention Center, Boston, MA, USA (2009.11).

4. Jong-Hyeon Jeong, Daiki Terashima, Chiharu Kimura, and Hidemitsu Aoki, "The influence of the intensity of an electric field on properties of P(VDF-TeFE) thin films during the annealing process," Solid State Devices and Materials 2010, Tokyo, JAPAN (2010.9).

5. Jong-Hyeon Jeong, Daiki Terashima, Chiharu Kimura, and Hidemitsu Aoki, "The study about the control of defect factors to improve properties of P(VDF-TeFE) thin film," 2010 MRS Fall Meeting, Hynes Convention Centrer, Boston, MA, USA (2010.11).

6. Duk-Soo Eun, Dae-Young Kong, Jong-Hyeon Jeong, Hee-Sung Kim and Jong-Hyun Lee, "Fabrication of a MEMS-based temper detection multi-sensor," 2006 Asia-Pacific Conference of Transducers and Micro-Nano Technology, Marina Mandarin Hotel, Singapore (2006.6).

7. Duk-Soo Eun, Dae-Young Kong, Jong-Hyeon Jeong, Hee-Sung Kim, Jang-Kyoo Shin and Jong-Hyun Lee, "A multi-sensor with integrated three functions," 2006 Microprocesses and Nanotechnology Conference, Kamakura, Japan (2006.10).

8. Jong-Hyeon Jeong, Jae-Bum Cho, Duk-Soo Eun and Jong-Hyun Lee, "Fabrication of vertical pore using an anodic reaction on (110) silicon," 2006 Microprocesses and Nanotechnology Conference, Kamakura, Japan (2006.10).

Domestic Conference Presentation

1. Jong-Hyeon Jeong, Chiharu Kimura, Hidemitsu Aoki and Takashi Sugino, "Formation of P(VDF-TeFE) piezoelectric polymer thin film with various solvents," 56th JSAP Spring Meeting, University of Tsukuba, Ibaraki, Japan (2009.3).

2. Jong-Hyeon Jeong, Chiharu Kimura, Hidemitsu Aoki and Takashi Sugino, "Influence of an electric field on properties of P(VDF-TeFE) piezoelectric polymer thin film," 70th JSAP Fall Meeting, Toyama University, Toyama, Japan (2009.9).

3. 青木秀充, 渡邊大祐, 大井直樹, 鄭 鍾炫, 木村千春, 杉野隆, "ベベルクリーニング用Ruバリア薄膜 の電気化学溶解", 電子情報通信学会 (SDM研究会), No.108, p.27 (2009.2).

4. 大井 直樹、青木 秀充、久保 英太郎、鄭 鍾炫、木村 千春、杉野 隆, "電磁場Cuめっきを用いた環境発電MEMS用マイクロコイルの作製プロセス", 電子情報通信学会 (電子デバイス研究会), ED2009-112 (2009.7).